Nano-silicon for light-controlled energy transfer to molecular oxygen

Amonkosolpan, Jamaree

Award date:
2014

Awarding institution:
University of Bath

NANO-SILICON FOR LIGHT-CONTROLLED ENERGY TRANSFER TO MOLECULAR OXYGEN

Jamaree Amonkosolpan

A thesis submitted for the degree of Doctor of Philosophy

University of Bath
Department of Physics

March 2014

Abstract

This thesis presents the results of several physical and magneto-optical experiments using nanostructured silicon fabricated by an electrochemical etching method. Quantum confinement causes the efficient visible light emission of nanocrystalline silicon. Long lived excitons confined in silicon nanocrystals are applied as an energy storage medium for energy transfer to oxygen. Nanocrystalline silicon-silica aerogel composites are synthesised and examined the sensitivity with adsorbed oxygen molecules.

Efficient energy transfer from photo-excited excitons to molecular oxygen to create singlet oxygen is presented in the experimental results. Spin exchange interactions are a key aspect controlling the energy transfer between silicon nanoparticles and molecular oxygens. Hence, modifications of the spins alter the dynamics of the energy transfer process. Spin distributions of the participating states are changed by applying magnetic fields or by changing excitation powers. Therefore, the dependences of the transfer process on magnetic field, excitation power and oxygen concentration were studied.

The energy transfer model is constructed based on a rate equation approach. The model produces simulations that are in good agreement with the overall data. The dynamic parameters are provided and indicate the characteristics of the silicon nanostructures. Possibilities for future work in this research area are included.

Acknowledgements

I would like to to express my gratitude to my supervisor, Dr Daniel Wolverson, for giving me his invaluable advice and patience, and providing support and encouragement throughout my PhD years. It has been a great experience to work under his supervision in the optical spectroscopy group.

I would like to thank Professor John Davies for his effort and ideas through the work in chapter 4. I also thank Professor Dmitri Kovalev for expert advice and guidance.

I am thankful to Dr Gazi Aliev, who accompanied and helped me to examine the results, including his effort to develop the model in chapter 4. I would also thank Dr Bernhard Goller for his help and suggestion on this work. I am grateful to Dr Stephen Bingham for interesting physics discussions and gossips.

I also thank Dr Matthew Rollings for creating aerogels in chapter 3. Special thanks also to Harry Bone for his help in the lab.

Further, I would like to thank the Royal Thai Government for their financial support.

Finally, I would like to express my deepest appreciation to my family members and my boyfriend for their love and unconditional support.

Contents

Chapter 1

Introduction

1.1 Introduction

Silicon (Si) is a well-known and non-toxic material with a diamond crystal structure. Si has been widely used for many electronic devices such as integrated circuits and microchips. However, Si is an inefficient light emitter in the infrared range even at cryogenic temperatures due to an indirect band gap about 1.11 eV at room temperature [1] that needs phonon assistance in the radiative process. Therefore, as a light emitter, it is highly inefficient, which also causes a very long lifetime of its excitonic state.

On 29 December 1959, Richard Feynman gave a discourse on "There's Plenty of Room at the Bottom" at the annual meeting of the American Physical Society at the California Institute of Technology (Caltech) [2]. Feynman proposed the idea of the possibility to manipulate atoms and molecules which inspired the invention of the field "nanoscience". Nanostructure materials can be created by two main methods, which are "top-down" and "bottom-up" [1]. The top-down technique refers to removing material from a bulk crystal to produce a nanostructured network such as etching [3], whereas the bottom-up produces the nanoscale material via self-assembly method, for example epitaxy [4].

Si nanostructure was first discovered by Uhlirs at Bell Laboratories in the 1950s by electrochemical etching of Si wafer [5]. In the 1990s, Si received consider-

able attention, in particular its nanostructure, owing to the discovery of efficient, bright red photoluminescence (PL) from porous silicon (PSi) [6, 7] at room temperature. For the following decade, the origin of the PL from Si nanostructure was discussed. Canham (1990) proposed that the visible PL was caused by quantum confinement [6]. Together with Lehmann (1991), he also interpreted the increasing of the effective bandgap as a result of quantum confinement [7]. Most studies conform with the argument of Canham and Lehmann et al [8, 9, 10, 11], nevertheless, alternative explanations were also suggested in order to describe the PL emission mechanism, for example surface hydrides and siloxene etc. [12].

With quantum confinement, Si exciton energies in nanoscale can be increased to 2.5 eV [13]. Reducing the sizes of Si down to nanoscale, increases the overlap of the exciton in momentum space and leads to a rising of the oscillator strength for radiative recombination of the exciton. Therefore, radiative lifetimes of smaller Si nanoparticles are shorter than larger Si nanoparticles [14]. However, even Si nanocrystals have the shorter lifetime than bulk Si, the exciton lifetime is still long (of the order of μs to ms) especially when compared with the lifetime of direct gap materials. This drives a huge potential of Si nanocrystals as photosensitisers of adsorbed molecules.

This introductory section provides a general introduction to the material based on Si and a brief overview about the discovery of Si nanostructures. The basic properties of molecular oxygen are also included. An idea to apply nanocrystalline Si as a photosensitiser is also introduced later in this chapter. We then go on to a following section which contains basic properties of bulk Si.

1.2 Bulk silicon

Bulk crystalline Si has a diamond structure with a lattice constant $a = 5.430$ Å and a tetrahedral bonding as shown in figure 1.1 [1]. Si is an indirect bandgap semiconductor with a valence band edge at the Γ point of the Brillouin zone. The conduction band edges lies along Δ which is close to a boundary X point as presented in figure 1.2. Thus, electronic transitions between the conduction band and the valence band need phonon assistance in order to conserve the crystal momentum.

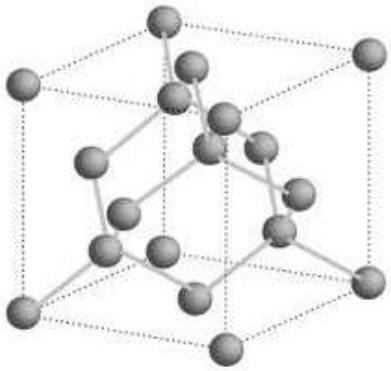

Figure 1.1: Schematic of the diamond crystal structure of Si after [1].

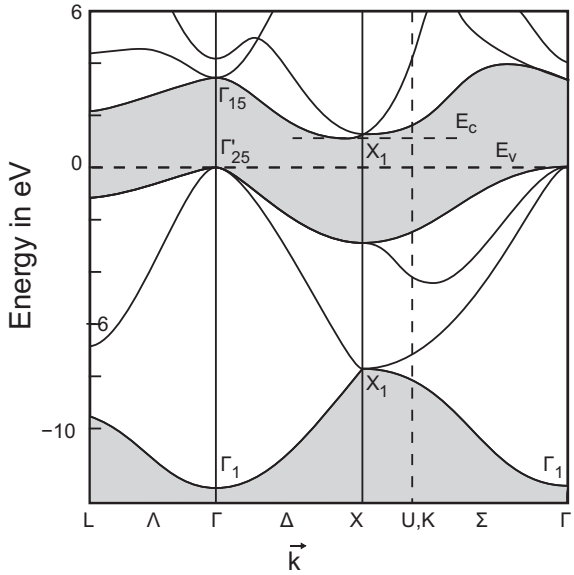

Figure 1.2: Schematic band structure of bulk Si after[15].

Figure 1.3 illustrates phonon assistance in optical transitions. The indirect transition can occur only with an absorption or emission of phonons to satisfy the momentum conservation. The energies of phonons involved in optical transitions for bulk Si are presented in figure 1.4. The relevant phonons include transverse optical phonons (TO), longitudinal optical phonons (LO) and transverse acoustic phonons (TA). At the Γ point of the Brillouin zone, the phonon energy is between 18 and 56 meV. A binding energy of the bulk Si exciton of 14.7 meV is not indicated in this figure [1].

Due to the involvement of phonons in the transition process, the radiative lifetime of bulk Si exciton is extremely long. Therefore, the free excitons can reach bound exciton states or non-radiative states then recombine without emission of light [13]. This is the reason of the inefficiency of light emission of bulk Si even at

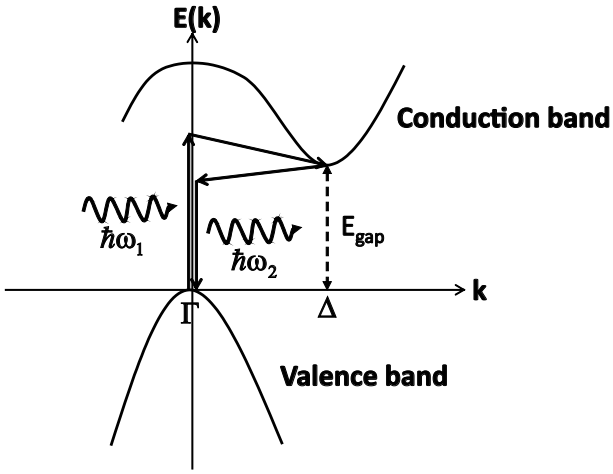

Figure 1.3: Schematic energy diagram of bulk Si. The electronic transition between the Γ and Δ points requires the contribution of momentum conserving phonons.

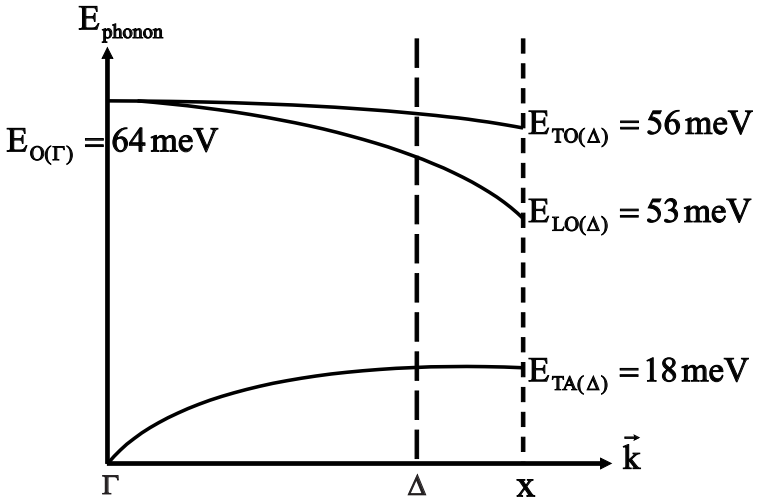

Figure 1.4: Dispersion relation of phonons in bulk Si.

cryogenic temperatures. However, in bulk Si, excitons can also be bound to doping atoms, hence these excitons fail to reach the non-radiative states. Instead of this process, the bound excitons can recombine and transfer energy to others as an Auger effect. The non-radiative Auger process also causes the ineffective PL emission in bulk Si [16, 17].

1.3 Silicon nanocrystals

As mentioned in section 1.1, as a consequence of the quantum size effect, the PL quantum yield of PSi is increased in comparison to the bulk Si. In the nanoscale structure, excitons are confined in the nanocrystal and cannot transport across to the other nanoparticles, therefore the recombination of the excitons usually happens within the same nanocrystal where they have been created. The rising of the PL quantum yield also is supported from a reduction of surface defects in PSi such as dangling Si surface bonds, owing to a passivation of PSi surface either by hydrogen or oxygen [18, 19, 20, 21].

At the nanostructure scale, the carrier density is extremely high, even if there are only few excitons per nanocrystal. Combining with the long radiative lifetime, hence, a saturation effect can arise if the excitation power is high enough. So excitons, in this situation, recombine non-radiatively via the Auger process [22]. This leads to the conclusion that most of the PL of PSi originates from radiative recombination process of excitons confined within the nanocrystals.

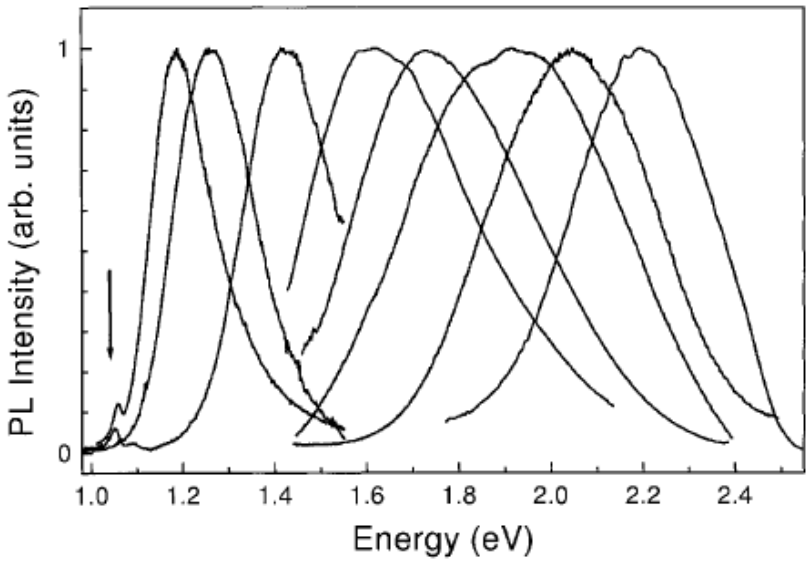

Figure 1.5: Tunability of PL spectra of PSi. The arrow shows the spectral position of the exciton transition in bulk Si after [13].

By size reduction, it is possible to increase the excitonic energies of PSi up to 2.4 eV as presented in figure 1.5. Several studies have revealed the dependence of the exciton energy on the nanocrystal size [14, 23]. Therefore, by varying the nanocrystal sizes, the emission band of Si nanocrystal assemblies is tuned to

achieve the desired energy range. Decreasing the size also causes the enhancement of the exciton binding energy. With the squeezing of the exciton by decreasing the nanoparticle size, the Coulomb interaction of electron-hole raises. Hence, the exciton binding energy increases to the order of ten to a hundred meV [14].

For bulk Si, the wave functions of holes and electrons are delta like functions in momentum space. Nevertheless, decreasing the size of crystal to the nanoscale (compared to the bulk exciton Bohr radius $\sim 4.5nm$) causes the effective quantum confinement. Consequently, the wave functions in k-space broaden and overlap with each other as displayed in figure 1.6. When the particle size reduces, accord-

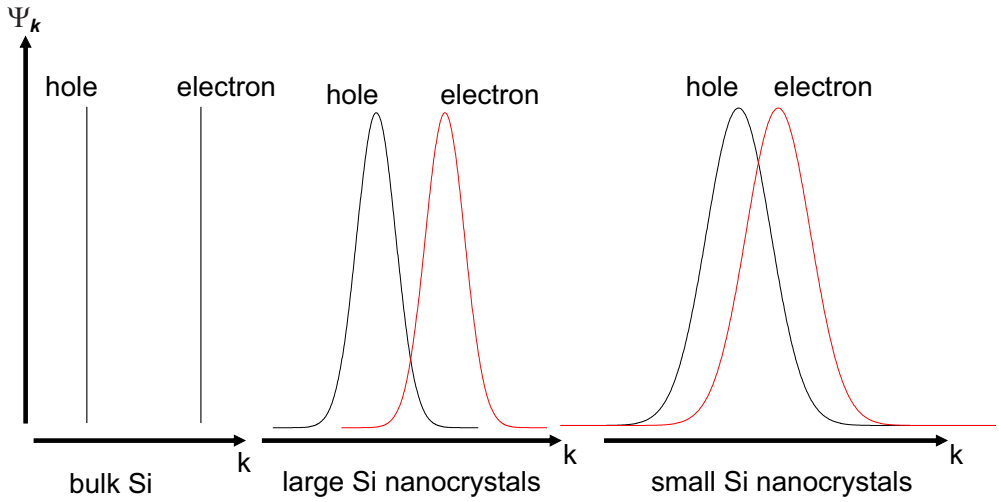

Figure 1.6: Schematic wavefunctions of electron and hole of bulk Si and Si nanocrystals in momentum space.

ing to the Heisenberg uncertainty principle, the momentum uncertainty of holes and electrons increases. Their wave functions become more overlapping in k-space. Thus, the valence and conduction band position shift closer to each other, whereas the crystal structure of the nanocrystals still maintains the diamond structure as in bulk Si [24].

Consider a one dimensional time-independent Schrödinger equation which can be written as [25]:

$$-\frac{\hbar^2}{2m}\frac{\partial^2}{\partial x^2}\Psi(x) + V(x)\Psi(x) = E\Psi(x),$$

where m is particle mass, $V(x)$ is a potential and E is an energy, respectively. For a particle in a box with an infinite potential wall and the length of the box

L, the energy eigenvalue is

$$E_n = \frac{\hbar^2 \pi^2}{2mL^2} n^2,$$

where n is a nonnegative integer number referring to the energy level. For the three-dimensional infinite potential box with all sides of length L, the energy eigenvalue is

$$E = \frac{\hbar^2 \pi^2}{2mL^2} \sum_{i=1}^{3} n_i^2, \tag{1.1}$$

where $i = 1, 2, 3$. As presented in equation 1.1, the energy band can be tuned by varying the size of the nanoparticle.

Turning now to Schrödinger's equation for an excitonic states within the confinement, it can be illustrated as [26]:

$$\left[-\frac{\hbar^2}{2m_e^*} \bigtriangledown_e^2 - \frac{\hbar^2}{2m_h^*} \bigtriangledown_h^2 + V_0(\vec{S_e}, \vec{S_h}) \right] \Psi(\vec{S_e}, \vec{S_h}) = E\Psi(\vec{S_e}, \vec{S_h}). \tag{1.2}$$

Here, m_e^* and m_h^* are electron and hole effective mass, respectively. V_0 is the potential energy of a confining sphere with a zero net charge. $\vec{S_e}$ and $\vec{S_h}$ are electron and hole positions, respectively. Finally, the excitonic band gap energy can be approximately by [26, 27]

$$E_{ex} = E_{bulk} + \frac{\hbar^2 \pi^2}{2R^2} \left(\frac{1}{m_e^*} + \frac{1}{m_h^*} \right) - \frac{1.8e^2}{\epsilon_2 R} + \frac{e^2}{R} \overline{\sum_{n=1}^{\infty} \alpha_n \left(\frac{D}{R} \right)^{2n}}, \tag{1.3}$$

with

$$\alpha_n = \left[\left(\frac{\epsilon_1}{\epsilon_2} - 1 \right) + (n+1) \right] / \left[\epsilon_2 \left(\frac{\epsilon_2}{\epsilon_1} n + n + 1 \right) \right].$$

Here, E_{bulk} is energy of bulk material, R is the radius of the nanoparticle, ϵ_2 is the dielectric constant of the nanoparticle, ϵ_1 is the dielectric constant of the surrounding medium, e is the elementary charge and D is the magnitude of the distance that the wave function peaks from the center of the spherical particle. The bar over the summation term signifies an average over the wave functions of $\vec{S_e}$ and $\vec{S_h}$. The second term and the third term are quantum energy of localization for electrons and holes and the Coulomb attraction between these two, respectively. The fourth term is the dielectric solvation energy loss. The calcula-

tion of equation 1.3 is based on the assumption that the nanocrystal is spherical [27]. In reality, the nanocrystals within PSi usually have an irregular shape, therefore equation 1.3 is used as a simplification.

1.3.1 Excitons confined in Si nanocrystals

Several studies have revealed that the spin exchange interaction between the two confined particles is a major contributing process of the basic optical properties of nanocrystal assemblies [14, 28, 29]. For Si nanocrystals, owing to the exchange interaction, the exciton state is split into two sublevels. There are an upper optically allowed singlet state ($S = 0$) and a lower, dipole forbidden triplet state ($S = 1$) [11, 30, 31]. Therefore, the triplet excitons lifetime is extremely long in order of 10^{-3} s. On the other hand, the lifetime of the singlet excitons is in the range of 10^{-6} s. However, compared with the direct bandgap recombination, it is still long.

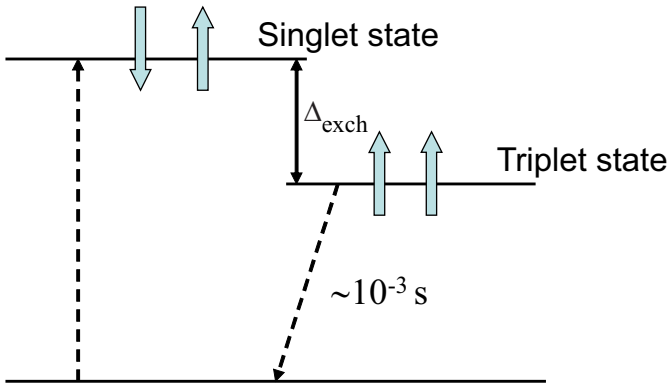

Figure 1.7: Sketch of the spin-singlet (S=0) exciton created by absorption of an exciting photon relaxes to the lowest possible triplet (S=1) state.

These two states are separated by the exchange interaction, so the exchange splitting energy (Δ_{exch}) depends on the nanoparticle size [32]. Generally, Δ_{exch} is in order of a few meV ($\sim 5 - 10\, m$eV) [11]. Figure 1.7 presents the singlet-triplet splitting of the excitonic state of Si nanocrystals. After the absorption of photons, excitons are created via the optically allowed transition to the singlet state. At low temperatures (T $\leq$ 10 K), k_BT [1] $\sim$ 0.8625 meV $<<$ Δ_{exch}, the excitons relax to the dipole forbidden triplet spin state via a spin-flip mechanism, leading to the very long decay time.

[1] k_B is the Boltzmann constant equal to $8.6173324(78)\times10^{-5}$ eV·K^{-1}

In contrast, at room temperature k_BT $\sim$ 25.875 meV $>>$ Δ_{exch}, both singlet and triplet are equally occupied (75% of all excitons are in the triplet, due to its multiplicity). Hence, the decay time is mostly controlled by the singlet exciton, with lifetime in the order of μs. This implies that the exciton lifetime of Si nanocrystals is long over the entire temperature range. Nevertheless, the radiative exciton lifetime of Si nanoparticle is still long in comparison with direct bandgap nanocrystals which normally is 10^{-8} to 10^{-9} s.

The long exciton lifetime is one of the reasons why Si nanocrystal can be a promising candidate to apply as the energy storage medium for excitation of adsorbed molecules such as molecular oxygen [33].

1.4 Molecular oxygen

Molecular oxygen (O_2)is a common substance in chemical and biological systems with a unique configuration of a triplet ground state ($^3O_2$). Exited states of O_2 play an important role in many chemical reactions including the photodynamic therapy of cancer, due to their high reactivity. [34]. Generally, at room temperature most oxygen is in the form of O_2, however, it is worth mentioning atomic oxygen. Each oxygen atom contains six outer electrons. The electronic configuration of atomic oxygen is $1s^2 2s^2 2p^4$. According to Hund's rule, the ground state of atomic oxygen has two unpaired electrons and is marked as a triplet ^{3}P state as shown in figure 1.8. This figure also presents the first two excited states of atomic oxygen which are designated as singlet ^{1}D and ^{1}S states.

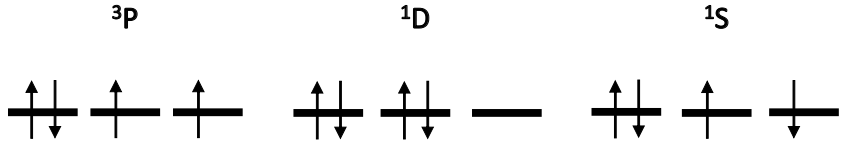

Figure 1.8: Electronic configurations of atomic oxygen.

These unpaired electrons in ^{3}P are bound with the other oxygen atom to form O_2 as shown in the schematic diagram in figure 1.9 The ground state electronic configuration of O_2 can be written as follows: $(\sigma_{1s})^2$ $(\sigma^*_{1s})^2$ $(\sigma_{2s})^2$ $(\sigma^*_{2s})^2$ $(\sigma_{2pz})^2$ $(\pi_{2py})^2$ $(\pi_{2px})^2$ $(\pi^*_{2px})^1$ $(\pi^*_{2py})^1$ [34, 35]. This electronic configuration of O_2 shows

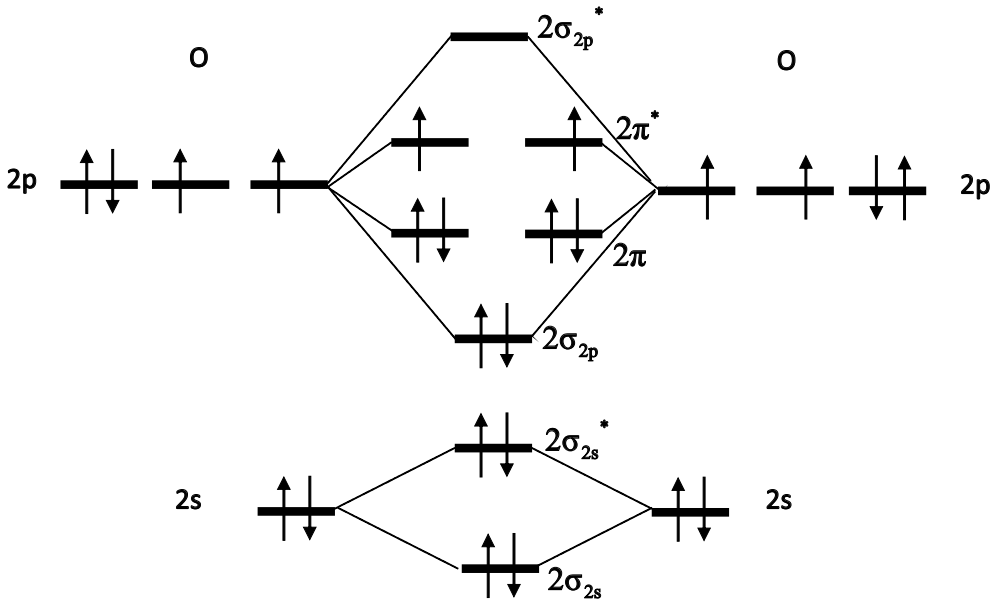

Figure 1.9: Schematic diagram of electronic configurations of molecular oxygen.

that the (π^*_{2p}) orbitals are each half filled, therefore, there are three possible states as followed: $^3\Sigma$, $^1\Delta$ and $^1\Sigma$. Hence, O_2 has the ground triplet state $^3\Sigma$.

The first two excited states of $^1O_2$ have singlet spin configuration which are the $^1\Delta$ and $^1\Sigma$ states as shown in figure 1.10. As a consequence of spin selection

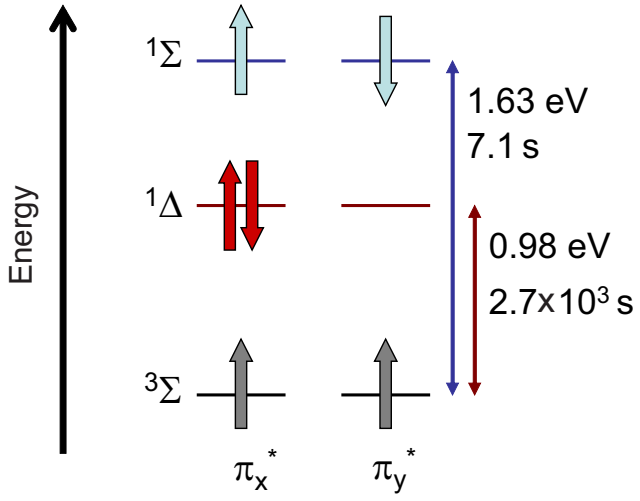

Figure 1.10: Electronic configurations of O_2. The triplet ground state, the first and the second excited states are indicated as $^3\Sigma$, $^1\Delta$ and $^1\Sigma$, respectively. The relative energy of these states and their lifetimes are included [36].

rules, direct optical excitation and de-excitation are forbidden. The transition

from the triplet ground state to the excited singlet state and vice versa requires a change of electron spin state (a spin-flip process) [36]. The radiative lifetimes of the $^1\Delta \rightarrow {}^3\Sigma$ and $^1\Sigma \rightarrow {}^3\Sigma$ are $\sim$ 2700 s and 7 s, respectively [34, 35].

The creation of singlet oxygen can be fulfilled by "photosensitisers". Traditionally, strongly light-absorbing organic dye molecules have been promoted as photosensitisers. After photo-excitation, the dye molecules interact with the O_2 via electron exchange to create $^1O_2$. Figure 1.11 shows that the photosensitisers

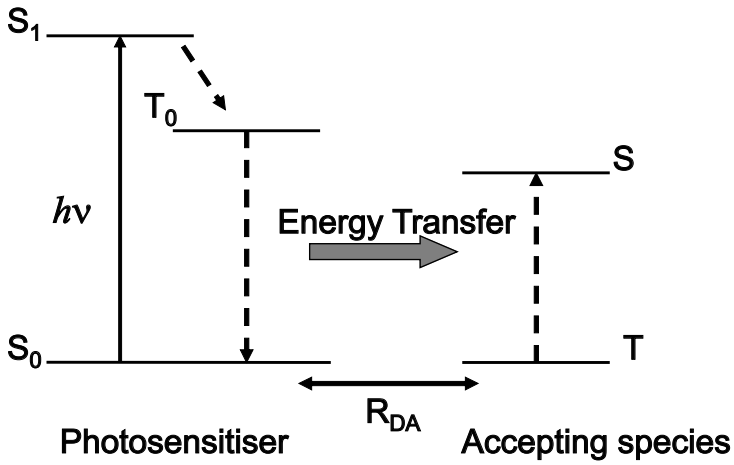

Figure 1.11: Schematic diagram of the energy transfer process. Here, S and T denote as singlet and triplet states, respectively. R_{DA} is the spatial distance between the photosensitiser and accepting specie.

are exited by photons to their optical active singlet states S_1. Afterwards, these sensitizers relax into their long-lived triplet states T_0. In case of energy matching, the excited sensitizers ("donors") can transfer energy to an accepting species ("acceptor") such as molecular oxygen.

Normally, energy transfer arises either by the dipole-dipole (Förster's model) or by the electron exchange interaction mechanism (Dexter's model). The Förster process is a non-radiative process based on a resonance theory of energy transfer [37, 38]. The relaxation of a photoexcited donor simultaneously generates the transition dipole which induces the formation of an excited acceptor. In this mechanism, the transitions are conducted by allowed electric-dipole. This requires the unchanged spins of the donor and the acceptor.

On the contrary, the Dexter model takes place via the direct electron-exchange

interaction between the photoexcited donor and the ground state acceptor. As if exchanging their states is a key factor of this energy transfer process, thereby, the process occurs within the short range of 10 Å [39]. This mechanism allows the transfer in which the two electrons undergo mutual spin-flips.

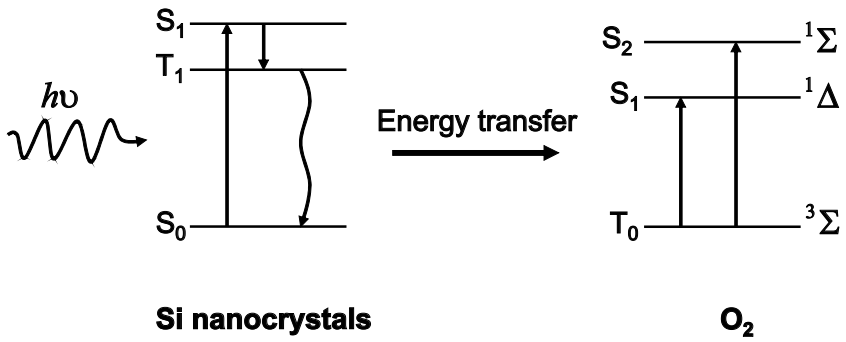

Figure 1.12: Schematic diagram of spin-flip activation process mediated by nanostructured Si.

In order to photo-sensitise oxygen molecules, the excited triplet state donor is required. Therefore, the Förster process, which involves only allowed transitions, is unable to apply to a triplet-triplet annihilation between the donor and the acceptor. However, in the Dexter process, the triplet-triplet annihilation is an allowed mechanism, owing to the spin restrictions being lifted, and is accompanied with the spin-flip of the O_2 [40] as presented in figure 1.12. Incident light ($h\nu$) creates excitons in the singlet state (S_1) then the excitons relax to the triplet state (T_1). The transfer of energy to O_2 occurs, consequently, the singlet oxygens are created. In case of the sensitisation, only the direct electron-exchange takes place in the energy transfer process.

1.5 Si nanocrystal as photosensitiser

As referred in the earlier section, we conclude that an ideal photo-sensitising material should satisfy the following characteristics: first of all, the selected material needs to be photoexcited easily; secondly, the lifetime of excited states of the chosen material is long enough; thirdly, the excited energies cover the energy range for the singlet oxygen generation; fourthly, there is a possibility to bring large numbers of elected materials and the oxygen molecules into close proximity;

finally, the photoexcited spin state of the selected material is a triplet state, in order to overcome the selection rules for excitation of the molecular oxygen.

Nanocrystalline Si satisfies all these requirements and could be a promising candidate as a photosensitiser for the following reasons. Even though, Si is indirect bandgap, the quantum confinement causes effective light emission. The spin exchange interaction of the confined excitons forms singlet-triplet states and results in a long exciton lifetime as mentioned in section 1.3.1. The tunability of PL emission band by adjusting the nanocrystals size also allows the matching of the singlet $^1O_2$ energy. A further advantage of using Si nanostructures is the enormous effective surface area for the adsorbed O_2. This advantage leads to the short separation distance R_{DA} in order to facilitate the spin exchange interaction. Finally, the triplet-triplet annihilation between the triplet exciton state of nanocrystalline Si and the triplet O_2 ground state via the spin-flip can be achieved by the allowance of the selection rules.

For the application in photodynamic therapy, Si nanoparticles have a great potential to function as the photosensitisers because of the following reason: The nanocrystals are non-cytotoxic with the absence of light. The study of PSi as photosensitisers for singlet oxygen by Xiao (2011) found that 54% of the hydrogen-terminated PSi degrade within 10 min at 37 °C in cell medium [41]. Therefore, degradation of Si nanocrystals in vivo is quick, consequently, the possibility of long term photosensitivity is minimised [41, 42, 43].

1.6 Outline of Thesis

The overall structure of this thesis takes the form of five chapters, including this introduction. This chapter contains basic knowledge of the bulk Si, the Si nanostructure and its behavior causing by the quantum confinement effect. The materials background is provided, along with the reasons behind the selection of Si nanocrystal as the facilitator for the photoexcitation of adsorbed oxygen molecule. Chapter 2 includes the synthesis of nanocrystalline Si along with the investigation of Si excitons by optical processes such as photoluminescence and Raman spectroscopy. Chapter 3 describes the design, synthesis, characterization and evaluation of the incorporation of Si nanoparticles into an aerogel including

the possibility to achieve the energy transfer with oxygen molecules. Chapter 4 presents the results of nanocrystalline Si by magneto-optical photoluminescence in the presence and the absence of molecular oxygen. In this chapter, the theoretical model of the energy transfer mechanism is discussed and compared with the experimental results. Chapter 5 concludes the current work with an overview of the findings as well as the future work in this research area.

References

[1] C. Kittel. *Introduction to solid state physics*. Hoboken, N.J. : Wiley, 2005.

[2] R. P. Feynman. There's plenty of room at the bottom. *Engineering and Science*, 23:5:22–36, 1960.

[3] M. Endo, Z. Jin, S. Kasai, and H. Hasegawa. Reactive ion beam etching of GaN and AlGaN/GaN for nanostructure fabrication using methane-based gas mixtures. *Japanese Journal of Applied Physics*, 41(4B):2689–2693, 2002.

[4] P. Atkinson, O. G. Schmidt, S. P. Bremner, and D. A. Ritchie. Formation and ordering of epitaxial quantum dots. *Comptes Rendus Physique*, 9(8):788–803, 2008.

[5] A. Uhlir. Electrolytic shaping of germanium and silicon. *Bell System Technical Journal*, 35(2):333–347, 1956.

[6] L. T. Canham. Silicon quantum wire array fabrication by electrochemical and chemical dissolution of wafers. *Applied Physics Letters*, 57(10):1046–1048, 1990.

[7] V. Lehmann and U. Gsele. Porous silicon formation: A quantum wire effect. *Applied Physics Letters*, 58(8):856–858, 1991.

[8] F. Buda, J. Kohanoff, and M. Parrinello. Optical-properties of porous silicon-a-1st-principles study. *Physical Review Letters*, 69(8):1272–1275, 1992.

[9] J. C. Vial, A. Briesy, F. Gaspard, R. Herino, M. Ligeon, F. Muller, R. Romestain, and R. M. Macfarlane. Mechanisms of visible-light emission from electroxidized porous silicon. *Physical Review B*, 45(24):14171–14176, 1992.

[10] A. J. Read, R. J. Needs, K. J. Nash, L. T. Canham, P. D. J. Calcott, and A. Qteish. First-principles calculations of the electronic properties of silicon quantum wires. *Physical Review Letters*, 69(8):1232–1235, 1992.

[11] P. D. J. Calcott, K. J. Nash, L. T. Canham, M. J. Kane, and D. Brumhead. Identification of radiative transitions in highly porous silicon. *Journal of Physics-Condensed Matter*, 5(7):L91–L98, 1993.

[12] O. Bisi, Stefano Ossicini, and L. Pavesi. Porous silicon: a quantum sponge structure for silicon based optoelectronics. *Surface Science Reports*, 38(13):1 – 126, 2000.

[13] D. Kovalev, H. Heckler, G. Polisski, and F. Koch. Optical properties of si nanocrystals. *Physica Status Solidi (b)*, 215(2):871–932, 1999.

[14] T. Takagahara and K. Takeda. Theory of the quantum confinement effect on excitons in quantum dots of indirect-gap materials. *Physical Review B*, 46:15578–15581, 1992.

[15] J. R. Chelikowsky and M. L. Cohen. Electronic structure of silicon. *Physical Review B*, 10:5095–5107, 1974.

[16] C. Delerue, M. Lannoo, G. Allan, E. Martin, I. Mihalcescu, J. C. Vial, R. Romestain, F. Muller, and A. Bsiesy. Auger and coulomb charging effects in semiconductor nanocrystallites. *Physical Review Letters*, 75:2228–2231, 1995.

[17] M. J. Kerr and A. Cuevas. General parameterization of auger recombination in crystalline silicon. *Journal of Applied Physics*, 91(4):2473–2480, 2002.

[18] S. Jung, K. H. andShih and D. L. Kwong. Developments in luminescent porous Si. *Journal of the Electrochemical Society*, 140(10):3046–3064, 1993.

[19] A. G. Cullis, L. T. Canham, and P. D. J. Calcott. The structural and luminescence properties of porous silicon. *Journal of Applied Physics*, 82(3):909–965, 1997.

[20] S. Tripathy, R. K. Soni, S. K. Ghoshal, and K. P. Jain. Optical properties of nano-silicon. *Bulletin of Materials Science*, 24(3):285–289, 2001.

[21] D. Jurbergs, E. Rogojina, L. Mangolini, and U. Kortshagen. Silicon nanocrystals with ensemble quantum yields exceeding 60%. *Applied Physics Letters*, 88(23):1–3, 2006.

[22] D. Kovalev, H. Heckler, B. Averboukh, M. Ben-Chorin, M. Schwartzkopff, and F. Koch. Hole burning spectroscopy of porous silicon. *Physical Review B*, 57(7):3741–3744, 1998.

[23] Z. C. Feng and R. Tsu. *Porous silicon.* World Scientific, 1994.

[24] L. T. Cullis, A. G. andCanham. Visible-light emission due to quantum size effects in highly porous crystalline silicon. *Nature*, 353(6342):335–338, 1991.

[25] S. Gasiorowicz. *Quantum physics.* John Wiley and Sons, Inc., New York, 1974.

[26] L. E. Brus. Electron-electron and electron-hole interactions in small semiconductor crystallites: The size dependence of the lowest excited electronic state. *The Journal of Chemical Physics*, 80(9):4403–4409, 1984.

[27] B. S. Kim, M. A. Islam, L. E. Brus, and I. P. Herman. Interdot interactions and band gap changes in cdse nanocrystal arrays at elevated pressure. *Journal of Applied Physics*, 89(12):8127–8140, 2001.

[28] M. Nirmal and L. Brus. Luminescence photophysics in semiconductor nanocrystals. *Accounts of Chemical Research*, 32(5):407–414, 1999.

[29] J. Heitmann, F. Muller, L. X. Yi, M. Zacharias, D. Kovalev, and F. Eichhorn. Excitons in Si nanocrystals: Confinement and migration effects. *Physical Review B*, 69(19), 2004.

[30] H. Heckler, D. Kovalev, G. Polisski, N. N. Zinov'ev, and F. Koch. Magneto-optical effects in photoluminescence of Si nanocrystals. *Physical Review B*, 60(11):7718–7721, 1999.

[31] E. Gross, .D Kovalev, N. Kunzner, J. Diener, F. Koch, V. Y. Timoshenko, and M. Fujii. Spectrally resolved electronic energy transfer from silicon nanocrystals to molecular oxygen mediated by direct electron exchange. *Physical Review B*, 68(11):115405–1–115405–11, 2003.

[32] T. Takagahara and K. Takeda. Excitonic exchange splitting and Stokes shift in Si nanocrystals and Si clusters. *Physical Review B*, 53(8):R4205–R4208, 1996.

[33] D. Kovalev, E. Gross, N. Künzner, F. Koch, V. Yu. Timoshenko, and M. Fujii. Resonant electronic energy transfer from excitons confined in silicon nanocrystals to oxygen molecules. *Phys. Rev. Lett.*, 89:137401, 2002.

[34] C Schweitzer and R Schmidt. Physical mechanisms of generation and deactivation of singlet oxygen. *Chemical Reviews*, 103(5):1685–1757, 2003.

[35] N. J. Turro, V. Ramamurthy, and J. C. Scaiano. *Modern molecular photochemistry of organic molecules*. Sausalito, Calif. : University Science, 2010.

[36] D. Kovalev and M. Fujii. Silicon nanocrystals: Photosensitizers for oxygen molecules. *Advanced Materials*, 17(21):2531–2544, 2005.

[37] T. Förster. Intramolecular energy migration and fluorescence. *Annalen Der Physik*, 2(1-2):55–75, 1948.

[38] P. D. Laible, R. S. Knox, and T. G. Owens. Detailed balance in Forster-Dexter excitation transfer and its application to photosynthesis. *Journal of Physical Chemistry B*, 102(9):1641–1648, 1998.

[39] D. L. Dexter. A theory of sensitized luminescence in solids. *The Journal of Chemical Physics*, 21(5):836–850, 1953.

[40] A. Damjanovic, T. Ritz, and K. Schulten. Energy transfer between carotenoids and bacteriochlorophylls in light-harvesting complex II of purple bacteria. *Physical Review E*, 59(3, B):3293–3311, 1999.

[41] L. Xiao, L. Gu, S. B. Howell, and M. J. Sailor. Porous Silicon Nanoparticle Photosensitizers for Singlet Oxygen and Their Phototoxicity against Cancer Cells. *Acs Nano*, 5(5):3651–3659, 2011.

[42] L. A. Osminkina, K. P. Tamarov, A. P. Sviridov, R. A. Galkin, M. B. Gongalsky, V. V. Solovyev, A. A. Kudryavtsev, and V. Y. Timoshenko. Photoluminescent biocompatible silicon nanoparticles for cancer theranostic applications. *Journal of Biophotonics*, 5(7):529–535, 2012.

[43] R. Tong and D. S. Kohane. Shedding light on nanomedicine. *Wiley Interdisciplinary Reviews-Nanomedicine and Nanobiotechnology*, 4(6):638–662, 2012.

Chapter 2

Porous Silicon Film

2.1 Introduction

Porous silicon (PSi) was first discovered by Uhlirs during an electrochemical etching of silicon (Si) wafer in hydrofluoric acid in 1956 [1]. In 1990, Canham [2] reported a visible (red) photoluminescence (PL) from PSi layers at room temperature. A PL blue shift was observed when the size of the silicon structures was reduced. Canham identified this phenomenon as an effect of a quantum confinement of silicon nanostructures. Lehmann and Gösele [3] also reported that the bandgap of porous silicon is larger than bulk crystalline silicon and attributed this increase to the quantum confinement. However, the mechanism of the luminescence from nano-silicon particles was widely discussed; many publications debated different theories about the origin of the visible PL [4, 5, 6] from PSi. Nevertheless, there is a large volume of published studies supporting the theory of the quantum confinement effect [7, 8]. Since then, silicon nanoparticles have become more attractive for potential applications.

2.2 Synthesis of silicon nanocrystals

There are several different ways to produce silicon nanocrystals, for example, aerosol procedure [9], thermal precipitation of silicon atoms implanted in SiO_2

[10], plasma enhanced chemical vapour deposition [11] or magnetron sputtering [12]. The conventional method of producing silicon nanocrystals is the electrochemical etching of bulk silicon in order to obtain porous silicon (PSi). The advantages of this method include good homogeneity and the possibilities to design thickness, porosity and pore sizes.

The morphology of PSi depend on the type and doping level of bulk Si as shown in table 2.1. The p-type Si wafer (commonly doped with boron) generates mesopores to micropores, the highly doped n^+ also gives mesopores. But the n-type bulk Si (normally with phosphorus-doped) tends to create macroporous silicon. Therefore, the pore diameter of p-type Si increases with the doping concentration. On the other hand, the n-Si pore diameter decreases with the doping concentration.

Table 2.1: Summary of the types of silicon morphologies. [13]

Silicon substrate type	**resistivity (Ω cm)**	**Pore type**	**Pore size (nm)**
p^-	1-20	Micropores	≤ 2
p^+	0.1-0.01	Mesopores	2-50
p^{++}	$\leq$0.01-0.001	Mesopores	2-50
n^+	0.1-0.01	Mesopores	2-50
n	$\geq$1	Macropores	>50

The properties of PSi depend on the fabrication conditions such as the substrate type, doping level, crystal lattice orientation, hydrofluoric acid (HF) concentration, current density and etching time. In this thesis, p-type B-doped silicon substrates (100) with resistivities of 1-10 Ω cm and 10-20 Ω cm have been used to fabricate PSi to obtain microporous Si. Before etching, the bulk Si substrate needs a thermal treatment in order to get rid of a hydrogen-diffused surface which commonly occurs during the Si wafer preparation. An oxide layer from this stage is removed by soaking this substrate in HF solution prior the etching process.

2.2.1 Fabrication of Porous Silicon

PSi is generated by electrochemical etching of crystalline silicon in hydrofluoric acid (HF) electrolyte. Anodisation of bulk Si in HF solutions creates pores and Si fragments. The size of these network pores can be reduced from the micrometer

down to the nanometer scale. [3, 14]. Figure 2.1 shows a schematic diagram of the anodisation method. A bulk silicon wafer is fixed by a teflon reservoir that is resistant to hydrofluoric acid (HF) and ethanol. An electro-chemically etched substrate of silicon is fixed on the copper back contact with an O-ring to seal the anodised cell. A Platinum mesh loop, which is used as a cathode, is immersed in HF electrolyte and placed parallel to the wafer to achieve a uniform and homogeneous PSi layer.

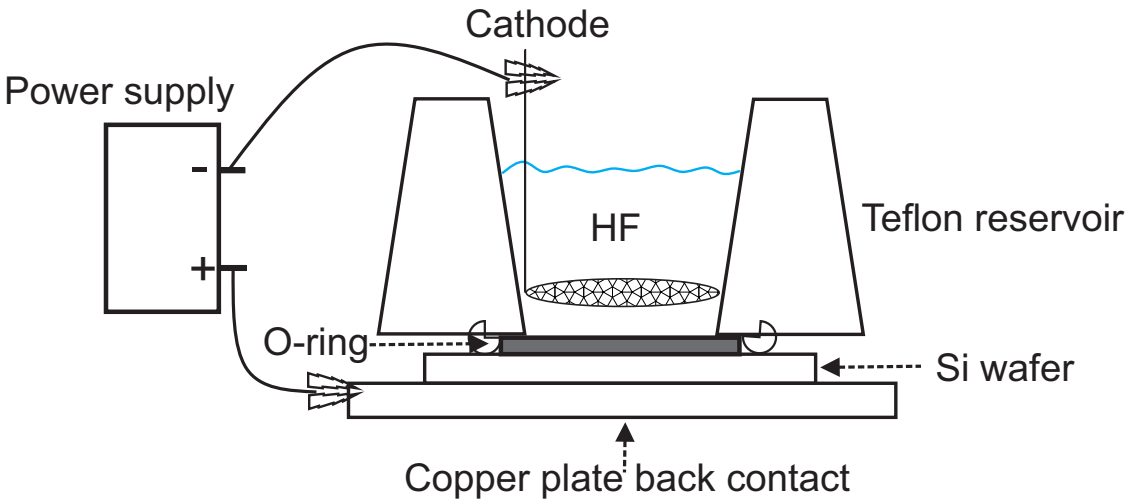

Figure 2.1: Schematic diagram of electrochemical cell : A reservoir contains HF electrolyte. A platinum wire is immersed in the HF solution, as cathode. A crystalline Si wafer sits on a copper plate which acts as the anode.

HF electrolyte solution can be produced by a mixture of aqueous HF (49 wt% HF in water) with ethanol in a ratio of 1:1 by volume and using a power supply working as a current source. The power supply is set to provide a constant current density of 37 mA/cm^2 then connected with a positive lead to the copper back contact; a negative lead to the platinum electrode. Etchting time is about 5-8 minutes to achieve a desirable PSi sample.

2.2.2 Pore Formation

The pore formation mechanism can be explained either by chemical or physical factors [13, 15]. Before applying an electric field, the hydrogen (H) saturated silicon surface is not attacked by fluoride ion (F^-) as presented in figure 2.2(a). By the applied electric field, valence band holes reach the surface of Si then a Si-H bond is susceptible to attack by the F^- to form a Si-F bond (figure 2.2(b)).

Due to polarisation effect from the Si-F bond, the second F^- attacks and replaces the remaining Si-H (figure 2.2(c)). In figure 2.2(c), the polarisation of Si-F bond is strong enough to reduce the electron density of Si-Si back bonds; then, these weakened bonds can be attacked by HF or H_2O. The silicon tetrafluoride reacts with the HF and forms the SiF_6^{-2} that leaves H-passivated surface as shown in figure2.2(d). For any remaining Si-F bonds, the H_2O can takeover the reaction and remove Si-F species from the surface [15]. The absence of Si-F species agrees well with FTIR measurements as presented in section 2.4. From FTIR results, the main identified vibration modes come from hydrides Si-H, Si-H_2 and Si-H_3 (details shown in section 2.4).

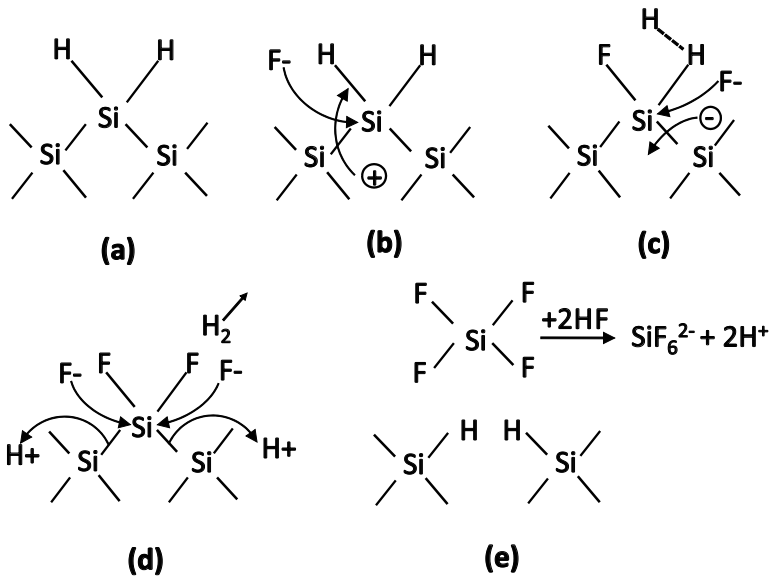

Figure 2.2: Mechanism for electrochemical etching of silicon in hydrofluoric acid (HF) associated with porous silicon formation (adapted from [3]) .

The physical factors that involved in pore formation are the electronic properties of the Si substrate such as the band structure, the type and dopant concentration etc [13]. Due to the excess valence band holes of p-type Si, there is no space-charge region that would produce a depletion between pores to stop the dissolution process. Therefore, the depletion region in p-type Si is originated from the quantum confinement of charge carriers [3]. The quantum confinement causes an increase of the effective energy band gap (details in chapter 1) which excludes valence band holes from these small region of the PSi.

2.3 Physical Characterisation of Porous Silicon

This section contains results of porosity, pore size and morphology that were determined by different methods. These include both destructive and non-destructive measurements, and the basic concepts and characteristic analysis of PSi samples.

2.3.1 Scanning Electron Microscopy

Scanning electron microscopy (SEM) is a technique that generates images of sample by focusing an electron beam in a small spot which is scanned across the surface of the sample. Images are commonly formed by collecting of secondary electrons or back scattered electrons which contains information about sample's surface topography and chemical combination. This tool can be used to quantify pore size, morphology and sample thickness.

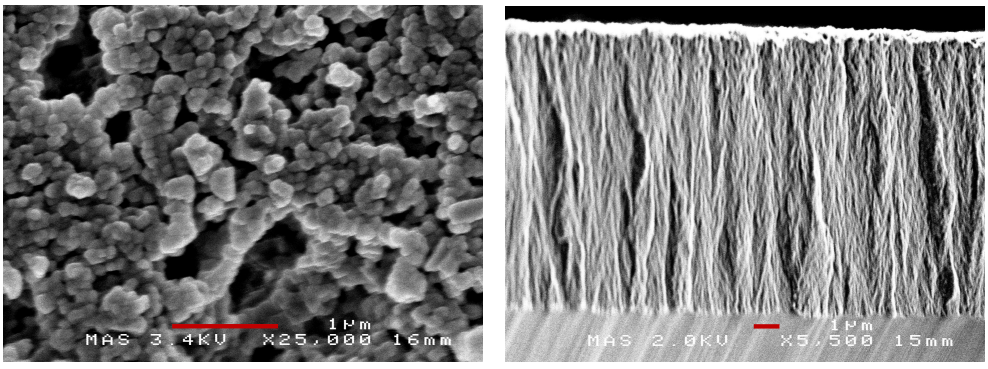

Figure 2.3: SEM images of PSi30 sample. (a) is a plan-view image with ×25,000 magnification. (b) is a cross-section view with ×5,500 magnification. The red scale bars are 1 μm.

Figure 2.3 shows SEM images of the PSi30 sample. This sample was prepared from (100) p-type silicon with 1-10 Ωcm resistivity, etched in a 1:1 (by volume) of 49% aqueous HF : ethanol solution. The porosity is 67.1%. Figure 2.3(a) shows the top-view of PSi with interconnected pores. Estimated pores sizes vary from 20 nm to 200 nm which would be a combination of mesopores and micropores as shown in table 2.1. Figure 2.3(b) displays the cross-section view showing the branshed and the "fir tree" structure. The thickness of this sample can be approximated around 11 μm.

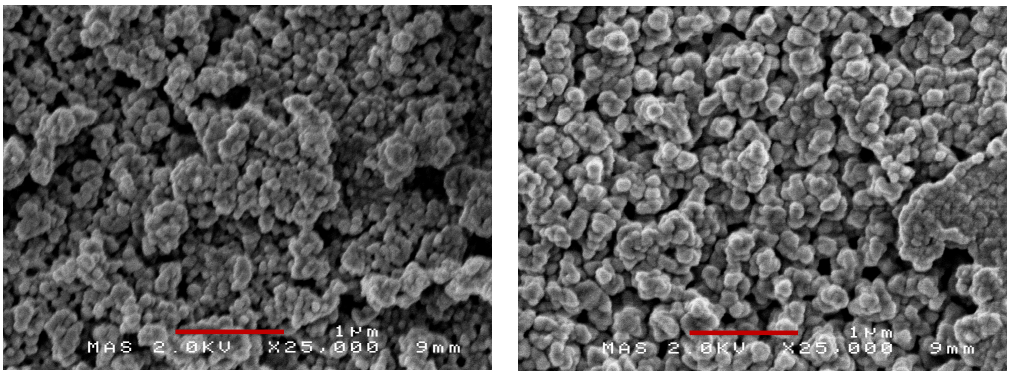

Figure 2.4: Comparison of SEM plan-view images PSi samples with different preparation conditions to produce the various sizes and porosities. Both images have ×25,000 magnification. The red scale bars are 1 μm. Both are prepared from (100) p-type silicon, etched in a 1:1 (by volume) of 49% aqueous HF : ethanol solution. Sample (a) (PSi34) and (b) (PSi703) are prepared from Si wafer with 1-10 Ωcm and 10-20 Ωcm resistivities, respectively. PSi 34 and 703 have porosities of 49.4% and 86.35, respectively.

SEM images from various samples are shown in figure 2.4. Obviously, the average pore size of PSi34 is smaller than PSi703 although the porosity of PSi34 is less than PSi703. As mentioned in section 2.2, the properties of a PSi sample can be designed by the preparation conditions. Other characterisation methods to determine porosity and thickness of the PSi samples will be shown in the next section.

2.3.2 Gravimetric measurement

Porosity (P) is defined as the ratio of the pore volume to the total volume of the PSi film:

$$P = \frac{V_{pores}}{V_{total}} \tag{2.1}$$

The gravimetric method is the simplest way to measure the porosity. It is, however, the least accurate method because this measurement is based on the assumption that the PSi layer is uniform. In reality, the preparation condition of PSi can cause non-uniform PSi layers. Therefore the gravimetric measurement that normally gives an average porosity value can be incorrect.

The gravimetric analysis is determined by weighing the sample before (m_1) and

after (m_2) etching, therefore the total pores volume is

$$V_{pores} = \frac{m_1 - m_2}{\rho_{Si} - \rho_{air}}, \tag{2.2}$$

where ρ_{Si} and ρ_{air} are the density of crystalline silicon (2.33 g/cm^3) and air(0.126 g/cm^3), respectively. Knowing the thickness (d) and area (A) of the PSi sample then by applying equation 2.2 into 2.1 then

$$P = \frac{m_1 - m_2}{(\rho_{Si} - \rho_{air})Ad} \tag{2.3}$$

For the thickness measurement, an optical microscope is used to measure the value which means the sample is needed to be cleaved.

Table 2.2: Gravimetric data and calculated porosity of some PSi samples

m_1(g)	m_2(g)	d (μm)	Diameter (mm)	Porosity (%)
3.17876	3.16114	8.4	39.15	79.01
3.1376	3.1183	13.8	38.74	52.83
2.95576	2.9402	7.8	39.12	75.28
2.94975	2.93411	8.4	38.96	70.83

Table 2.2 shows gravimetric data and porosity from p-type PSi samples. By weighing the Si substrate before and after etching, we should obtain the m_1 and m_2, respectively.

2.3.3 Reflection measurement

As mentioned in 2.3.2, the gravimetric method is the least accurate way to determine the PSi thickness, therefore this section explains another technique of optical reflectance. A schematic set up diagram of the reflectance measurement is displayed in figure 2.5.

A 100-Watt halogen lamp creates the white light that is passed through a lens and a pinhole to make a parallel beam. The beam passes through a beam splitter, then is incident on the sample surface. An interference pattern is created from

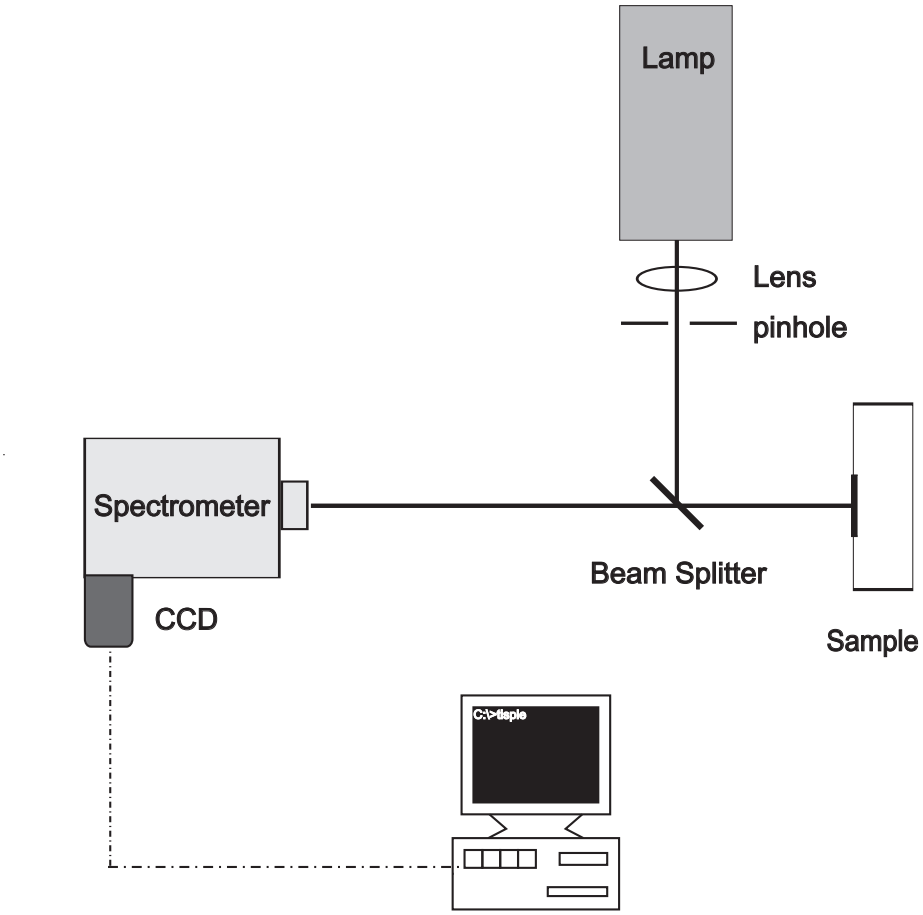

Figure 2.5: Schematic diagram of reflectance measurement.

reflection of the interface between medium/PSi and PSi/bulk Si, which is recorded by a CCD. The measurement displays Fabry-Pérot interference spectra which rely on the presence of a single porous layer on top the polished-back silicon substrate for determination the porosity of PSi sample.

For a Fabry-Pérot film, reflectance (R) can be expressed as [16, 17]:

$$R = \frac{r_1^2 + r_2^2 + 2r_1 r_2 cos2\delta_1}{1 + 2r_1 r_2 cos2\delta_1 + r_1^2 r_2^2},$$

$$\delta_1 = \frac{2\pi n_1 d_1}{\lambda}, \tag{2.4}$$

where r_1 and r_2 are the reflection coefficients of optical waves at the interface air/PSi and PSi/Si substrate, respectively, δ_1 is the change in phase of the interfering beam in the PSi layer, n_1 is refractive index of PSi, d_1 is the thickness of the PSi, and λ is the wavelength of the light. The optical path length $n_1 d_1$ can be calculated by considering in case of adjacent extrema (minima or maxima)

when $cos2\delta_1 = \pm 1$ then equation 2.4 will be

$$n_1 d_1 = \frac{\lambda_i \lambda_{i+1}}{4(\lambda_i - \lambda_{i+1})}, \tag{2.5}$$

where λ_i and λ_{i+1} are the positions of two closest extrema. Therefore knowing d_1, we can calculate the PSi reflective index by equation2.5.

The porosity of the PSi can be derived by using the Bruggeman effective medium approximations (EMA) [18, 19, 20]. The EMA theory assumes that the medium is spherical inclusions or circular inclusions in a two-dimensional composite [21, 22]. For two or more materials a,b,..., the Bruggeman's model can be expressed as

$$f_a \frac{\varepsilon_a - \varepsilon_{eff}}{\varepsilon_a + 2\varepsilon_{eff}} + f_b \frac{\varepsilon_b - \varepsilon_{eff}}{\varepsilon_b + 2\varepsilon_{eff}} + \ldots = 0, \tag{2.6}$$

where f_a+f_b+...=1. f_a and f_b are respectively the volume fractions of material a and b and ε_a, ε_b are the dielectric constants of a and b and ε_{eff} is effective dielectric constant.

Applying to the PSi case, f_a is a volume fraction of air inside porous medium, which equals to P, ε_a=ε_{air}=n^2_{air} and the b material is bulk Si, therefore f_b=f_{Si}=1−P and ε_b=ε_{Si}=n^2_{Si}. Equation 2.6 can be presented in

$$P \frac{n^2_{air} - n^2_{eff}}{n^2_{air} + 2n^2_{eff}} + (1 - P) \frac{n^2_{Si} - n^2_{eff}}{n^2_{Si} + 2n^2_{eff}} = 0, \tag{2.7}$$

where $n_{air} \approx 1$, $n_{Si} \approx 3.47$ [18, 23] and n_{eff} is the refractive index of PSi which can be obtained from n_1 in equation 2.5. Therefore applying the EMA from equation 2.7, the porosity can be measured out.

An example of optical reflectivity spectra in figure 2.6 demonstrates the Fabry-Pérot interference patterns. A black solid line and a blue dashed line are, respectively, a normalised reflectance spectra and a calculated reflectance spectra. The thickness of this sample is 7.8 μm measured by the optical microscope. By the fitting in figure 2.6, the results from this analysis are $n_{eff} = 1.574$ μm and $P = 69.7\%$ at $\lambda = 1.2$ μm. The results in table 2.3 present the calculated porosity and refractive index of PSi samples. This also includes a comparison of the porosity by reflectivity measurement with the gravimetry.

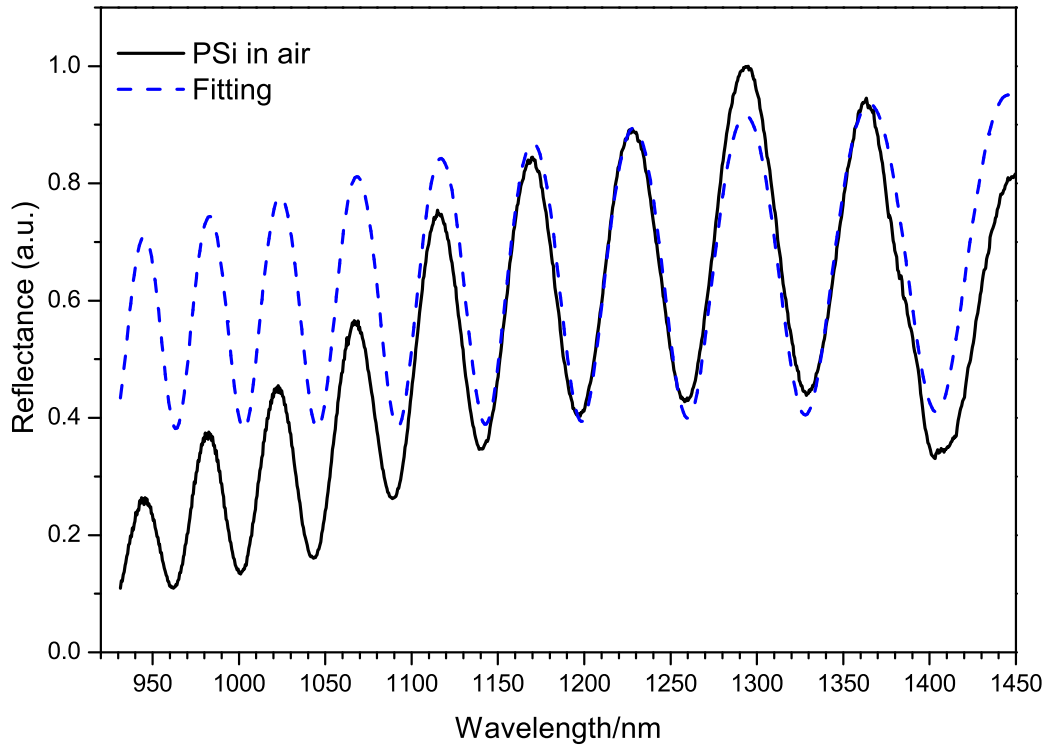

Figure 2.6: Normalised reflection spectra of a PSi : solid line is an experimental result and dash line is a fitting

This section describes and discusses the methods used to provide the physical characteristics of PSi samples. SEM images declare the traditional fir tree structure of PSi and can be used to estimate the pore sizes. The porosities were measured by both gravimetric and optical reflectance for comparison.

2.4 Fourier transform infrared transmission

Infrared (IR) spectroscopy is a common technique used to determine the qualitative and quantitative features of compounds [24]. Each molecule has an oscillation with a set of vibrational frequencies. If the IR frequency is associated with that oscillating vibration then the molecule absorbs the IR radiation. This absorption is resonant frequency. Therefore, the resulting spectrum can be used to identify and characterise the sample. Since, each molecule and atomic bond contains its

Table 2.3: Calculated porosity and reflective index of some PSi samples at λ =1.2 μm

EMA method		**Gravimetric method**
porosity (%)	**refractive index (n)**	**porosity (%)**
81.1	1.302	79.01
82.2	1.278	52.83
69.7	1.574	75.28
69.3	1.585	70.83

Note: PSi samples in this table is the same series of the sample in table 2.2.

own unique vibration frequency, IR spectra provides information about molecular structure and bonds.

Originally, the conventional IR experiment was a dispersive technique, by applying a diffraction grating to disperse the frequencies of IR source, which means data points at each frequency are measured one at a time. This results in both time consuming measurement and poor signal to noise ratio in spectrum. In the early 1970's, these limitations were overcome by using Fourier transform infrared spectroscopy (FT-IR)[25]. FT-IR is typically based on principle of Michelson's interferometer and Fourier transform technique to convert a time-domain into its corresponding frequencies. Light from IR source is directed to a beam splitter that divides reflected and transmitted light to a fixed and a moving mirror, respectively as displayed in figure 2.7. Both beams reflect off their respective mirrors. With the mirror movement, an optical path different is occurred $\delta = 2\Delta$ where Δ is a mirror displacement. For constructive interference, a maximum intensity signal is observed then $\delta = n\lambda$ where $n = 0, 1, 2, \ldots$. On the other hand, a minimum intensity can be detected when $\delta = (n + \frac{1}{2})\lambda$ where $n = 0, 1, 2, \ldots$ for destructive case. Therefore, the mirror moves back and forth, and creates a sinusoidal wave in the intensity of the signal which is referred as an interferogram. As each frequency produces its interferogram, the detector determines the sum of all the interferograms that can be converted by using the Fourier transform to a corresponding spectrum $F(\omega)$. All frequencies are measured simultaneously in a single data collection leading to very fast measurement. So the spectrum can be collected in a shorter time and a better signal to noise ratio compares with

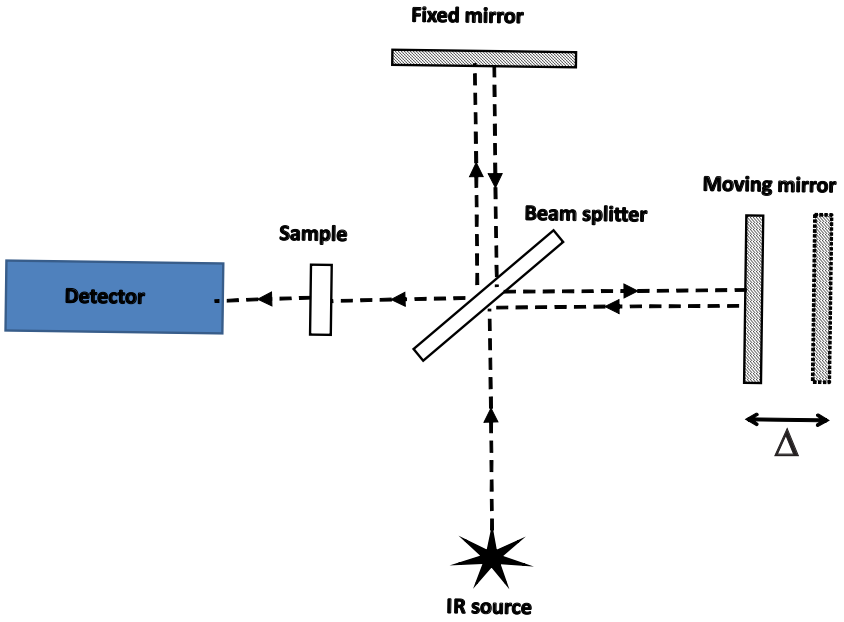

Figure 2.7: Schematic diagram of Michelson interferometer

the original IR technique.

$$F(\omega) = \int_{-\infty}^{\infty} f(x) e^{i\omega x} dx,$$

and the inverse Fourier transform is

$$f(x) = \frac{1}{2\pi} \int_{-\infty}^{\infty} F(\omega) e^{-i\omega x} d\omega,$$

where ω is angular frequency, x is optical path length, $F(\omega)$ is a spectrum and $f(x)$ is the interferogram points.

The FT-IR spectroscopy can be applied to samples in either solid, liquid or gas phase. Traditionally, FT-IR is a technique based upon the transmission of IR passing directly through the sample, meaning that the IR beam also needs to penetrate through the bulk Si substrate. Commonly, free carriers in Si strongly absorb IR radiation therefore with the transmission configuration, the samples, especially, with highly doped Si substrate, have too strong absorbing signals. The other problem is that Fabry-Pérot interference can appear in the transmission mode [13]. This interference in IR spectra obscures the IR peaks of interest and consequently, attenuated total reflectance (ATR) is used to encounter these problems.

The ATR technique applies the total internal reflection principle. We are considering the beam of radiation when it passes through an interface between two materials with different refractive indices as shown in figure 2.8. According to Snell's law (figure 2.8(a))

$$n_1 \sin\theta_i = n_2 \sin\theta_t,$$

where n_1 and n_2 are reflective indices of ATR cell and sample, respectively and θ_i and θ_t are angle of incidence and transmission, respectively. Increasing θ_i to the critical angle (θ_c) as presented in figure 2.8(b), then

$$\theta_c = \sin^{-1}\frac{n_2}{n_1}.$$

Thus for all values of $\theta_i \geq \theta_c$, total internal reflection can occur (figure 2.8(c)) at the interface of ATR crystal and sample (angle of reflection (θ_r) $= \theta_i$) [17].

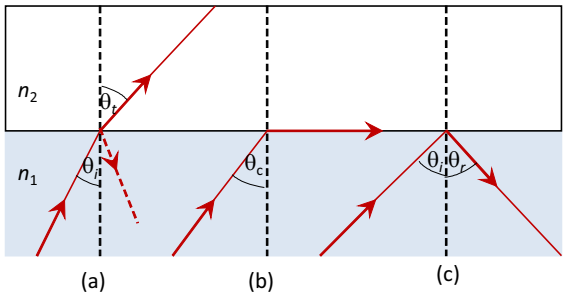

Figure 2.8: Diagram of an internal reflection principle

This creates an evanescent wave that extends into the sample if the sample is in contact with the ATR crystal. Also, this method can be succeeded only if the refractive index of the crystal is greater than the sample, otherwise the internal reflectance cannot take place ($n_{21} = n_2/n_1$ then $n_{21} < 1$). Figure 2.9 displays a multiple reflection ATR system. The beam strikes and undergoes into the crystal and reflects several times within the ATR crystal then exits towards the detector. However, our ATR is a single reflection system, hence, only has one bounce. The intensity of the evanescent wave extends inside the sample [26]:

$$I_{ev} = I_0 \exp(\frac{-z}{d_p}),$$

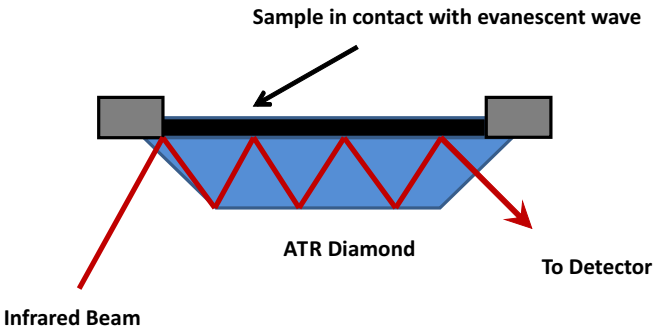

Figure 2.9: Schematic diagram of a typical ATR

where z is the distance normal to the optical interface, I_0 is the intensity at $z = 0$ and d_p is the penetration depth which is defined by,

$$d_p = \frac{\lambda}{2\pi n_1 (sin^2\theta - n_{21}^2)^{1/2}}.$$

The penetration depth depends on the wavelength (λ), the refractive indices of the ATR crystal (n_1) and the sample (n_2) and the angle of the entering light beam (θ). n_{21} is $\frac{n_2}{n_1}$.

In this case the surface of PSi can have different surface composition. The FT-IR transmission measurements were determined by using a Perkin Elmer Frontier FTIR. A diamond is used as the ATR crystal, which covers over wide IR spectral range. The sample must be in direct contact with the diamond ATR head.

Table 2.4 shows the typical infrared band frequencies of PSi. The comparison of the IR absorption spectra between an oxidised and refreshed feature of PSi film is displayed in figure 2.10. A black line represents a refreshed sample that clearly provides Si-H$_x$ (x=1,2 and 3) vibrational mode with corresponding wavenumber of 2,000-2,250 cm^{-1}, whereas the oxidised PSi (a red line) observes an imprecise Si-H band in this region. For the other Si-H band at 850-950 cm^{-1}, the refreshed PSi obviously shows these features in contrast with the oxidised PSi. However, the oxidised PSi spectrum displays Si-O vibrations at $\approx 1,100$, $\approx 1,010$ and ≈ 800 cm^{-1} while Si-O absorption bands of the refreshed spectrum have virtually disappeared at ≈ 800 cm^{-1} although the strong 1,050 cm^{-1} band still appears. This can imply that the surfaces of the refreshed PSi are H-terminated upon the removal of oxide layer by HF refreshing.

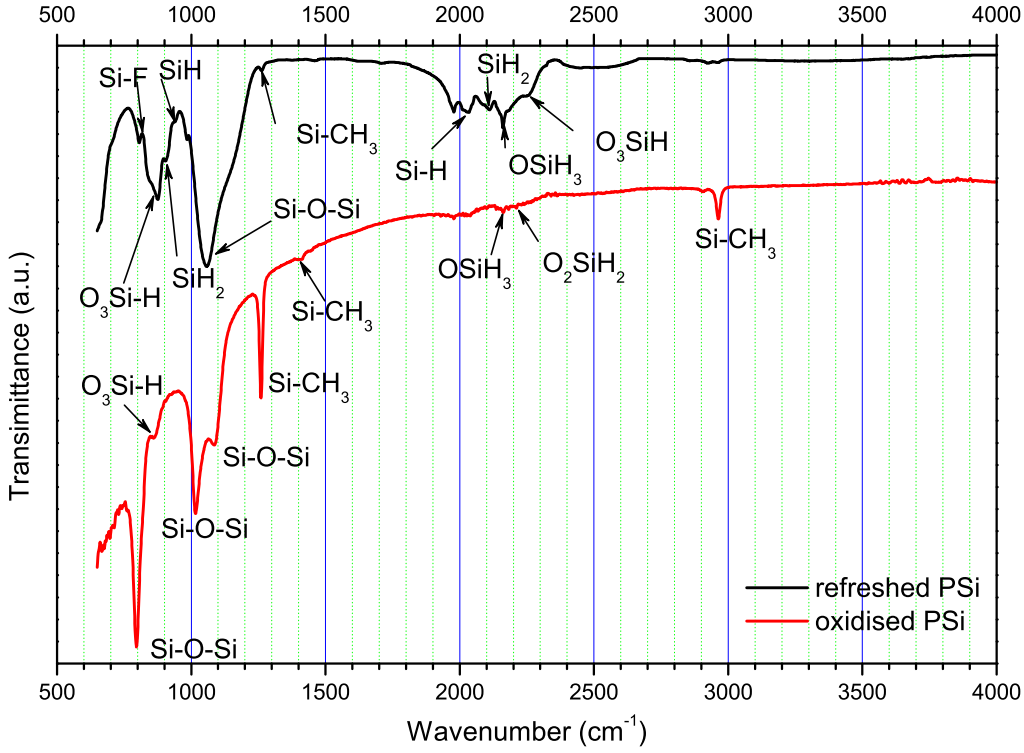

Figure 2.10: Normalised ATR-FTIR spectra of refreshed and oxidised PSi at room temperature: A PSi film was prepared from the p-type B-doped silicon substrate (100) with resistivity of 1-10 Ωcm using a current density of 36.71 mA/cm^2; the film has 49.4% porosity and 2.18 reflective index. The sample was oxidised about 5 weeks under ambient condition before measurement then refreshed in HF vapour and remeasured.

Figure 2.11 illustrates both PSi samples exhibit the Si-H vibrational bands at about 2,000-2,250 cm^{-1} and 850-950 cm^{-1}. Also the IR absorption bands attributable to Si-CH species (2,850-3,000 cm^{-1}) and Si-F (810 cm^{-1}) are detected. The spectra obviously show that the IR absorption of sample PSi34 is significantly stronger than the other sample, corresponding with their porosities (the porosity of samples PSi30 and PSi34 are 67.1% and 49.4%, respectively).

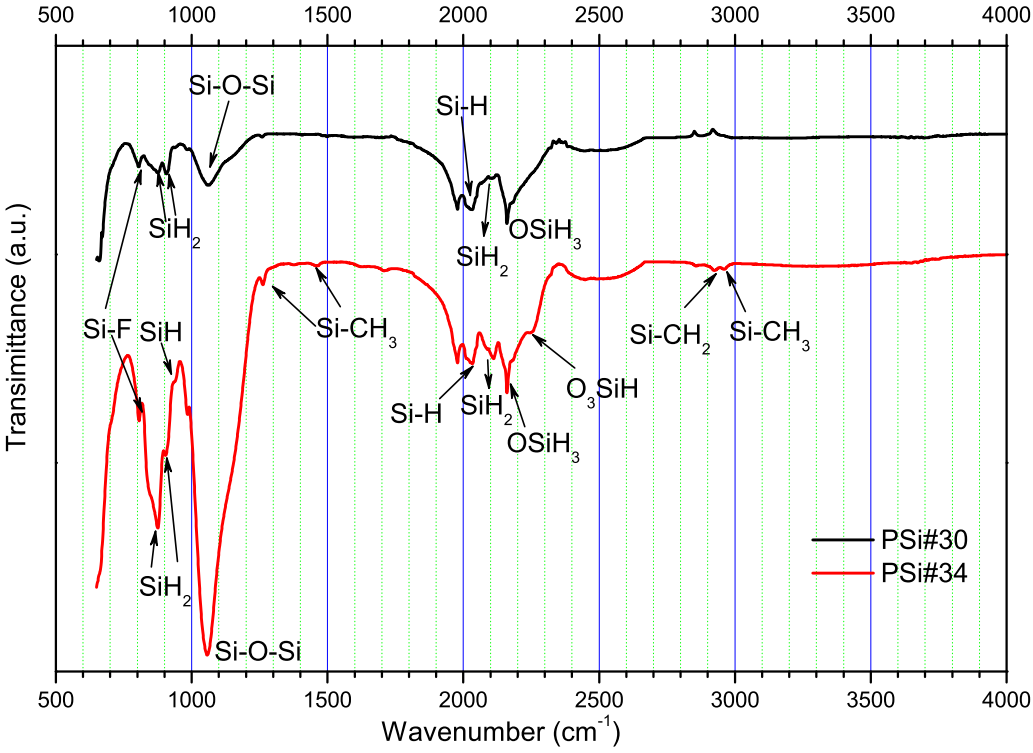

Figure 2.11: Normalised FTIR spectra of PSi samples with different porosity at room temperature. Both samples were produced from the p-type B-doped silicon substrate (100) with resistivity of 1-10 Ωcm with different current densities and time to achieve various porosities. Black and red lines present IR spectra of PSi30 with a porosity of 67.1% and a refractive index of 1.64 and PSi34 with a porosity of 49.4% and a refractive index of 2.18, respectively.

2.5 Raman Spectroscopy

Raman spectroscopy is the inelastic scattering of light. The vibrational Raman scattering was discovered in 1928 by the Indian physicist C.V. Raman [29]. Raman scattered light is frequency-shifted with respect to the excitation frequency, but the magnitude of the shift is independent of the excitation frequency. In this section, Raman scattering has been used to examine the surface termination of PSi with complementary to the FTIR technique. The vibrational Raman mechanism involves an interaction of photons with phonon modes and the energies can either lose (Strokes) or gain (anti-Strokes) relative to the excitation energy, as

Table 2.4: Common infrared bands associated with porous silicon [13, 27, 28]

Frequency (cm^{-1})	**Species**	**Mode**
2965	Si-CH_3	antisymmetric stretching C-H
2927	Si-CH_2	antisymmetric stretching C-H
2898	Si-CH_3	symmetric stretching C-H
2856	Si-CH	antisymmetric stretching C-H
2248	O_3-SiH	antisymmetric stretching Si-H
2200	O_2-SiH_2	symmetric stretching Si-H
2160	$OSiH_3$	stretching Si-H
2108	Si-H_2	stretching Si-H
2087	Si-H_1	stretching Si-H
1463	Si-CH_3	antisymmetric deformation CH_3
1252	Si-CH_3	symmetric deformation CH_3
1056-1160	Si-O-Si	symmetric stretching Si-O-Si
980-1050	Si-O-Si	antisymmetric stretching Si-O-Si
948	Si_2H-SiH	bending Si-H
906	Si-H_2	symmetric scissor Si-H_2
856	Si-H_2	wagging Si-H
812	Si-F	symmetric Si-F
800	Si-O-Si	bending Si-O
681	Si-CH_3	stretching Si-C
665	Si-H_x	wagging Si-H_2
628	Si-H_x	bending Si-H

shown:

$$\hbar\omega_s = \hbar\omega_i \pm \hbar\omega_{phonon}.$$

Here $\hbar\omega_s$, $\hbar\omega_i$ and $\hbar\omega_{phonon}$ are the energy of Raman shift, the incident photon and the phonon, respectively.

In classical model, an incident electromagnetic wave with frequency υ_0 is given by

$$\vec{E} = \vec{E_0} \cos 2\pi\upsilon_0 t,$$

where $\vec{E_0}$ is the maximum value of the electric field and t is time. Considering the dipole moment $\vec{p}$ of the molecule,

$$\vec{p} = \vec{\mu_0} + \vec{\mu}, \tag{2.8}$$

and

$$\vec{\mu} = \alpha \vec{E}, \tag{2.9}$$

where $\vec{\mu_0}$ is a permanent dipole moment, $\vec{\mu}$ represents an induced dipole moment and α is the molecular polarisability [30]. The polarisability, which is the change of the molecule charge distribution caused by an external electric field, is a rank 2 tensor α_{ij}. When the light is incident on the molecule therefore

$$\vec{p} = \vec{\mu_0} + \alpha_{ij} \vec{E_0} \cos 2\pi\nu_0 \, t. \tag{2.10}$$

The change in polarisability of the electron cloud causes a small displacement so using a Taylor series expansion, α_{ij} can be estimated by

$$\alpha_{ij} = \alpha_{0ij} + \left(\frac{\partial \alpha_{ij}}{\partial Q_k} \right)_0 Q_k. \tag{2.11}$$

Here Q_k is the set of nuclear displacements due to the vibrational mode in a simple harmonic motion and can be expressed, $Q_k(t) = Q_{k0} \cos(2\pi\nu_{vib} \, t)$, where ν_{vib} is the vibrational frequency. Then the dipole moment becomes

$$\vec{p} = \vec{\mu_0} + \alpha_{0ij} \vec{E_0} \cos(2\pi\nu_0 \mathrm{t}) + \vec{E_0} \, Q_{k0} \left(\frac{\partial \alpha_{ij}}{\partial Q_k} \right)_0 \cos(2\pi\nu_{vib} t) \cos(2\pi\nu_0 \mathrm{t}) \tag{2.12}$$

and

$$\vec{p} = \vec{\mu_0} + \alpha_{0ij} \vec{E_0} \cos(2\pi\nu_0 \mathrm{t}) + \frac{\vec{E_0} \, Q_{k0}}{2} \left(\frac{\partial \alpha_{ij}}{\partial Q_k} \right)_0 \left[\cos 2\pi(\nu_0 + \nu_{vib}) \, t \, + \, \cos 2\pi(\nu_0 - \nu_{vib}) \, t \, \right]. \tag{2.13}$$

The first term in equation 2.13 is the permanent dipole moment. The others vary with three different frequencies ν_0, $\nu_0 - \nu_{vib}$ and $\nu_0 + \nu_{vib}$ which relate to Rayleigh, Stokes and anti-Stokes scattering, respectively.

Although the classical framework correctly predicts the frequency of the Raman scattering, the relative intensities of Stokes and anti-Stokes signals should not be equal according to Boltzmann distribution. This can be described by a quantum mechanical approach such that the vibrational energy states of molecule (E_{vib})are quantised and given by

$$E_{vib} = h\nu_{vib}(n_{vib} + \frac{1}{2}), \tag{2.14}$$

where h is the Planck constant, ν_{vib} is the frequency of the vibrational mode and n_{vib} is the vibrational quantum number ($n_{vib} = 0, 1, 2, \ldots$). The incident photons induce the molecular system into an excited virtual state (or an eigenstate of the electronic system). The interaction with the phonon arises then as the remaining energy decays via either Stokes or anti-Stokes scattering. Mostly, the molecular system is found in the ground vibrational state therefore the phonon is absorbed by the molecule and the system emits the outgoing photon with lower energy (Stokes shift). On the other hand, if a molecule is originally located in the excited vibrational state, during scattering, the phonon is emitted by the molecule. This causes the outgoing photon to radiate at higher energy (anti-Stokes shift), which process is not always possible. At normal temperatures, very few molecules occupy the excited vibrational state hence the chance of the anti-Stokes shift is much smaller than the Stokes scattering. This leads to a reason why the relative intensities is not equal, expressed as [31]:

$$\frac{I_{anti-Stokes}}{I_{Stokes}} = \left(\frac{\omega_i + \omega_{phonon}}{\omega_i - \omega_{phonon}}\right)^4 \exp\left(-\frac{\hbar\omega_{phonon}}{kT}\right), \tag{2.15}$$

where $I_{anti-Stokes}$, I_{Stokes}, k and T are respectively anti-Stokes, Stokes scattering intensities, Boltzmann constant and temperature.

Raman spectroscopy is an excellent tool to study nanocrystalline structures. Disorder and size of crystalline determine the shapes of Raman lines from microcrystalline semiconductors [32].Many articles have supported a phonon confinement model [32, 33, 34, 35]. According to Fig. 2.12, in bulk crystalline Si (c-Si), the first order Raman scattering at optical phonon in the center of the Brillouin zone is shifted by 522 cm^{-1} (left side) : the spectrum shape is symmetric and has a natural linewidth of 3.5 cm^{-1} at room temperature [36]. In nanoscale particles, the translation symmetry of the ideal crystal is disturbed and the momentum conservation law is weakened. When a phonon is confined within a space ΔL, the momentum uncertainty principle is given by $\Delta q \, \Delta L \sim 1$. Therefore, phonons near the momentum uncertainty around the center of the Brillouin zone become Raman active (as shown in right side of Fig. 2.12). This means that in nanosize particles (thus larger Δq) the Raman spectrum shifts to lower energies and broadens. Consequently, the Raman spectroscopy can be used to estimate the shape and the size of Si nanocrystals. According to the Gaussian confinement model of Richter et al [36] and following Campbell et al [32] for a spherical nanoparticle with diameter L, the first order Raman spectrum can be written as:

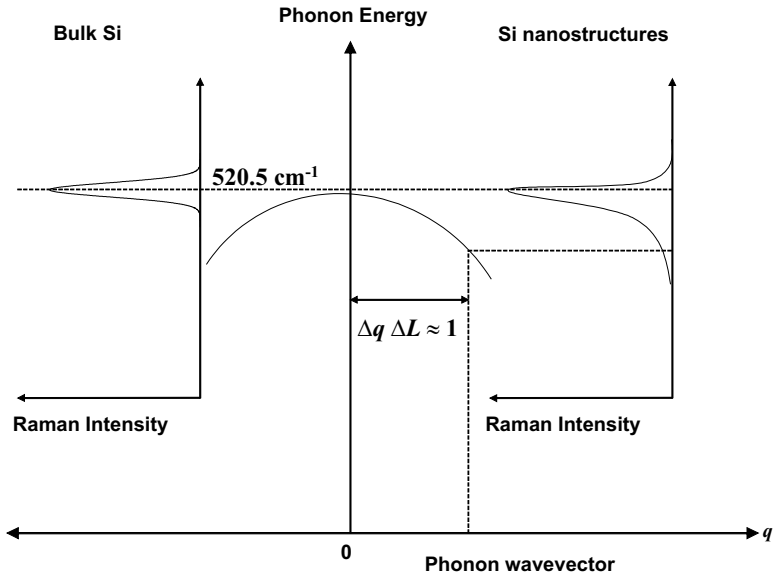

Figure 2.12: Schematic diagram of phonon dispersion relation. Left side is Raman spectrum of crystalline silicon

$$I(\omega) = \int_0^q \frac{exp(-q^2L^2/4)}{\left[\omega - \omega(q)\right]^2 + (\Gamma_0/2)^2} d^3q, \tag{2.16}$$

where q is expressed in units of $2\pi/a$, a is the lattice constant with equal to 0.54 nm, Γ_0 is the natural linewidth of c-Si (3.6 cm^{-1}) at room temperature and $\omega(q)$ is the dispersion relation of optical phonons in c-Si. We can calculate the Raman spectrum of PSi and estimate the size of Si nanocrystals by considering the optical phonon dispersion $\omega(q)$ to be isotropic and approximated in form as

$$\omega^2(q) = A + B\cos(\frac{\pi q}{2}). \tag{2.17}$$

Here $A = 1.714 \times 10^5 cm^{-2}$ and $B = 1.000 \times 10^5 cm^{-2}$ were determined by neutron scattering measurements [37]. The parabolic form of the dispersion curve also

$$\omega(q) = \omega_0 - \beta q^2, \tag{2.18}$$

has been used to simplify equation 2.16 as well [34]. Here ω_0 is the center phonon wavenumber of bulk silicon(521.5 cm^{-1}) and β is 120 cm^{-1}.

The Raman scattering measurements were carried out using a Renishaw inVia Raman Microscope using 532 nm and 785 nm excitation wavelength at room

temperature. The Raman spectra were obtained by using a 50× optical microscope objective with various power density of the laser. However, the high laser power can increase the local temperature of PSi and the influence of this heating effect also creates the asymmetrical line shape and the shift of Raman peak in silicon nanocrystal due to the anharmonic phonon processes [38, 39]. Figure 2.13 demonstrates the normalised Raman spectra of a PSi sample with different power densities. As shown in figure 2.13, increase of the power density leads to a broad

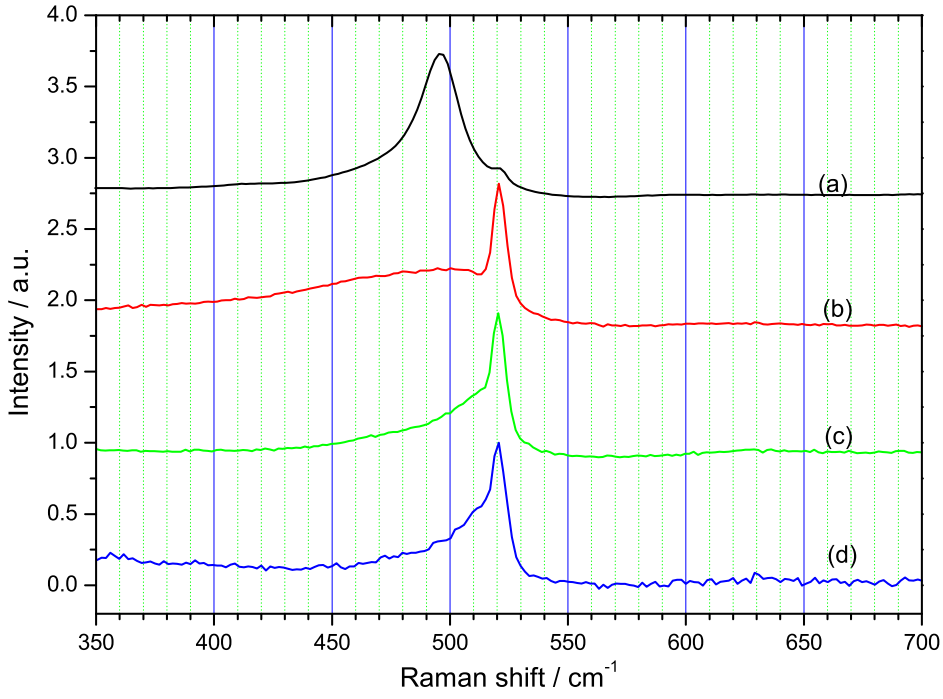

Figure 2.13: Normalised Raman spectra of the PSi500 which was exited by the 532 nm laser with different laser power. (a) by $\approx$ 200 mW/cm^2; (b) by $\approx$ 100 mW/cm^2; (c) by $\approx$ 20 mW/cm^2 and (d) by $\approx$ 10 mW/cm^2

low-frequency shift of the Raman spectra from 520 cm^{-1} at the lowest power density to 495 cm^{-1} at the highest power density and the increased full-width from 6.0 cm^{-1} to 18.0 cm^{-1}. This significant change is due to the local heating effect. Therefore, to avoid the laser heating effect, the measurements were carried out at the lowest power density.

Figure 2.14 shows the Raman spectra from the porous silicon and the bulk silicon with the 532 nm excitation wavelength at $\approx$ 10 mW/cm^2. The crystalline silicon spectrum has a symmetric line shape which is peaked at 522.5 cm^{-1} with a full

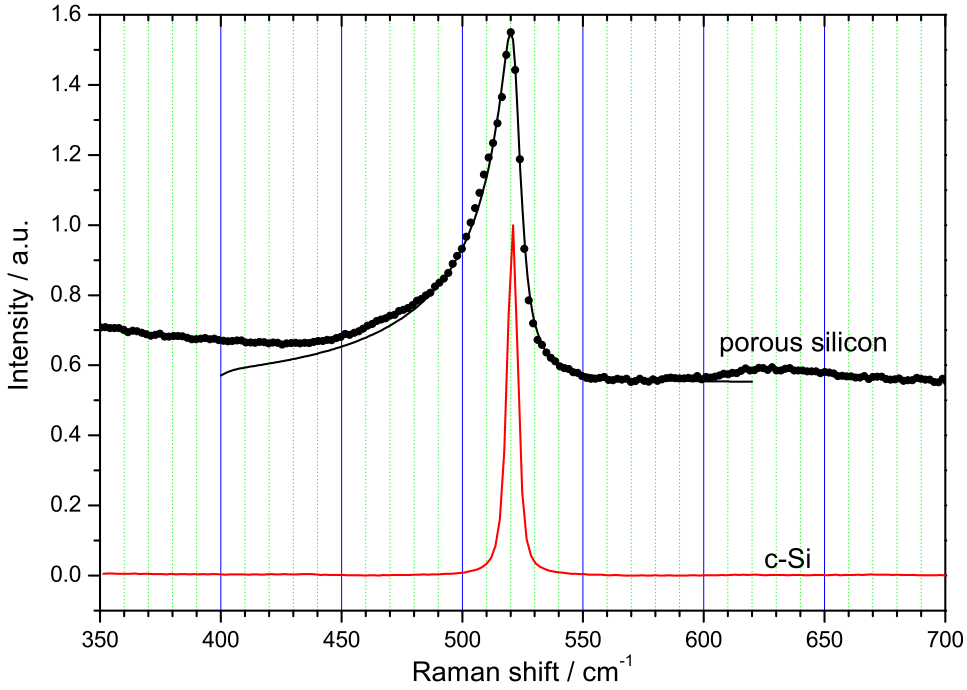

Figure 2.14: Measured and calculated Raman spectra of porous silicon is presented by circle and solid line, respectively. The bulk crystalline silicon is also included in the figure.

width at half maximum (FWHM)of 3.6 cm^{-1}. In contrast with the bulk silicon, a broad and downward shift were observed in Raman spectrum of porous silicon. The Si nanocrystal peak (circle) shows a down-shift of about 3 cm^{-1} relative to the peak of c-Si and a FWHM in the range of 7.5 to 7.6 cm^{-1}. For the sake of simplicity, we assume that Si nanocrystals have spherical grains and we then can determine the size of Si nanocrystals (L) using equation 2.16. The black-solid line in figure 2.14 is a calculated spectrum that the best fit applied for both phonon dispersions. The average diameters of Si nanocrystal using equations 2.17 and 2.18 are 2.75 nm and 2.70 nm, respectively. Clearly, there is no significant difference between the fitting result from both dispersion equations.

Compared with the SEM image of this sample in figure 2.15, the images indicate that the grain size is in order of 20 to 40 nm which is more than 10 times larger than the calculated result. However, the difference between these two values does not mean that the calculation is wrong. A possible explanation for this might be that the porous silicon sample has been oxidised, therefore, the images from

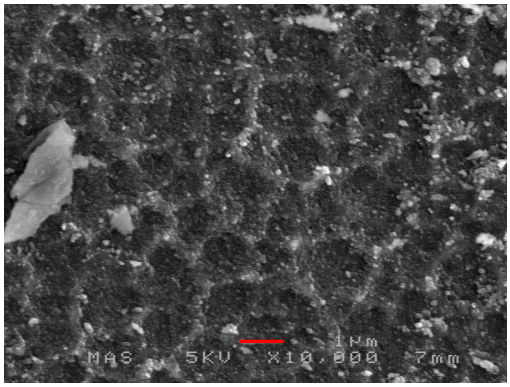

(a)

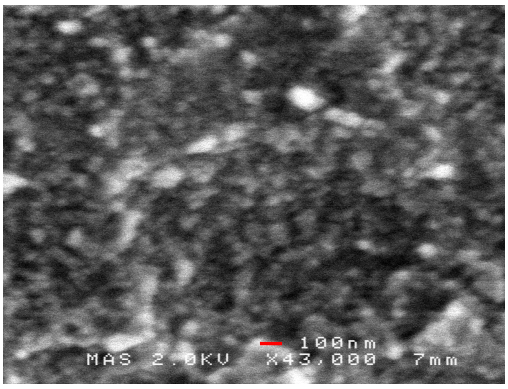

(b)

Figure 2.15: SEM top-view images of PSi sample.(a) has magnification of ×10,000 with the scale bar of 1 μm. (b) has magnification of ×43,000 with the scale bar of 100 nm.

the SEM do not exactly show the pure Si nanocrystals. Several studies have investigated the oxide thickness and have shown that it is about 10% to 25% of the total size of the oxidized particle depend on the size of silicon nanoparticle, temperature and time[40, 41, 42]. Appling this assumption to our case with the 20 nm approximate grain size, the ideal oxide layer should be 2 to 5 nm. Hence, the estimate size of actual silicon nanocrystals would be 10 to 16 nm. Although, the calculated size by Raman measurement might not agree well with the SEM measurements, the photoluminescence (PL) analysis also reflects the quantum-confinement effect and indicates the few nm size of the Si nanocrystal [13]. The PL measurements will be discussed in section 2.6.

However, there is no excitation wavelength factor in the phonon confinement model. Considering the Raman spectra as a function of excitation wavelength, figure 2.16 shows three PSi Raman spectra which were measured at two different excitation wavelengths. A narrowing of the spectra and a reduced peak shift at longer excitation wavelength were observed on all samples. Table 2.5 presents the

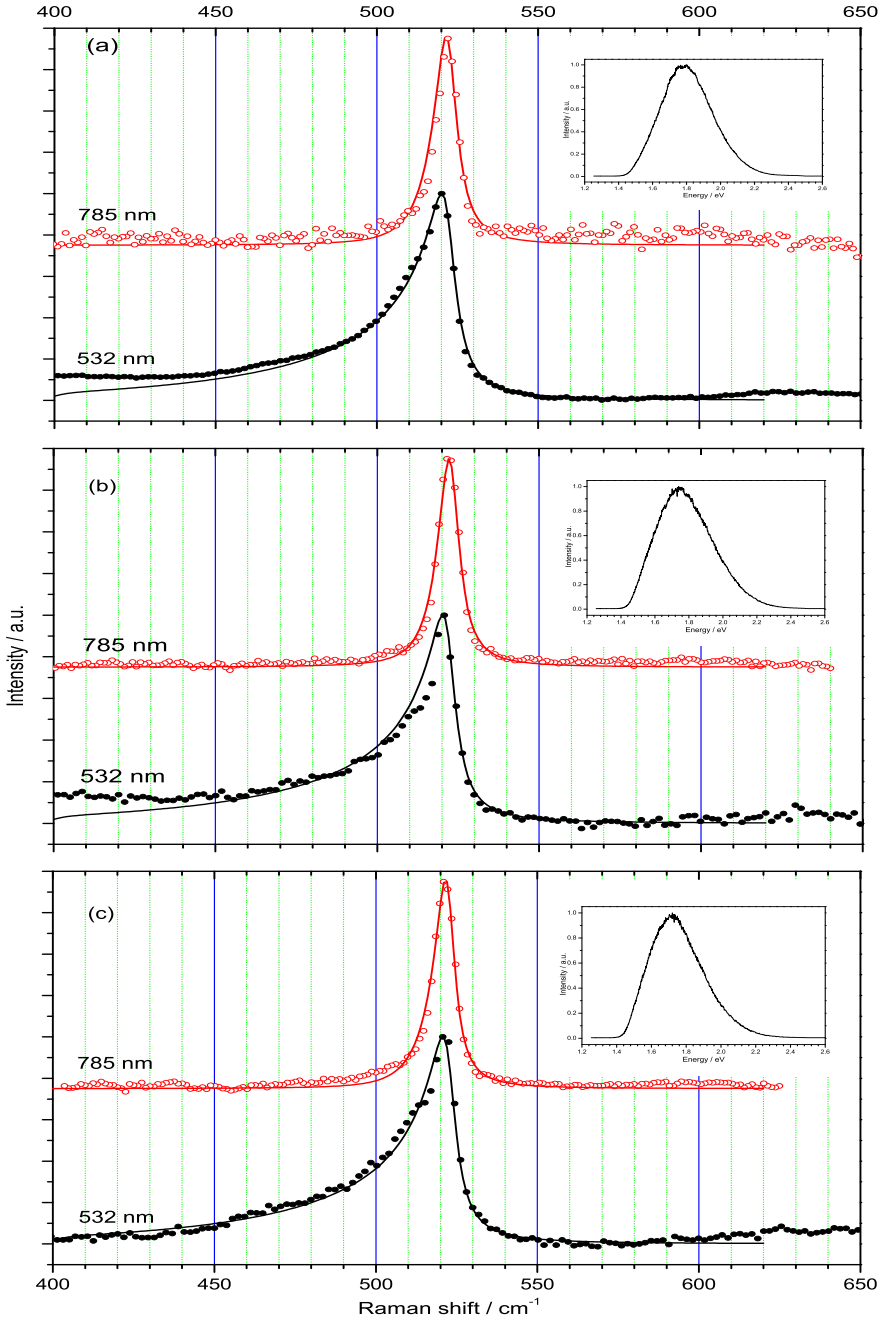

Figure 2.16: Measured and calculated Raman spectra of three porous silicon films at 532 and 785 nm are presented by circle and solid line, respectively. Insets are the PL spectra excited by 450 nm (2.76 eV) : (a) PSi350, (b) PSi500 and (c) PSi2501

results of PSi samples obtained from the fitting by the two excitation wavelengths. It seems possible that these results are due to the fact that the excitation beam

Table 2.5: Calculated particle size and basic parameters from Raman measurement by 532 nm and 785 nm excitation wavelength

Excitation wavelength (nm)	**sample**	**Raman shift (cm^{-1})**	**FWHM (cm^{-1})**	**L (nm) eq.2.17**	**L (nm) eq.2.18**
532	350	3.0	7.6	2.75	2.70
	500	2.5	7.0	2.90	2.70
	2501	2.0	7.0	2.70	2.70
785	350	1.0	7.0	9.80	10.4
	500	0.3	6.3	12.0	12.5
	2501	1.0	5.9	8.80	9.60

penetrates deeper at longer wavelengths. Assuming that porosity decreased with depth, therefore, the narrowing of the spectra could be dominated by the larger grains from the deeper surface or the c-Si from the substrate. In order to examine this explanation, a depth series Raman experiment was carried out at 532 nm and 785 nm excitation. Comparisons between the two wavelengths at different

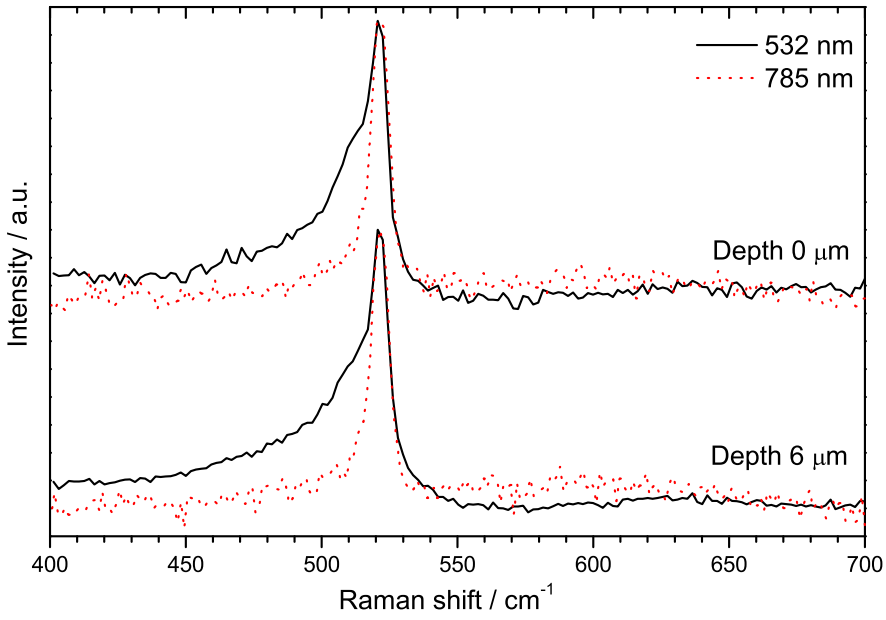

Figure 2.17: Normalised Raman spectra of porous silicon film at 532 and 785 nm excitation wavelength which are presented by a black solid line and a red dot line, respectively, at different layer depths.

layer depths were shown in figure 2.17. It is apparent from this result that the

Raman line shape depends on the excitation wavelength and the spectra with 532 nm excitation are always broader than the spectra with 785 nm excitation. Also, several studies have revealed that, even for the free standing PSi samples, this Raman feature was still detected [43, 44, 45]. Therefore, the different penetration depth model can not explain these results.

It is apparent from the insets in figure 2.16 that the PL spectra are very broad and lie in region of 1.4 to 2.5 eV. This indicates the various sizes of PSi grains which give another possible explanation for the dependence of excitation wavelength in the Raman feature as follows. Due to the size distribution of the samples, resonant Raman scattering (RRS) must play a major role in this case. When the excitation energy matches the band edge of a certain particle size, these associated particles will dominate the Raman spectrum due to the RRS effect. The higher energy will excite smaller nanoparticles as appeared in figure 2.16. Therefore, the excitation wavelength dependent of Raman scattering originates from the resonance size-selection effect which is corresponding with the size distribution of Si nanoparticles.

2.6 Photoluminescence Spectroscopy

Photoluminescence(PL) spectroscopy is a nondestructive technique that is used for investigating and probing the electronic states of semiconductors. When the photo-excitation energy is higher than the energy gap of the semiconductor, electrons within the valence band will move into permissible excited states and create electron-hole pairs. The energy can be released when these electrons return to their equilibrium state. This process may occur with the emission of light (a radiative process) or without (a nonradiative process). In radiative recombination, the PL energy corresponds to the difference in energy levels between this transition.

The experimental setup is shown in figure 2.18. A solid-state 450 nm laser is used to excite PSi samples ,which can be replaced with an 488 nm argon ion laser or a Verdi V6 solid-state laser (532 nm). Light entering the cryostat is linearly polarized. The sample holder is interchangeable; data shown in this report was taken mainly in the backscattering configuration shown in the inset of figure 2.18

as this helps to limit the stray laser light that is elastically scattered from the sample.

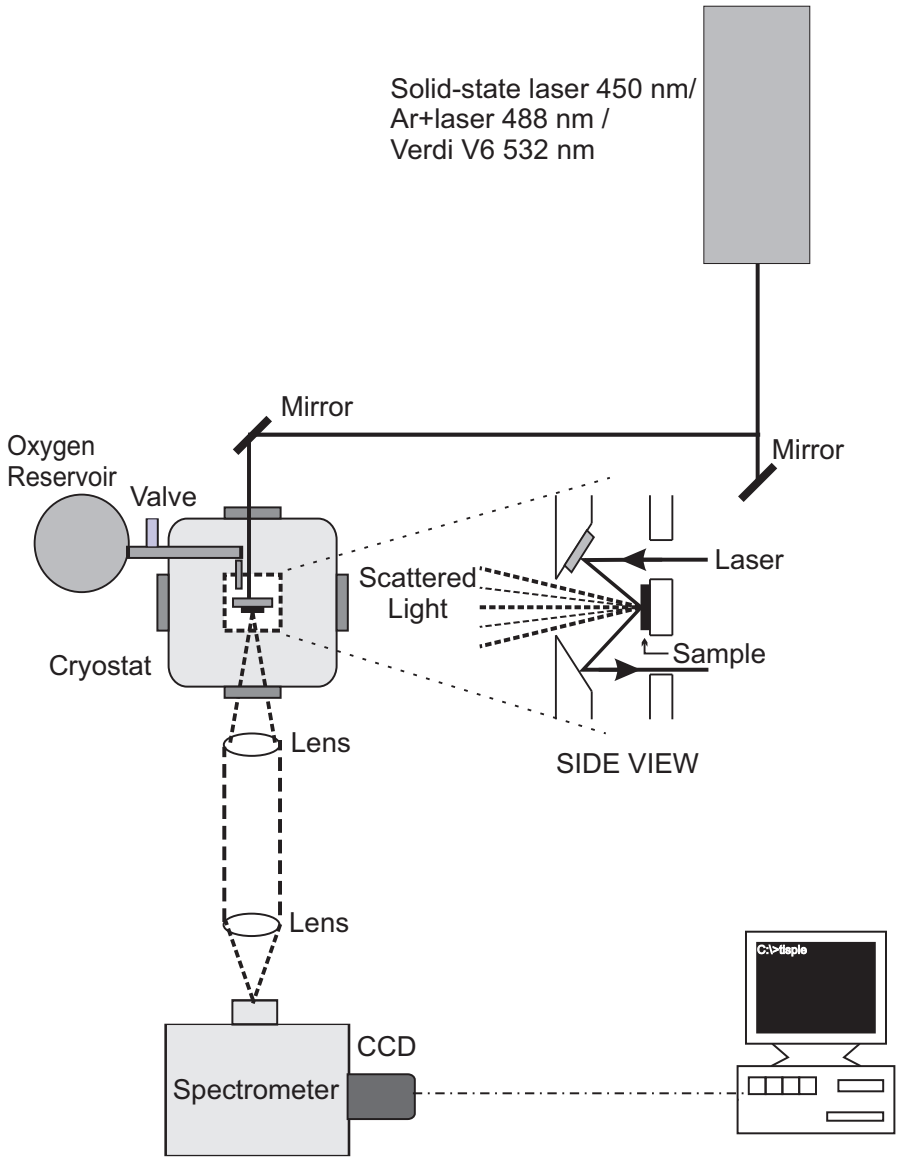

Figure 2.18: Sketch of a photoluminescence experimental setup. The image is edited with thanks to L.C. Smith.

The cryostat (Oxford Instruments Spectromag) contains a 6T split coil magnet allowing for easy optical access on all sides of the sample. In the centre of the magnet the sample sits in a liquid helium bath at a temperature of 1.5K. This is cooled by a larger surrounding liquid helium bath and a liquid nitrogen bath. The outer chamber of the magnet is evacuated as a final layer of insulation. The entire cryostat can be rotated through 90° to perform experiments in either Faraday or Voigt geometry meaning that the magnetic field (**B**) is applied perpendicular or

parallel to the sample surface, respectively. To investigate the effect of molecular oxygen adsorbed into a surface of Si nanocrystals measurement, an oxygen reservoir was used to supply O_2 into the sample space which can controlled by a valve connected between the reservoir and the sample space.

After the cryostat, light from the sample passes through the lenses which are used to collect the scattered light entering through the single spectrometer that can detect the spectral range from 1.2 to 3.0 eV. A charge coupled devices (CCD) (Princeton instruments CCD 512TK) camera was used to recorded the results as intensity vs position, and was calibrated to read intensity vs wavelength. This CCD camera can detect spectra in the NIR and visible spectral range.

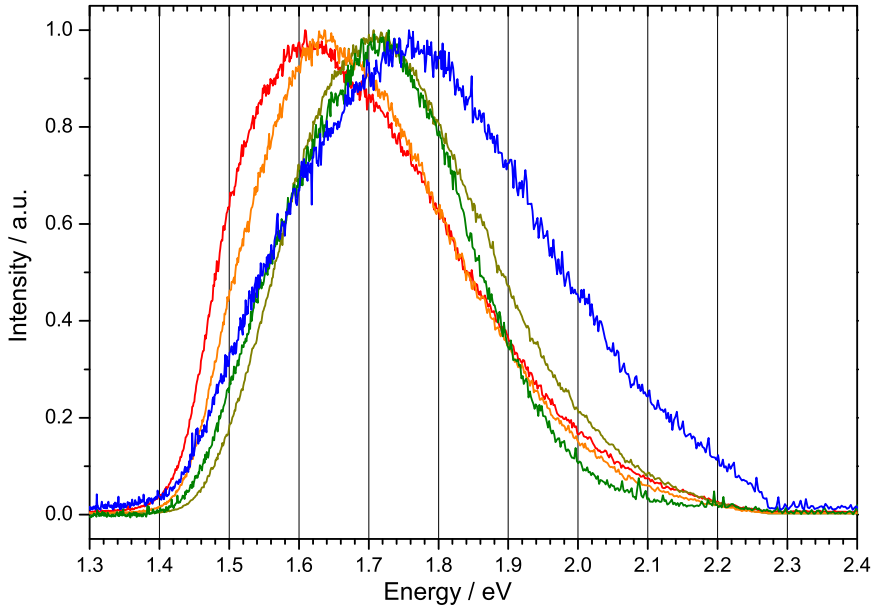

Figure 2.19: Normalised PL spectra of the different PSi samples at room temperature, $E_{ex} = 2.755$ eV. The PL spectra show the tunability of the PL band of PSi films with different etching conditions.

In early 1990s, Canham reported efficient visible photoluminescence (PL) from porous silicon at room temperature and interpreted this phenomenon as arising from quantum confinement effect [2]. Then in 1991, Lehmann and Gösele also identified that an increase of the effective band gap energy is due to the quantum confinement effect [3]. The tunability of the PL band in PSi is controlled by the size of nanocrystals which, due to the formation process, have a large size

distribution. Therefore, the emission is in a broad energy range with FWHM of about 300 to 400 meV as presented in figure 2.19. The SEM images in section 2.3.1 also indicate the wide size distribution of our samples. Obviously, the emitting states of Si nanocrystals are driven to higher energy by the quantum confinement effect [46, 47, 48]. When the Si nanocrystal size is smaller, the band gap should increase and the PL spectrum moves to the blue as shown in figure 2.19 in which the blue spectrum arises from the smaller average size of Si nanoparticle than the red solid spectrum. Table 2.6 shows the lists of luminescence bands from

Table 2.6: Porous Si luminescence band adapted from [49]

Spectral range	**Peak wavelength (nm)**	**Luminescence band label**
UV	~ 350	UV band
blue-green	~ 470	F band
blue-red	400-800	S band
near IR	1100-1500	IR band

PSi samples. In this research, we focus on the "S band" luminescence, for which the emission lifetime is in order of microseconds. By contrast, the "F band" has fast decay time of a few nanoseconds. It has been suggested that the F band originates from the oxidised PSi [50]. For infrared emission, it has been proposed that it can arise from dangling bonds [51]. Also the UV band has been observed from oxidised PSi which can relate to defects in oxide layer [49]. In order to emit S band luminescence, the dominant size of the PSi samples must be on the scale of quantum-sized Si particles [13, 49, 52].

2.6.1 Time resolved measurements

In order to understand the luminescence process of PSi, the time dependence of the PL from PSi is one of the most important factors to investigate. The time evolution of PL intensity measurement was set up as in figure 2.20 in order to investigate continuous illumination during set time intervals. The laser light passes through a mechanical light chopper which is used to trigger a lock-in amplifier. A gated intensified CCD has been employed for this technique, which has a time resolution of 5 ns. The measurement gate width and the delay time can be varied from ns to ms in order to observe PL intensity.

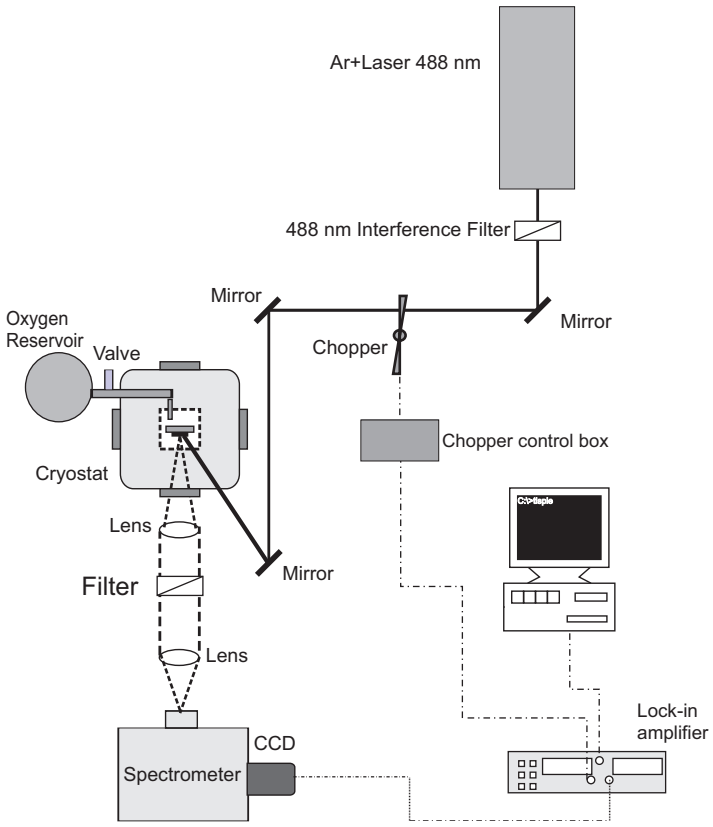

Figure 2.20: Sketch of a time-evolution experimental setup for PSi.

Figure 2.21 shows the results from the time evolution measurements of PSi at room temperature. The dashed arrow line shows that the PL intensities decrease with increasing of delay times. Inset are the PL decays of the different energy emissions which clearly shows the strong dependence between the decay times and the detection energy. The lifetimes become shorter with increasing detection energies. From time-resolved studies, PL decay profiles are multi-exponential [46] and can be modeled by using a stretched exponential function [53, 54]:

$$I_{PL}(t) \; = \; I_0 \exp[-t/\tau]^{\beta}, \tag{2.19}$$

where $I_{PL}(t)$ is the luminescence intensity, I_0 is the luminescence intensity at $t = 0$, τ is the PL lifetime and $\beta \leq 1$ is a dispersion exponent. This suggests a distribution of recombination rates at the same emission energy. The inset of figure 2.21 shows the multi-exponential behaviour which is typical for PSi samples. To calculate the lifetime (τ), the fitting by the stretched exponential in equation 2.19 is presented in the inset of figure 2.22.

Figure 2.22 shows the decay times range from 2.0 μs at 2.2 eV to 13 μs at 1.63 eV

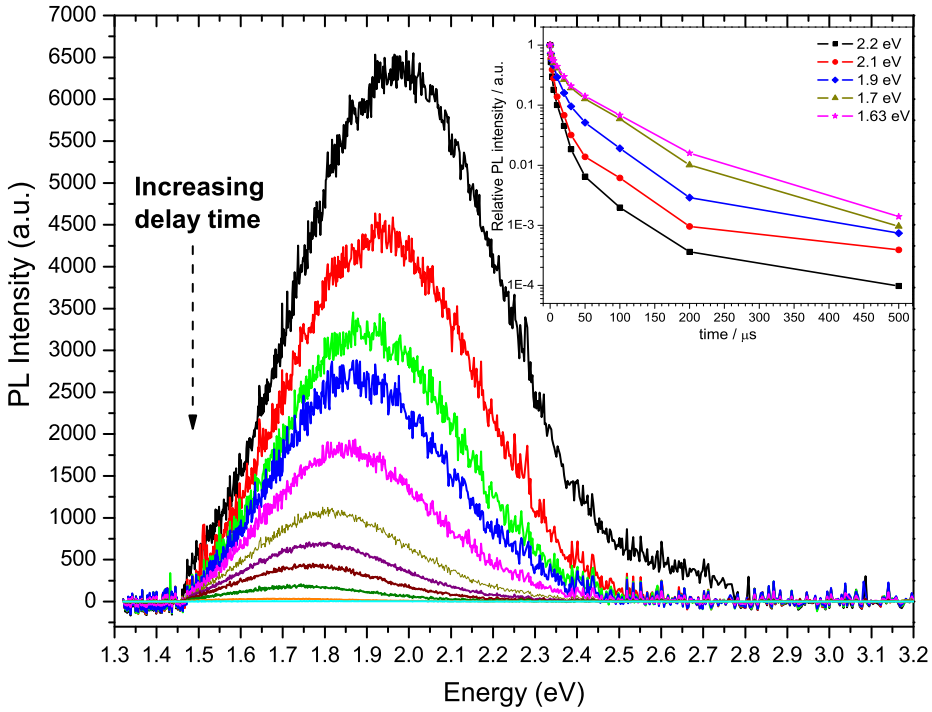

Figure 2.21: Time evolution PL spectra of PSi at room temperature. Inset is the normalised PL decays at the selective detection energy as indicated (the solid lines are the guiding line to the eyes) . The excitation energy is 2.54 eV.

which the lifetime at the lower emission energies is six times longer than the lifetime at the higher energy. This result supports the quantum confinement model and can be explained as follows: when the size of Si nanocrystals decreases (corresponding with the higher energies) , their electron-hole wave functions overlaps more in momentum space than in large particles (equivalent to the lower energies). Therefore, with stronger confinement, faster quasi-direct exciton recombination arises. Nevertheless, the room temperature lifetime in PSi is longer than in direct gap semiconductors (typically, in order of nanosecond). This suggests that PSi is still an indirect bandgap semiconductor. The lifetime of PSi is strongly temperature dependent [49, 53, 54, 55].

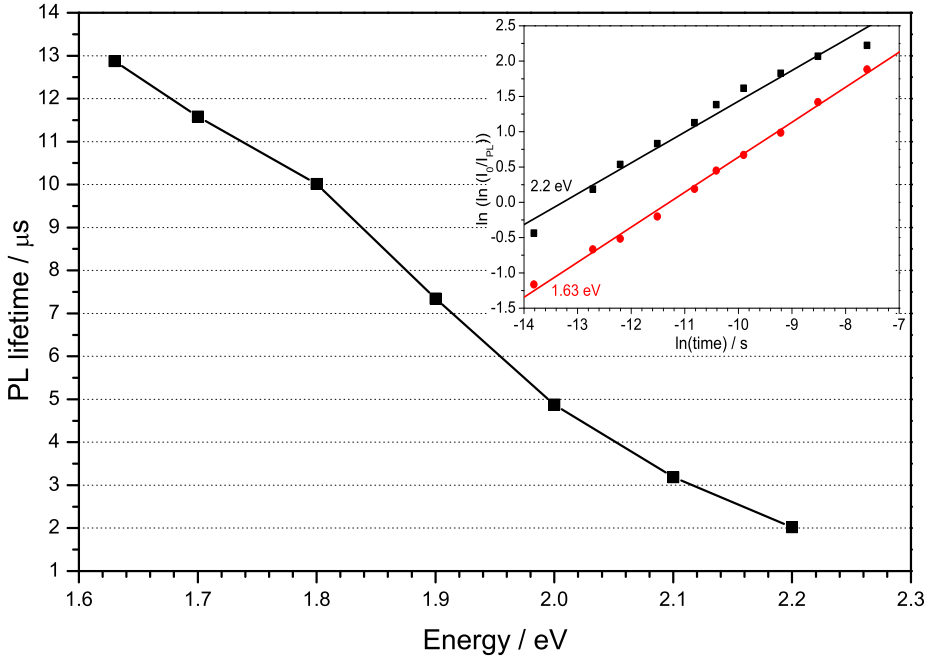

Figure 2.22: Spectral dispersion of the exciton lifetime of PSi at room temperature. The connecting line is for guiding the eyes. Inset shows the stretched exponential fits of the PL decay at 2.2 and 1.63 eV by using the stretched exponential model.

2.6.2 Frequency resolved measurements

The frequency-resolved spectroscopy (FRS) has been used to examine the temperature dependence of PSi lifetime [56]. The experimental setup is presented in figure 2.23. A PSi sample was installed in a closed-cycle cryostat which can cool the system down to 10 K. The 532 nm laser was modulated sinusoidally by an acousto-optic modulator (AOM) over a range of frequencies from $10Hz$ to $100kHz$. The PL was detected by a photomultiplier at photon energies of 1.52 eV to 1.91 eV and the in-phase signal was obtained by a SR400 gated photon counter which was triggered by a function generator that provides the frequency up to $15MHz$.

The experiment was set to measure the lifetime at various PL photon energies in the range 1.52 eV to 1.91 eV, and over the temperature range 10 K to 292 K. Figure 2.24 presents the intensities of the in-phase signal of FRS as a function

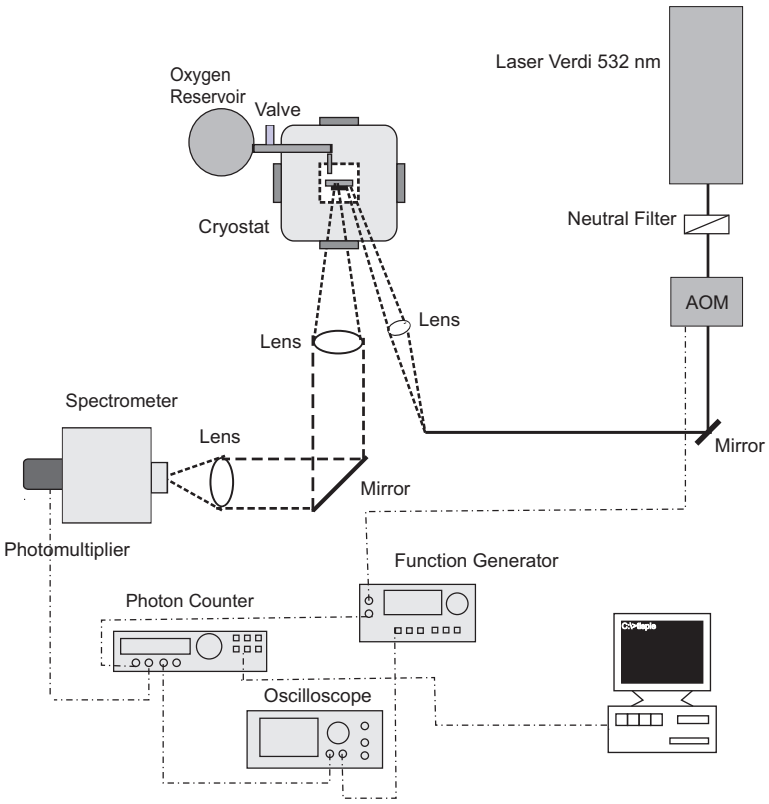

Figure 2.23: Sketch of a frequency-resolved experimental setup for PSi.

of frequency with varying temperatures at PL energy of 1.78 eV. It is apparent from the graph that the spectra are strongly temperature dependence. The FRS intensity, as shown in figure 2.24, increases with decreasing frequency then reaches a saturated point. This feature is shown in all FRS spectra at different temperatures.

A simple rate equation can be used to explain the FRS measurement as follows [56]:

$$\frac{dn(t)}{dt} = g(t) - \frac{n(t)}{\tau}, \tag{2.20}$$

where n is the number of carriers in the photoexcited state, g is the generation rate and τ is the lifetime. If the excitation is modulated at an angular frequency ω then

$$g(t) \;=\; g_0 \;+\; g_1\, e^{i\omega t}.$$

Let us assume n has a component also at $e^{i\omega t}$, hence,

$$n(t) \;=\; n_0 \;+\; n_1\, e^{i\omega t},$$

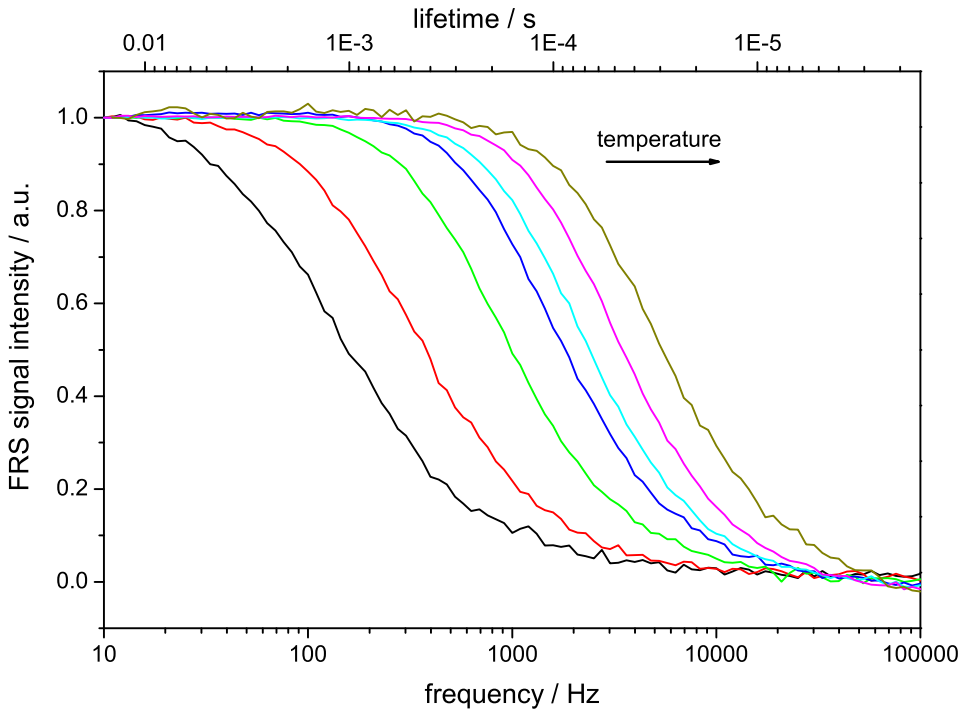

Figure 2.24: Frequency-resolved spectra with various temperatures from 10 K to 292 K increase as shown by arrow sign. Excitation energy is 2.33 eV with the power density of 44.8 mW/cm^2 at detection energy of 1.78 eV.

giving equation 2.20 as

$$0 \; + \; i\omega n_1 \, e^{i\omega t} = g_0 - \frac{n_0}{\tau} \; + \; (g_1 - \frac{n_1}{\tau}) \, e^{i\omega t}. \tag{2.21}$$

By equating coefficients of 1 and $e^{i\omega t}$, so equation 2.21 shows that

$$0 \; = \; g_0 \; - \; \frac{n_0}{\tau}, \tag{2.22}$$

and

$$i\omega n_1 \; = \; g_1 \; - \; \frac{n_1}{\tau}. \tag{2.23}$$

Equation 2.22 is the continuous wave solution which presents the rate equation in the steady state photoluminescence case. Equation 2.23 represents the FRS spectrum as a function of ω. Therefore,

$$n_1 \; = \; \frac{g_1 \, \tau}{1 \; + \; i\omega\tau}. \tag{2.24}$$

The saturation case ($\omega \; \rightarrow \; 0$) leads to $n_1 \; \rightarrow \; g_1\tau$. On the other hand, at high

frequency ($\omega \rightarrow \infty$) n_1 is equal to 0. Clearly, this response gives the limiting behaviour of the FRS spectrum as shown in figure 2.24 and 2.25. Equation 2.24 is rewritten giving

$$n_1 = \frac{g_1 \tau}{1 + i\omega\tau} = \frac{g_1\tau(1 - i\omega\tau)}{1 + \omega^2\tau^2}. \tag{2.25}$$

As shown in equation 2.25, n_1 is complex, hence, the expression of

$$|n_1| = \frac{\sqrt{g_1^2\tau^2 + \omega^2\tau^2}}{1 + \omega^2\tau^2}, \tag{2.26}$$

is exactly the value obtained from experiments. By fitting the result with this equation, the lifetime is delivered as presented in figure 2.25. Figure 2.25 shows

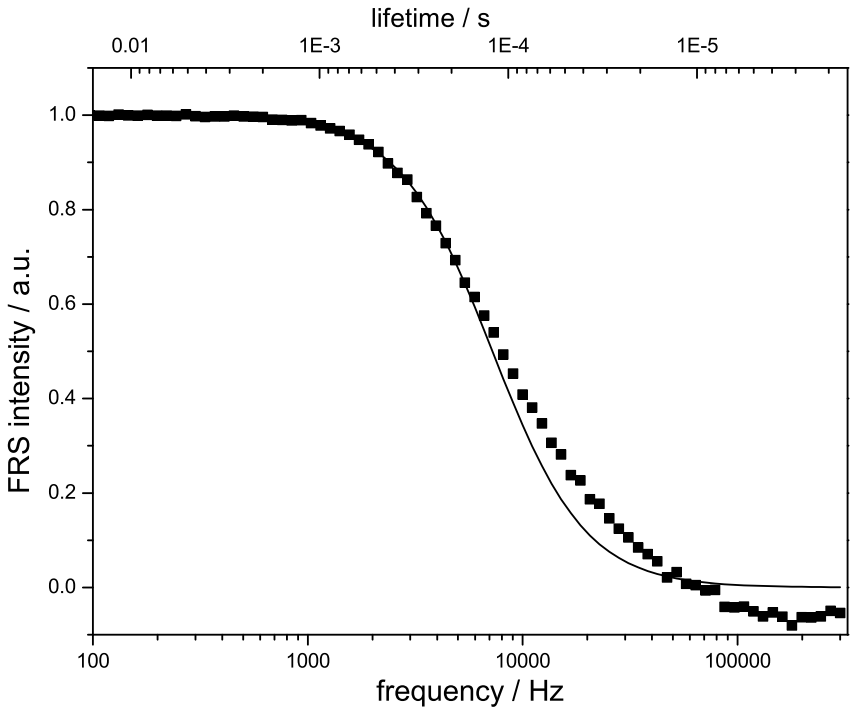

Figure 2.25: Frequency-resolved spectrum at T = 295 K. Excitation energy is 2.33 eV with the power density of 44.8 mW/cm^2 at detection energy of 1.86 eV. The square and line represent the experimental result and the fit from equation 2.26, respectively.

an example of FRS spectrum compared with the fit obtained from equation 2.26. As can be seen, the fit does not match the experimental measurement. Due to the size distribution of the PSi sample, the PL lifetime is also distributed. However, equation 2.26 holds strictly only for the single lifetime, thus, it could not fit the whole range of the frequencies as shown in figure 2.25. Nevertheless, it can still

reveal changes in lifetime distribution.

Therefore, we assume that the lifetime at the half-saturation intensity point represents an average lifetime of the sample. Figure 2.26 shows the lifetimes obtained

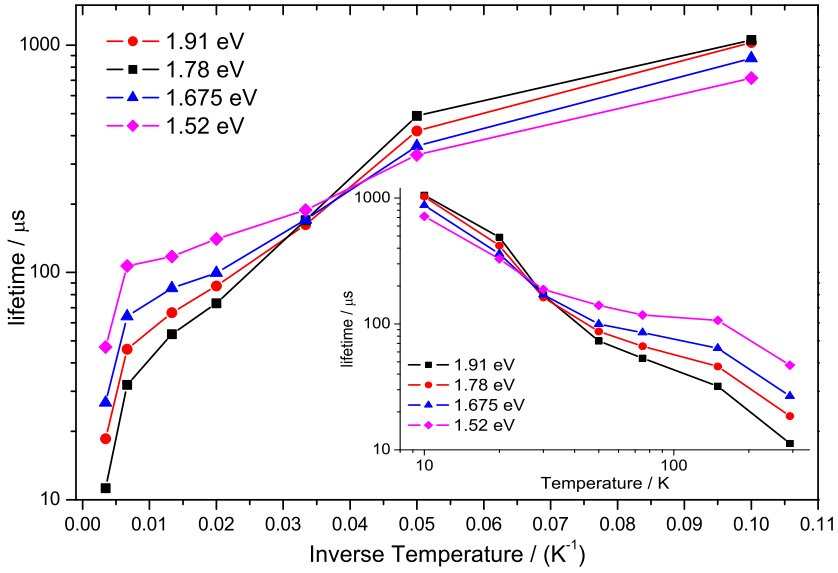

Figure 2.26: Spectral dispersion of the exciton lifetimes of PSi at various PL detection energy from 1.52 eV to 1.91 eV plotted as a function of inverse temperatures. The connecting line is for guiding the eyes. Inset is the lifetimes plotted as a function of temperature.

from the FRS measurements plotted as a function of inverse temperatures at four different PL energy. As can be seen from the results in figure 2.26, the decay times increase drastically with decreasing temperature. For example, the decay time at 1.91 eV rises from 32 μs at 150 K to 1.05 ms at 10K. It has been proposed that the temperature dependence of decay time arises from a splitting of localised exciton state into a two level system by an energy splitting Δ [55]. There are a singlet and a triplet state as an upper (τ_U) and lower state (τ_L), respectively. The lifetime (τ)can be wriiten as:

$$\tau^{-1} = \frac{3\tau_L^{-1} + \tau_U^{-1}\exp(-\Delta/kT)}{3 + \exp(-\Delta/kT)}, \tag{2.27}$$

where k is the Boltzmann constant and T is temperature. τ is assumed to be radiative decay time, however, in reality the PL decay time from the experimental

results is a combination of both radiative and non-radiative decay processes. Therefore, the PL decay time τ_{PL} can be expressed as:

$$\frac{1}{\tau_{PL}} = \frac{1}{\tau_r} + \frac{1}{\tau_{nr}} \tag{2.28}$$

and the PL quantum yield (η)

$$\eta = \frac{\tau_r^{-1}}{\tau_r^{-1} + \tau_{nr}^{-1}} \text{ or } \eta = \frac{\tau_{PL}}{\tau_r}, \tag{2.29}$$

where τ_r and τ_{nr} are the radiative and the non-radiative decay time of excitons, respectively [51]. Alternatively, we can express τ_{PL} in term of recombination rates as:

$$\tau_{PL} = \frac{1}{W_r + W_{nr}}, \tag{2.30}$$

where W_r and W_{nr} are the radiative and non-radiative recombination rates, respectively. At room and elevated temperature, non-radiative decay plays a dominant role in the relaxation process due to thermally activated transport of carriers so the carriers are able to reach the non-radiative centers [7, 49]. From figure 2.22, the decay time at room temperature is in the range of tens of microseconds which indicates that most excitons recombine within the nanocrystals and cannot reach the non-radiative centres. This conclusion further supports the idea that the high quantum yield of PSi is associated with the disability of the non-radiative process rather than the reduction of the radiative lifetime [57]. At lower temperatures than 150 K, it is clearly demonstrated from inset of figure 2.26 that the decay times rise as the temperature decreases. This suggests that the recombination process in this temperature range arises mainly from radiative transition, therefore we can apply equation 2.27 to fit the lifetime results as shown in figure 2.27.

Figure 2.27 plots $\log_{10}(\tau)$ versus inverse temperature for two PL energies (1.91 and 1.52 eV). The solid and dash lines are the result of the fits with equation 2.27 while τ_U, τ_L and are adjustable parameters. These parameters are presented in figure 2.28 and 2.29. Figure 2.28 provides the energy dependence of the energy splitting (Δ) with increasing from 5 meV at 1.52 eV to 8.5 eV at 1.91 eV. Both graphs clearly show that these parameters are intensely dependent with the PL energy. This evidence also supports the quantum confinement model as the excitons are localised which each state is split by an exchange interaction into a spin singlet and a spin triplet. In the strong quantum confinement model, the exchange

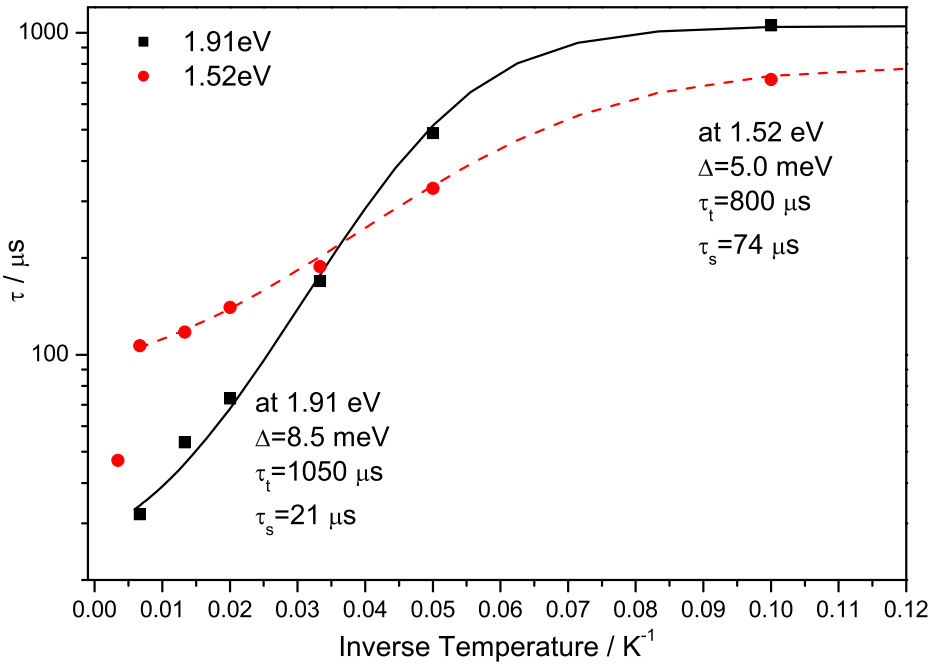

Figure 2.27: The temperature dependence of the PL lifetime. The squares and dots represent the decay time at 1.91 and 1.52 eV, respectively. The solid and dash line are the fits from equation 2.27 at 1.91 and 1.52 eV, respectively.

splitting is enhanced and consistent with the energy splitting Δ. As shown in this result, increased PL energy (small nanocrystal) lifts up Δ, which indicate that Δ is the exchange splitting, τ_U and τ_L are the singlet and the triplet lifetime, respectively [55].

This conclusion leads to an explanation of the temperature dependence of the lifetime in the inset of figure2.26 as follow. At low temperature (T$\leq$30K), the thermal energy of the excitons ($kT = 2.58meV$) is lower than the splitting energy which is 4-15 meV [55, 58] depend on the PL energy therefore the PL only arises from the triplet state. The decay time from this state is very long (in order of ms) owing to the optical forbidden transition. On the contrary, when temperature is raised ($kT >> \Delta$), the population of excitons in singlet state increases so the lifetime is shorter, in the order of μs.

Figure 2.29 plots the upper (singlet) and lower (triplet) state lifetimes against the PL energy. The lifetime of the upper state is of the order of ten μs and

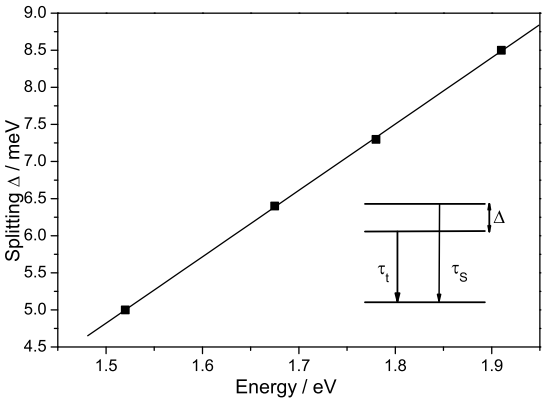

Figure 2.28: The energy splitting (Δ) between singlet and triplet states as a function of the PL energy. The line is a guide for the eyes.

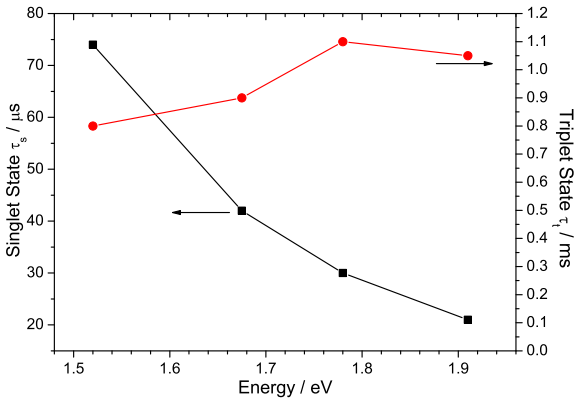

Figure 2.29: The lifetimes of the upper (τ_U) and lower (τ_L) states are represented by square and dot symbols, respectively, as a function of the PL energy.The lines are guide for the eyes.

dramatically declines at high PL energy whereas the lower state lifetime is of the order of ms. It clearly shows that the upper state lifetimes are much shorter than the lower state lifetimes. The energy dependence of the upper state lifetime is in agreement with the room temperature lifetime in section 2.6.1, which confirms the confinement effect. On the other hand, the τ_L shows the independence of PL energy (Si nanocrystals size). This could lead to an assumption that the origin of the lower state lifetime mechanism differs from the upper state lifetime. Dovrat et al. [57] proposed that nonradiative processes play a dominant role in the lower state lifetime. However, the exchange splitting model still exists and agrees with the assumption of Dovrat due to the long lifetime of the triplet state lifetime. Therefore, the lifetime of the triplet state is long and less sensitive to the nanocrystals size.

The lifetimes as a function of PL energy are presented in figure 2.30. It is apparent that the lifetimes depend strongly on the photon energy at temperatures above 50 K. In contrast to temperatures below 50 K, the PL decay lifetime is not sensitive to the PL emission energy. This implies that different factors dominate the decay process in different temperature ranges. This result is consistent and supports the above assumption about the mechanisms of decay process. As can be seen from figure 2.30 for the temperature range from 50 K to 290 K, large size nanoparticles (low PL energy) have a long decay time, then for smaller particle size, the lifetime rapidly becomes shorter. An explanation for the lifetime in

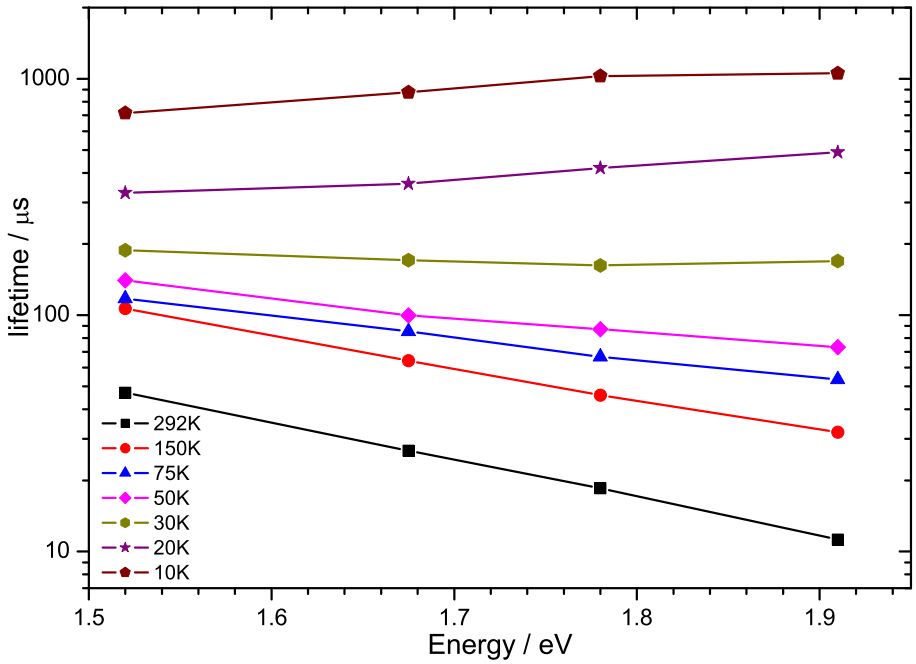

Figure 2.30: Lifetime as a function of the detected photon energy at various temperatures. The connecting lines are to guide the eye.

this temperature range is that the recombination process is dominated by the radiative process and the excitons can occupy in both singlet and triplet states according to the exchange splitting model. The transition mainly launches from the fast singlet state rather than the optical forbidden triplet state, therefore, the PL lifetimes are remarkably dependent on the emission energy in the same trend as the singlet state lifetime τ_U as shown in figure 2.29 and 2.30.

However, the low temperature range (from 30 K down to 10 K) reveals a weak dependence of the PL lifetime as a function of the emission energy. The observed independence of lifetime could be attributed to the non-radiative recombination which dominates the triplet lifetime. At this temperature, excitons have more opportunities to occupy in the triplet state rather than the singlet state, hence, the behavior of the lower lifetime τ_L plays a crucial role on the independent of these PL lifetimes as can be seen in figure 2.29 and 2.30.

The temperature dependence of the PL intensity is shown in figure 2.31. It is apparent from this graph that the PL intensity significantly increases from room

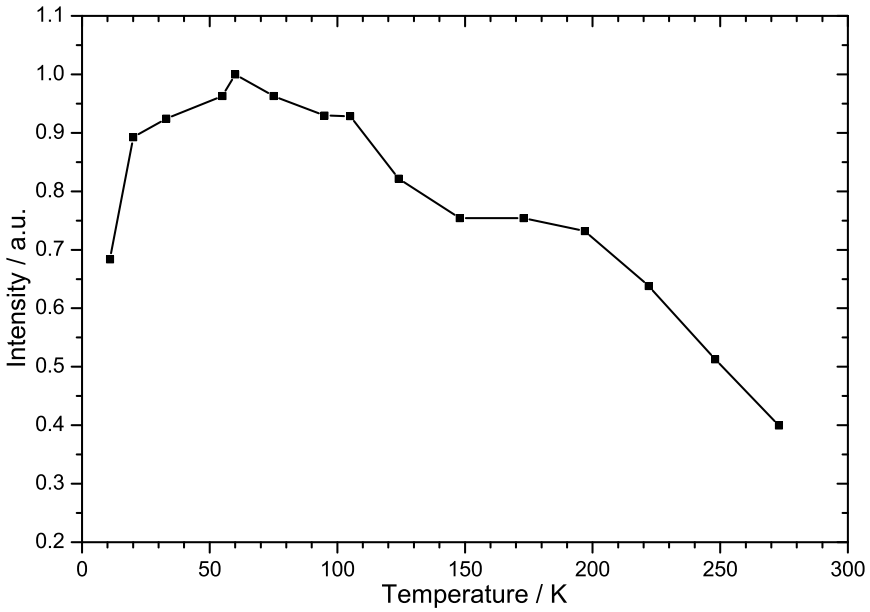

Figure 2.31: Normalised PL intensity as a function of temperature. The excitation wavelength is 2.775 eV with the power density of 44.8mW/cm^2. The line is to guide the eye.

temperature to 60 K approximately by a factor of 2 and then slightly decreases at lower temperature. It has been proposed by Suemoto et al. [59] that the slight decrease of PL intensity at the low temperature can be attributed to a slow tunneling of carriers to nonradiative centres. At higher temperatures, the radiative transition is fast enough to take over the luminescence process. This conclusion agrees well with our results and on the explanation of the decay mechanisms over the temperature range. In contrast to this assumption, however, several studies have described that the slight decline of PL intensity at lower temperature range is due to nonradiative Auger recombination when the excitation intensity is intense enough [58, 60, 61]. The exciton lifetime is extremely long at this temperature range and so there is a high chance that the next photon arrives before the excitons can radiatively recombine. According to the strong excitation intensity, the carrier density is already high, therefore, exciton recombination energy, instead of emitting photon, is used to excite the charge carrier. The nonradiative Auger recombination occurs, hence, the PL is suppressed at the low temperature.

2.7 Conclusion

In summary, porous silicon was produced by electrochemical etching. The type, doping level of bulk Si and the preparation conditions are factors that need to be considered in order to achieve the desirable PSi sample. The characteristics of PSi sample were examined by different experimental methods. SEM results reveal that PSi samples have the fir tree pore structure of about 11 μm thickness and pores sizes vary in a range from 20 to 120 nm which could be a combination of mesopores and micropores. The porosity of PSi samples were determined by gravimetric and reflection methods. The porosities are in the range of 40 to 80 %. The FTIR spectroscopy has been used to investigate the surface composition of samples. Oxidation at room temperature leads to the formation of Si-O-Si modes which show the vibrational frequency near 1,000, 1,010 and 800 cm^{-1}. The oxidation also causes the insertion of O into Si-Si back bonds, leads to the formation of O_ySiH_x species. By removing the oxide layer, refreshed PSi samples contain H-terminated surfaces as shown by Si-H_x species are observed near 2,000-2,250 and 850-950 cm^{-1}.

The Raman spectra of PSi present a down shift in energy and broad peak features which can be explained by a theoretical model of phonon confinement. Fitting from this model is used to estimate the size of Si nanocrystal to be of the order of 3 nm. The present study also reveals that the excitation wavelength dependence of Raman scattering originates from the resonance size-selection effect which is corresponding with the size distribution of Si nanoparticles. The quantum confinement model is proposed to explain the origin of the visible luminescence and high quantum efficiency of PSi. The tunability of the PL band is controlled by the size of Si nanocrystals. The time and frequency resolved measurements are used to investigated lifetime. The variation of the PL lifetime and intensity with temperature also corroborate the quantum confinement effect. Exciton lifetime is in a range of 10^{-3} to 10^{-6} s depending on temperature, which is long enough to serve as a suitable storage of energy for the photosensitising process.

References

[1] A. Uhlir. Electrolytic shaping of germanium and silicon. *Bell System Technical Journal*, 35(2):333–347, 1956.

[2] L. T. Canham. Silicon quanum wire array fabrication by electrochemical and chemical dissoution of wafers. *Applied Physics Letters*, 57(10):1046–1048, 1990.

[3] V. Lehmann and U. Gosele. Porous silicon formation: A quantum wire effect. *Applied Physics Letters*, 58(8):856–858, 1991.

[4] M. S. Brandt, H.D. Fuchs, M. Stutzmann, J. Webber, and M. Cardona. The origin of visible luminescence from porous silicon - a new interpretation. *Solid State Communications*, 81(4):307–312, 1992.

[5] J. M. Perez, J. Villalobos, P. Mcneill, J. Prasad, R. Cheek, J. Kelber, J. P. Estrera, P. D. Stevens, and R. Glosser. Direct evidence for the amorphous-silicon phase in visible photoluminescent porous silicon. *Appied Physics Letters*, 61(5):563–565, 1992.

[6] F. Koch, V. Petrovakoch, and T. Muschik. The luminescence of porous Si-the case for the surface-state mechanism. *Journal of Luminescence*, 57(1-6):271–281, 1993.

[7] J. C. Vial, A. Briesy, F. Gaspard, R. Herino, M. Ligeon, F. Muller, R. Romestain, and R. M. Macfarlane. Mechanisms of visible-light emission from electroxidized porous silicon. *Physical Review B*, 45(24):14171–14176, 1992.

[8] T. K. Sham, D. T. Jiang, I. Coulthard, J. W. Lorimer, X. H. Feng, K. H. Tan, S. P. Frigo, R. A. Rosenberg, D. C. Houghton, and B. Bryskiewicz. Origin of luminescence from porous silicon deduced by synchrotron-light-induced optical luminescence. *Nature*, 363(6427):331–334, 1993.

[9] K. A. Littau, P. J. Szajowski, A. J. Muller, A. R. Kortan, and L. E. Brus. A luminescent silicon nanocrystal colloid via a high-temperature aerosol reaction. *Journal of Physical Chemistry*, 97(6):1224–1230, 1993.

[10] M. Fujii, M. Yoshida, Y. Kanzawa, S. Hayashi, and K. Yamamoto. 1.54 $\mu m photoluminescence of Er^{3+} doped into SiO_2 films containing Si nanocrystals : Evidence for energy transfer from Si nanocrystals to Er^{3+}. Applied Physics Letters, 71(9) : 1198 - -1200, 1997.$

[11] L. Dal Negro, M. Cazzanelli, L. Pavesi, S. Ossicini, D. Pacifici, G. Franzo, F. Priolo, and F. Iacona. Dynamics of stimulated emission in silicon nanocrystals. *Applied Physics Letters*, 82(26):4636–4638, 2003.

[12] J. Ruan, P. M. Fauchet, L. Dal Negro, M. Cazzanelli, and L. Pavesi. Stimulated emission in nanocrystalline silicon superlattices. *Applied Physics Letters*, 83(26):5479–5481, 2003.

[13] M. J. Sailor. *Porous silicon in practice : preparation, characterization and applications*. Wiley-VCH, Weinheim, 2012.

[14] A. G. Cullis and L. T. Canham. Visible-light emission due to quantum size effects in highly porous crystalline silicon. *Nature*, 353(6342):335–338, 1991.

[15] X. G. Zhang. Morphology and formation mechanisms of porous silicon. *Journal of the Electrocheical Society*, 151(1):C69–C80, 2004.

[16] O. S. Heavens. *Optical properties of thin solid films*. Butterworths London, 1965.

[17] E. Hecht. *Optics*. San Francisco London : Addison-Wesley, 2002.

[18] C. Pickering, M. I. J. Beale, D. J. Robbins, P. J. Pearson, and R. Greef. Optical studies of the structure of porous silicon films formed in p-type degenerate and non-degenerate silicon. *Journal of Physics C-Solid State Physics*, 17(35):6535–6552, 1984.

[19] C. Pickering, M. I. J. Beale, D. J. Robbins, P. J. Pearson, and R. Greef. Optical-properties of porous silicon films. *Thin Solid Films*, 125(1-2):157–163, 1985.

[20] E. V. Astrova and V. A. Tolmachev. Effective refractive index and composition of oxidized porous silicon films. *Materials Science and Engineering B-Solid State Materials for Advanced Technology*, 69(SI):142–148, 2000.

[21] D. E. Aspnes, J. B. Theeten, and F. Hottier. Investigation of effective-medium models of microscopic surface roughness by spectroscopic ellipsometry. *Physical Review B*, 20:3292–3302, 1979.

[22] X. C. Zeng, D. J. Bergman, P. M. Hui, and D. Stroud. Effective-medium theory for weakly nonlinear composites. *Physical Review B*, 38(15):10970–10973, 1988.

[23] M. Herzberger and C. D. Salzberg. Refractive indices of infrared optical materials and color correction of infrared lenses. *Journal of the Optical Society of America*, 52(4):420–427, 1962.

[24] A. L. Smith. *Applied infrared spectroscopy : fundamentals, techniques, and analytical problem-solving*. New York Chichester : Wiley, 1979.

[25] A. W. Mantz. Infrared spectroscopic studies of transients. *Applied Optics*, 17(9):1347–1351, 1978.

[26] N. J. Harrick and F. K. Dupre. Effective thickness of bulk materials and of thin films for internal reflection spectroscopy. *Applied Optics*, 5(11):1739–1743, 1966.

[27] A. Borghesi, A. Sassella, B. Pivac, and L. Pavesi. Characterization of porous silicon inhomogeneities by high spatial resolution infrared spectroscopy. *Solid State Communications*, 87(1):1–4, 1993.

[28] H. Mimura, T. Futagi, T. Matsumoto, T. Nakamura, and Y. Kanemitsu. Blue-light emission from rapid-thermal-oxidized porous silicon. *Japanese Journal of Applied Physics Part 1-Regular Papers Short Notes Review Papers*, 33(1B):586–589, 1994.

[29] C. V. Raman and K. S. Krishnan. A new type of secondary radiation. *Nature*, 121:501–502, 1928.

[30] N. B. Colthup, L. H. Daly, and S. E. Wiberley. *Introduction to infrared and Raman spectroscopy*. Academic Press Inc., 1964.

[31] C. Lamberti. *Characterization of semiconductor heterostructures and nanostructures*. Boston Mass. : Elsevier, 2008.

[32] P. M. Campbell, I. H. andFauchet. The effects of microcrystal size and shape on the one phonon Raman spectra of crystalline semiconductors . *Solid State Communications*, 58(10):739–741, 1986.

[33] Z. C. Feng and R. Tsu. *Porous silicon.* World Scientific, 1994.

[34] Z. F. Sui, P. P. Leong, I. P. Herman, G. S. Higashi, and H. Temkin. Raman analysis of light-emitting porous silicon. *Applied Physics Letters*, 60(17):2086–2088, 1992.

[35] M. N. Islam and S. Kumar. Influence of crystallite size distribution on the micro-Raman analysis of porous Si. *Applied Physics Letters*, 78(6):715–717, 2001.

[36] H. Richter, Z.P. Wang, and L. Ley. The one phonon Raman-spectrum in microcrystalline silicon. *Solid State Communications*, 39(5):625–629, 1981.

[37] Y. Kanemitsu, H. Uto, Y. Masumoto, T. Matsumoto, T. Futagi, and H. Mimura. Microstructure and optical properties of free-standing porous silicon films: Size dependence of absorption spectra in si nanometer-sized crystallites. *Physical Review B*, 48:2827–2830, 1993.

[38] J. Menéndez and M. Cardona. Temperature dependence of the first-order raman scattering by phonons in si, ge, and -sn: Anharmonic effects. *Physical Review B*, 29:2051–2059, 1984.

[39] Z. X. Su, J. Sha, G. W. Pan, J. X. Liu, D. R. Yang, C. Dickinson, and W. Z. Zhou. Temperature-dependent Raman scattering of silicon nanowires. *Journal of Physical Chemistry B*, 110(3):1229–1234, 2006.

[40] H. Hofmeister, F. Huisken, and B. Kohn. Lattice contraction in nanosized silicon particles produced by laser pyrolysis of silane. *European Physical Journal D*, 9(1-4, SI):137–140, 1999.

[41] G. Ledoux, O. Guillois, D. Porterat, C. Reynaud, F. Huisken, B. Kohn, and V. Paillard. Photoluminescence properties of silicon nanocrystals as a function of their size. *Physical Review B*, 62(23):15942–15951, 2000.

[42] D. Q. Yang, J. N. Gillet, M. Meunier, and E. Sacher. Room temperature oxidation kinetics of Si nanoparticles in air, determined by x-ray photoelectron spectroscopy. *Journal of Applied Physics*, 97(2), 2005.

[43] S. Guha, P. Steiner, and W. Lang. Resonant raman scattering and photoluminescence studies of porous silicon membranes. *Journal of Applied Physics*, 79(11):8664–8668, 1996.

[44] F. Agulló-Rueda, J. D. Moreno, E. Montoya, R. Guerrero-Lemus, and J. M. Martinez-Duart. Influence of wavelength on the Raman line shape in porous silicon. *Journal of Applied Physics*, 84(4):2349–2351, 1998.

[45] F. M. Liu, B. Ren, J. H. Wu, J. W. Yan, X. F. Xue, B. W. Mao, and Z. Q. Tian. Enhanced-Raman scattering from silicon nanoparticle substrates. *Chemical Physics Letters*, 382(5-6):502–507, 2003.

[46] Y. H. Xie, F. M. Wilson, W. L. andRoss, J. A. Mucha, E. A. Fitzgerald, J. M. Macaulay, and T. D. Harris. Luminescence and structural study of porous silicon films. *Journal of Applied Physics*, 71(5):2403–2407, 1992.

[47] C. Delerue, G. Allan, and M. Lannoo. Theoretical aspects of the luminescence of porous silicon. *Physical Review B*, 48:11024–11036, 1993.

[48] L. E. Brus, P. F. Szajowski, W. L. Wilson, T. D Harris, S. Schuppler, and P. H. Citrin. Electronic spectroscopy and photophysics of Si nanocrystals: relationship to bulk c-Si and porous Si. *Journal of the American Chemical Society*, 117(10):2915–2922, 1995.

[49] A. G. Cullis, L. T. Canham, and P. D. J. Calcott. The structural and luminescence properties of porous silicon. *Journal of Applied Physics*, 82(3):909–965, 1997.

[50] J. V. Tsybeskov, L. andVandyshev and P. M. Fauchet. Blue emission in porous silicon: Oxygen-related photoluminescence. *Physical Review B*, 49(11):7821–7824, 1994.

[51] O. Bisi, S. Ossicini, and L. Pavesi. Porous silicon: a quantum sponge structure for silicon based optoelectronics. *Surface Science Reports*, 38(1-3):1–126, 2000.

[52] L. T. Canham. Luminescence bands and their proposed origins in highly porous silicon . *Physica Status Solidi B-Basic Research*, 190(1):9–14, 1995.

[53] L. Pavesi and M. Ceschini. Stretched-exponential decay of the luminescence in porous silicon. *Physical Review B*, 48:17625–17628, 1993.

[54] N. Ookubo and S. Sawada. Temperature dependence of photoluminescence in porous silicon and its interpretation using the porous-cluster model. *Physical Review B*, 51:17526–17534, 1995.

[55] P. D. J. Calcott, K. J. Nash, L. T. Canham, M. J. Kane, and D. Brumhead. Identification of radiative transitions in highly porous silicon. *Journal of Physics-Condensed Matter*, 5(7):L91–L98, 1993.

[56] S. P. Depinna and D. J. Dunstan. Frequency-resolved spectroscopy and its application to the analysis of recombination in semiconductors. *Philosophical Magazine B-Physics of Condensed Matter Statistical Mechanics Electronic Optical and Magnetic Properties*, 50(5):579–597, 1984.

[57] M. Dovrat, Y. Goshen, J. Jedrzejewski, I. Balberg, and A. SaAr. Radiative versus nonradiative decay processes in silicon nanocrystals probed by time-resolved photoluminescence spectroscopy. *Physical Review B*, 69(15):155311, 2004.

[58] D. Kovalev, H. Heckler, G. Polisski, and F. Koch. Optical properties of si nanocrystals. *Physica Status Solidi (B)*, 215(2):871–932, 1999.

[59] T. Suemoto, K. Tanaka, and A. Nakajima. Interpretation of the temperature dependence of the luminescence intensity, lifetime, and decay profiles in porous Si. *Physical review B*, 49(16):11005–11009, 1994.

[60] A. L. Efros and M. Rosen. Random telegraph signal in the photoluminescence intensity of a single quantum dot. *Physical review letters*, 78(6):1110–1113, 1997.

[61] D. Kovalev, H. Heckler, B. Averboukh, M. Ben-Chorin, M. Schwartzkopff, and F. Koch. Hole burning spectroscopy of porous silicon. *Physical Review B*, 57(7):3741–3744, 1998.

Chapter 3

Silicon-silica aerogel composites

3.1 Introduction

In this chapter, we consider the incorporation of silicon nanoparticles into an aerogel. Aerogel was first made by Kistler [1] in 1930's. Since then, there have been many practical applications. This is because of the simple and uncomplicated way to synthesis both organic and inorganic compounds into aerogel[2], particularly, silica aerogel.

Silica aerogel is an amorphous material, usually having a high open porosity which has been described as the solid gel network. Typically, the silica aerogel has pores on the scale of about 10 to 50 nm. Physical properties of the aerogel include low refractive index (1.02 to 1.05), low density (typically greater than 90% air by volume), high optical transparency, extremely low thermal conductivity, and a large surface area that accessible to gas [3].

Over the last two decades, interest in silica aerogel has rapidly arisen according to its unique characteristics. Silica aerogel, a nano-porous structure, is potentially an ideal host for nanoparticles such as gold, silver etc. It provides many possible applications in non-linear photonic devices, catalysis, gas sensing, photochemistry etc. [4, 5, 6]. Typically, silica aerogel is prepared from the liquid phase, which gives an opportunity to design shape, volume, the possibility of long path length and a solid pore network structure which could be advantageous for light

interacting with embedded nanoparticles.

In chapters 1 and 2, silicon nanoparticles were introduced and studied as a photosensitiser that can transfer energy to chemical species such as oxygen molecules etc. [7, 8]. Potentially, this offers the possibility of a connection between the optical excitation of silicon nanocomposites and gas diffusion within the silica aerogel pores. Therefore, silica aerogel could be an ideal candidate substrate for nano-silicon particles.

There are already a few studies on the silica aerogel/porous silicon nanocomposites. One of these studies created the composites in pellet form by pressing various mixtures of silica aerogel and porous silicon powder [9] which, of course, the pore structures must be closed up by this method. In this chapter, we attempted to prepare silicon-silica aerogel composites by a more conventional method (the detail is explained in section 3.2) with various types of silicon nanoparticles and concentrations. We will also explore the optical properties and the behaviour of the composite inside the silica aerogels.

3.2 Sample preparation

This section describes the procedure for preparing samples. This includes the descriptions on how to create the silicon nanoparticles in powder form, the process to prepare the silica aerogel, and how the nanoparticles incorporate into the gels.

3.2.1 Silicon powder preparation

Three different types of porous silicon powder were created to introduce into silica aerogel. Firstly, commercial metallurgical grade polycrystalline silicon powder was prepared by Vesta Ceramics, with a typical particle size of approximately 3-11 microns. This was used to create porous silicon particles via the stain etching method [10]. Stain etching is normally used to create porous silicon from silicon powders. In stead of electrochemical reaction in electrochemical etching that was introduced in chapter 1, a chemical oxidant plays a key role in control the reaction of this etching. The porous silicon grains were produced by immersing

the silicon powders in hydrofluoric acid (HF) solutions with other additives, commonly, nitric acid. The final grains contain a bulk silicon core surrounded by a nanoporous silicon shell with freshly hydride-terminated (H-terminated) surfaces (tagged PSi-NPs). The particle size distribution of these PSi-NPs can be specified by controlling the etching time. After this process was finished, the porous powders were collected from the etching solution and dried. In ambient conditions, the porous surfaces will start to oxidise and incorporate a mono-layer of oxygen atoms back-bonded to the hydrogen-terminated (H-terminated) surfaces [11]. However, variation in the temperature and the humidity can create the different types of porous silicon surface.

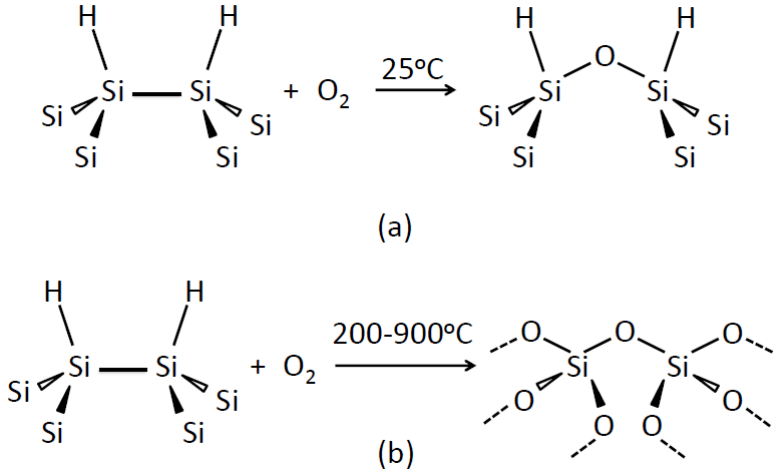

Figure 3.1: Oxidation reactions : (a) at room temperature, (b) at high temperature and the figure adapted from reference no.[11].

At room temperature, oxidation creates an oxide layer which can grow over several months. Nevertheless, some H-terminated surfaces still remain as shown in figure 3.1(a). It will also be shown in section 3.3.3 that there is efficient energy transfer to oxygen, which suggests that the H-terminated surfaces are preserved [7]. These powders are labelled as LH type.

Secondly, via thermal annealing of these PSi-NPs in air at high temperature, the surfaces can be completely oxidised [7] to produce oxide terminated (O-terminated) surfaces. This is demonstrated in figure 3.1(b). These powders are called LO type. Both LH and LO type are dark brown in colour, as presented in figure 3.2 (a).

Finally, silicon nanocrystals (Si-NCs) were produced in a microwave supported

plasma reactor [12]. Their initial average size is approximately 25 nm. This was then followed by stain etching, to achieve the size where visible photoluminescence has been observed [13]. These free standing powders have an average of 5-10 nm. They are then developed into O-terminated surfaces (labelled as SO type) and have a light brown colour, as shown in figure 3.2 (b).

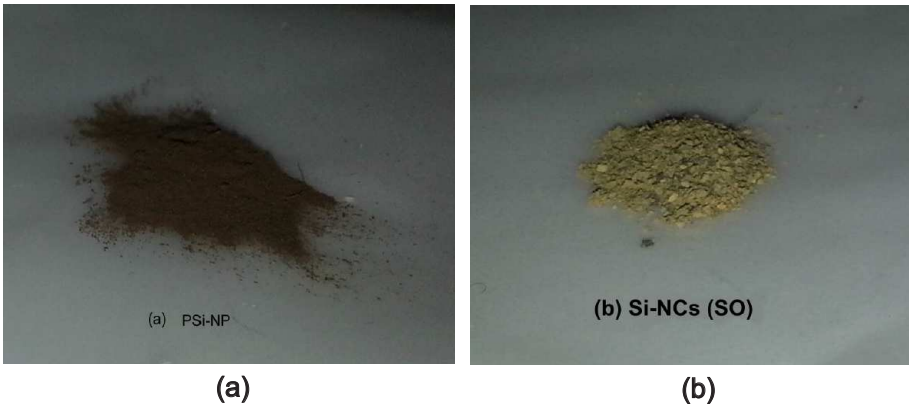

Figure 3.2: Silicon powder : (a) PSi-NPs, (b) Si-NCs.

Figure 3.3 shows three different models of silicon powder before incorporation into aerogels. The silicon grains is etched to obtain the core-shell structure as modelled in figure 3.3 (a); the PSi-NC surface, initially, remains H-terminated. After the thermal treatment, this surface will be oxidised to become O-terminated, as shown in figure 3.3 (b). Finally, predominant O-termination of Si-NCs is illustrated in figure 3.3 (c).

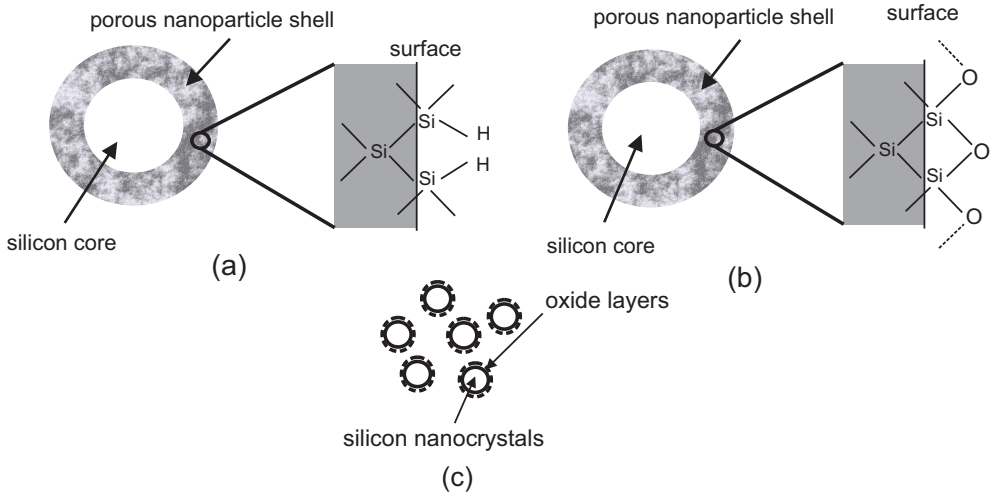

Figure 3.3: Three types of silicon powder models : (a) PSi-NP (LH type), (b) PSi-NP (LO type) and (c) Si-NCs (SO type).

3.2.2 Formation of silicon nanoparticles in silica aerogels

Conventional silica aerogel is prepared in two stages. The first step is to form a "sol gel", which is used to obtain the desired gel structure, and to introduce the materials inside the gel. This is followed by the supercritical drying process with CO_2, which prevents capillary forces that could damage or collapse the glass network [5].

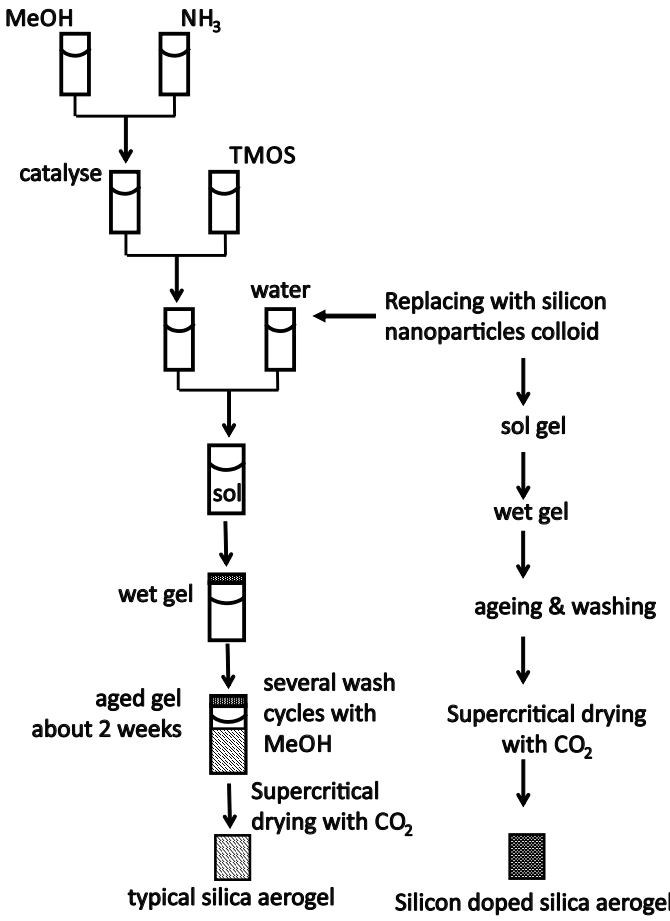

Figure 3.4: Schematic diagram of silica aerogel procedure.

Figure 3.4 shows a step by step schematic diagram of the preparation process. First of all, ammonia (NH_3) is added into the methanol (MeOH) to act as a catalyst of rigid gel setting. The sol gel is then made from a mixture of tetramethyl orthosilicate (TMOS), water and the catalyst MeOH to homogenise and form a wet gel. This is followed by an aging step, which takes about 2 weeks[5]. In this step, the gel was washed several times in MeOH to diffuse water, and create a hydrophilic surface. After that, MeOH is exchanged with the supercritical CO_2 and air to create the silica aerogel in the supercritical drying process.

The three varieties of silicon nanoparticles (PSi-NPs (LH and LO types) and Si-NCs) that introduced in Sec.3.2.1 were incorporated into the silica aerogel in form of colloidal suspension of MeOH. The silicon nanoparticle-aerogel composites were formed by replacing the water with these colloids in the wet gel formation stage. By varying concentrations of silicon nanoparticle dopants from, approximately, 0.0053 to 0.34 mg/ml (increased by a factor of 2 in each step), sets of silicon-silica aerogel composite samples have been created with dimensions of approximately $10 \times 10 \times 20$ mm, as shown in figure 3.5

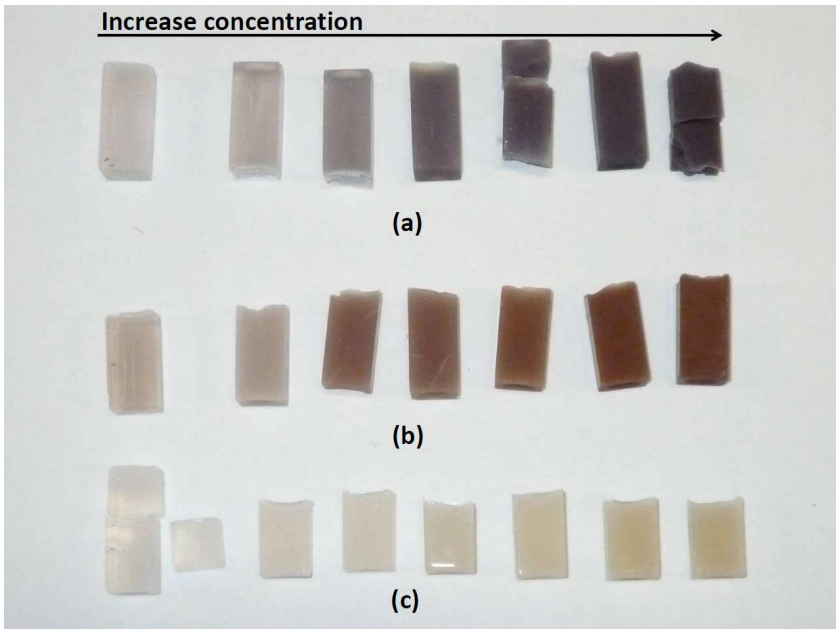

Figure 3.5: Silicon nanoparticle-silica aerogel composites with different concentrations with : (a) LH , (B) LO and (C) SO silicon powder dopants.

Figure 3.5 (a) shows three sets of aerogels containing particles of LH type. Starting with a transparent block (coloured in the light grey) through a dark grey till completely black opaque indicate oxidised porous structure, which happen during the preparation. In contrast with LH silicon nanoparticle-aerogel composites, aerogels that contain LO particles are brown, as shown in figure 3.5 (b). This implies a broad absorption spectrum in the visible range. Consequently, this demonstrates the presence of porous silicon in the final product. Meanwhile, in figure 3.5 (c), aerogels with SO powder are pale yellow to brown colour (depending on its concentrations). This again proves the existence of silicon nanocrystals in the aerogel matrix.

3.3 Experimental Results

This section contains experimental results on the morphology and optical properties of silicon aerogel composites. Physical and optical measurements are used, in order to obtain a full understanding of the presence of PSi-NP and Si-NC in the aerogel matrix, the oxidation states in aerogel composites and the reaction of adsorbed molecular oxygen (O_2) with the composites.

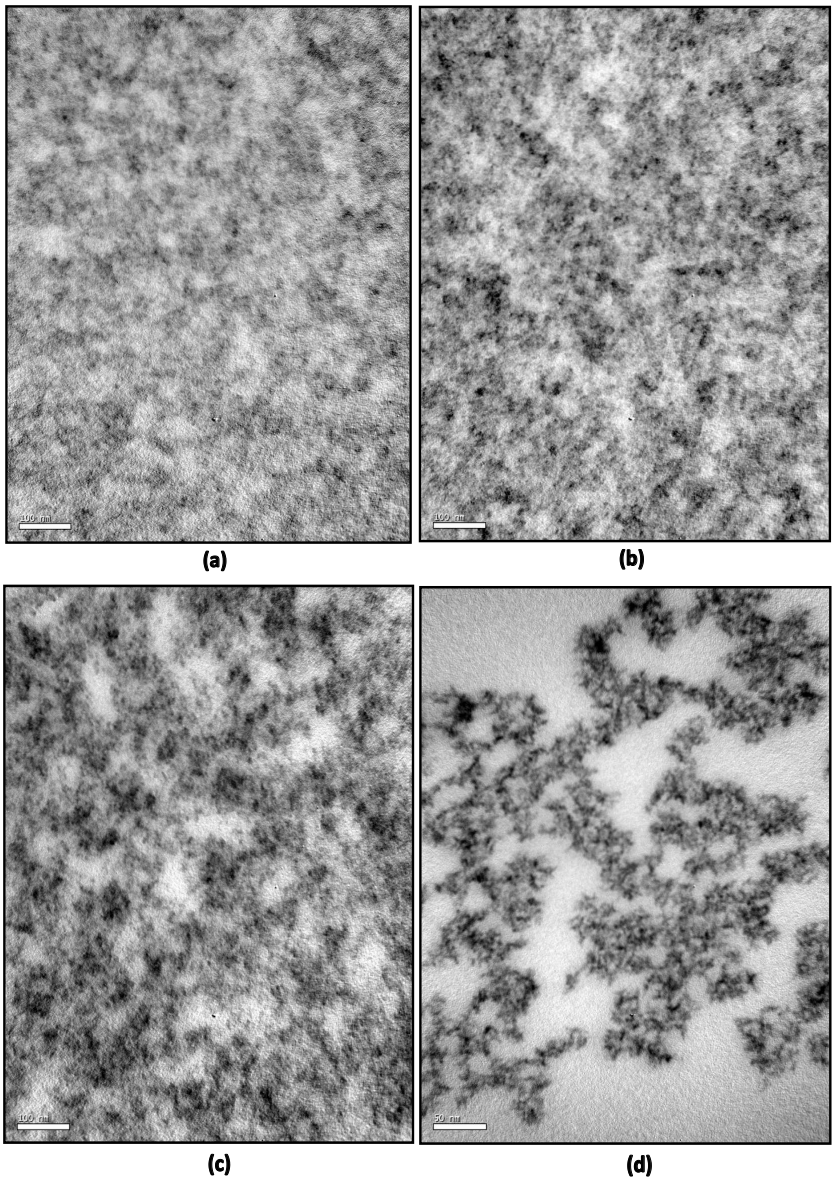

Figure 3.6: Top view images of various nanosilicon doped silica aerogels : (a) LH , (b) LO, (c) SO aerogel composites at 0.085 mg/ml concentration, approximately, (scale bars are 100 nm) and (d) SO aerogel composite at 0.021 mg/ml (scale bar is 50 nm).

3.3.1 Microscopic images

Transmission electron microscopy (TEM,JEOL JEM1200EXII) was used as a tool to quantify the morphology and pore size of the samples. TEM images of the surfaces of the doped aerogels are shown in figure 3.6.

The nanosilicon particles and silica grains could not be distinguished by image contrast. For the LH aerogel, the image does not obviously show the pore structure. This is also the case with the LO sample for large porous grains, which were introduced into gels. On the other hand, the TEM image of SO composite clearly shows porous features in the range of 10-30 nm, as shown in figure 3.6 (c). The low concentration SO gel (present in figure 3.6(d)), in particular, exhibits a sponge-like network porous structure. These results could indicate the size and the doping concentration of the silicon nanograins.

3.3.2 Photoluminescence

Photoluminescence (PL) measurements were studied at room temperature in vacuum. Samples were excited by unfocused continuous wave 325-nm with power densities of 10.61 mW/cm^2. The samples were loaded into a cryostat, which also can cool the samples down to liquid nitrogen temperatures (approximately below 80K). In order to investigate the energy transfer effect, an oxygen reservoir was connected with the cryostat to supply O_2 into the sample space to detect the PL quenching by adsorbed O_2. The PL spectra were detected using a low resolution single-grating spectrometer (Spectra Pro275 Si) and CCD detector.

In figure 3.7, all spectra were normalized to the peak height to emphasize the shape of the PL bands. The PL spectra of PSi-NP (LH) and Si-NC were measured before incorporated into the aerogels; the PL spectrum of the LH grains was dominated by the silicon nanoparticles inside the porous shell. This spectrum band covers in the visible range from 1.35 - 2.1 eV, approximately, corresponding to the size distribution of nanoparticles inside the porous shell. On the other hand, the PL band of Si-NC (SO) centers at 1.8 eV with a range from 1.5 - 2.1 eV, which is slightly higher energy and narrower width, indicating smaller size distribution than the porous grain powder.

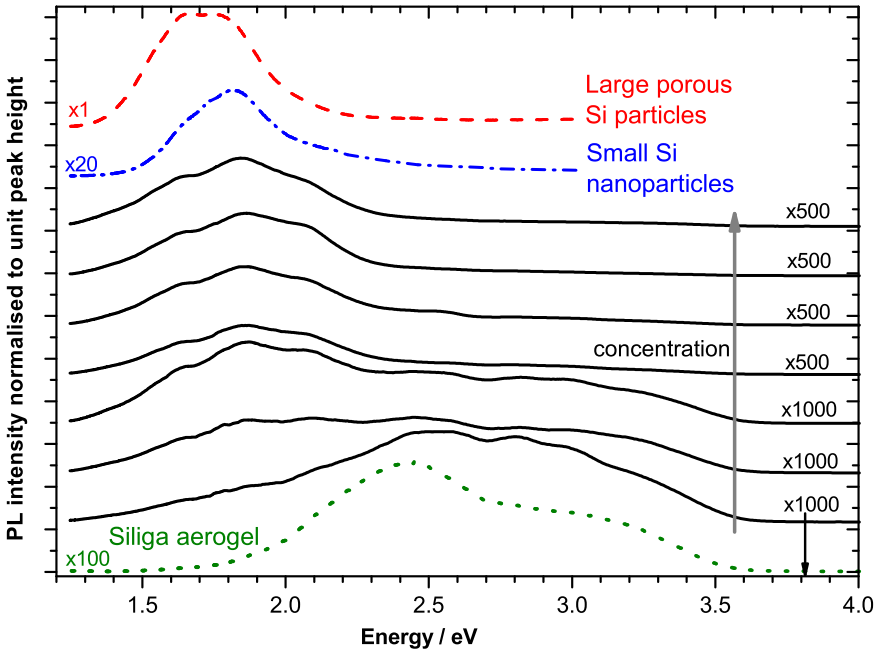

Figure 3.7: Photoluminescence spectra of porous silicon and silicon nanoparticles before and after incorporation in silica aerogel : PL spectrum of porous silicon LH (red dashed line at the top), PL spectrum of silicon nanoparticle SO (blue dashed-dotted line at the second top) and PL spectrum of silica aerogel (green dotted line at the bottom). Black lines represent the PL spectra of LH porous silicon doped aerogel series with various concentrations, initially, increasing from 0.0053 to 0.34 mg/ml by the factors of 2. These spectra show the lowest to the highest concentrations in upward direction as shown by the grey arrow. The black downward arrow shows the excitation energy at 3.81 eV (325 nm). Spectra are scaled by the indicated multiplication factors for better comparison.

As presented in figure 3.7, the PL spectra of the composites from the lowest to the highest concentration (upward direction, as shown by a grey arrow) starting from a broad, high energy emission to become narrower and shift to a lower energy emission. This can be interpreted as the PL spectrum of the lowest concentration mainly originating from silica aerogel, itself. The bottom PL spectrum (green dotted line), which is typical PL spectrum of silica aerogels [14]. However, with increasing concentrations, the PL spectra become more dominated by silicon nanoparticles as compared with the powder form PL spectra (red and blue upper lines). Figure 3.7 shows the results, which obtained from LH aerogel composites. Basically, the same sequence of PL spectra is obtained for the LO and SO aerogel composites.

3.3.3 Energy transfer to oxygen

Generally, the silicon nanoparticle can be used as a donor[1] to transfer energy to an acceptor[2] like O_2, which was explained in more detail in chapter 1. To observe the interaction of silicon nanoparticle with O_2 after incorporation in the aerogels, the investigation sensitivity with O_2 was measured by excitation at 3.81 eV (325 nm). Unfocussed excitation beam has been used at 10.61 mW/cm^2 (the same as in section 3.3.2).

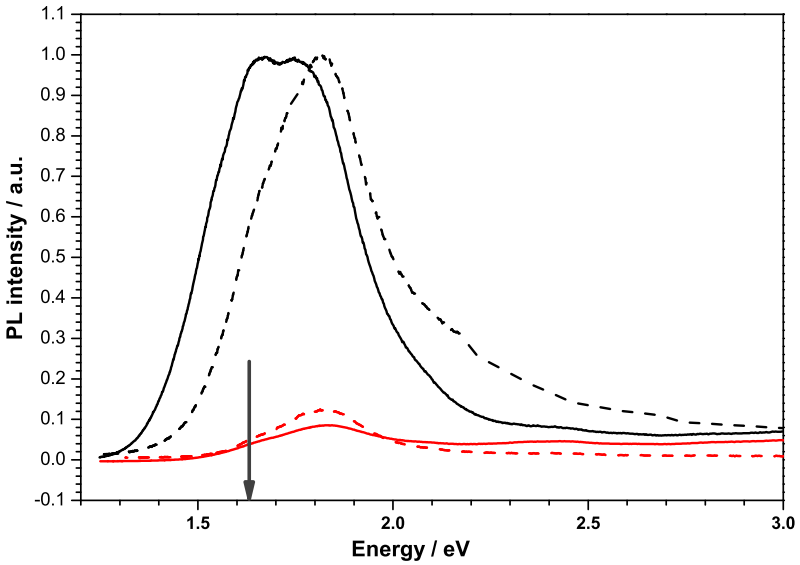

Figure 3.8: Photoluminescence spectra of PSi-NP and Si-NC samples in vacuum and in the presence of O_2 at liquid nitrogen temperature before embedded into the gel. Black lines show the PL spectra in vacuum, which were quenched after adsorbed O_2 (red lines) via the energy transfer process, solid lines and dashed lines represent large nanoporous silicon and small silicon particles respectively. The arrow indicates the energy of triplet-singlet ($^3\Sigma$-$^1\Sigma$) transitions of O_2 (at 1.63 eV). All spectra are normalised to unit peak height of the spectra measured before energy transfer occurrence.

PL spectra of LH and SO particles in powder form in vacuum are illustrated in figure 3.8 (black lines); when O_2 was present the spectra dropped down, as shown in the red lines. Typically, these show the quenching of PL spectra due to the energy transfer process as discussed earlier in chapter 1. However, there is no

[1]Donor in this term means the energy donation rather than the electron donation.
[2]Acceptor in this term means the energy acceptance rather than the electron acceptance.

evidence of any quenching in all of the aerogel composites. This means that the incorporation of the silicon nanoparticle into the aerogel has changed the surface state of this nanoparticle. We tried to turn this surface into the active state again by refreshing aerogel in hydrofluoric acid (HF) vapour.

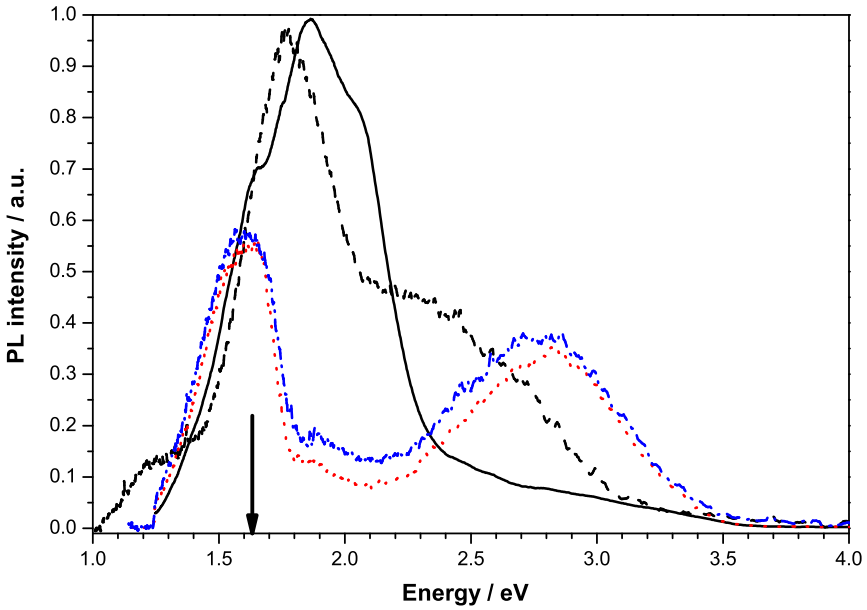

Figure 3.9: Photoluminescence spectra of LO aerogel at 0.17 mg/ml concentration in vacuum and in O_2 at liquid nitrogen temperature comparing between before and after refreshing. In vacuum, PL spectrum of the original LO sample is presented by a black solid line, after refreshing is represented by the black dash line. In O_2 ambient, the PL spectrum quenched down to the red dotted line. Finally, the blue dash-dot line presents the spectrum when O_2 was removed. The arrow shows a typical energy where energy transfer process takes place. In vacuum, the spectra were normalised to unit peak height. The PL spectra of LO aerogel in the presence of O_2 were normalised with their PL spectrum in vacuum in order to compare degree of changing.

The LO aerogel composite was refreshed in HF vapour to eliminate the oxide layer which probably occurred during the preparation stage. However after refreshing, the PL spectrum of the LO gel broadens and covers the range of approximately 1.5 - 3.1 eV, as shown in figure 3.9 with the black dotted line. This is implied that the change of the PL spectrum is a consequence of the combination of defects, chemical impurities and surface states which affects by HF vapor. When oxygen is admitted into the refreshed LO gel, the PL spectrum changes to the red dotted line. Nevertheless, this is not clear evidence for the appearance of

energy transfer, because no recovery has been observed (blue dash-dotted line). Therefore, the incorporation of silicon nanoparticles inside aerogel reduces the efficiency of the energy transfer process from them to oxygen molecules. This can be understood if, somehow in the preparation procedure, the active surface state (hydrogen-terminated surface) has been oxidised. According to this assumption, the spatial distance between the confined exciton of silicon nanoparticles and oxygen molecules is increased and, hence, no transfer energy was observed.

3.3.4 Raman scattering

As previously detailed in section 2.5, disorder and size of crystallites determine the shapes of Raman lines from microcrystalline semiconductors [15]. In bulk crystalline Si (c-Si), the first order of the Γ-point phonon mode is about 521 cm^{-1} in a symmetric spectrum shape with a peak width of 3 cm^{-1} [16]. According to quantum confinement and the relaxation of momentum selection rules in nano-particles, a shift to a lower energy and an asymmetric broadening of the Raman spectrum are produced. These can be used to estimate the size distribution of the nano-particles [16, 17, 18, 19, 20].

The Raman scattering experiment was measured in a macroscopic sampling mode in the back scattering geometry using 532 nm excitation at 74 mW/cm^2 (to avoid heating effects, low power excitation was used). A triple grating spectrometer (Jobin Yvon) collected the scattering light. The first stage of this is a pre-monochromator (DHR 320) which consists of two diffraction gratings forming a bandpass filter. Incoming scattering light was focused on the first grating which disperses the light and passed through an adjustable slit to reject the elastic scattering light. Finally, in the monochromator (THR 1000), the Raman-scattered light was dispersed again by a final grating which, in this case, is a 300 groove/mm grating and was recorded on a liquid nitrogen-cooled CCD. This final grating can be changed between a 300 groove/mm grating for low resolution to a 1800 groove/mm for high resolution measurements.

The Raman spectra of silica aerogels and a representative selection of doped aerogel samples are shown in figure 3.10. The top black line represents the Raman spectrum of silica aerogel with peaks at 485 and 620 cm^{-1} which are called, respectively, D_1 and D_2 defect lines of silica aerogel. Their origin has been widely

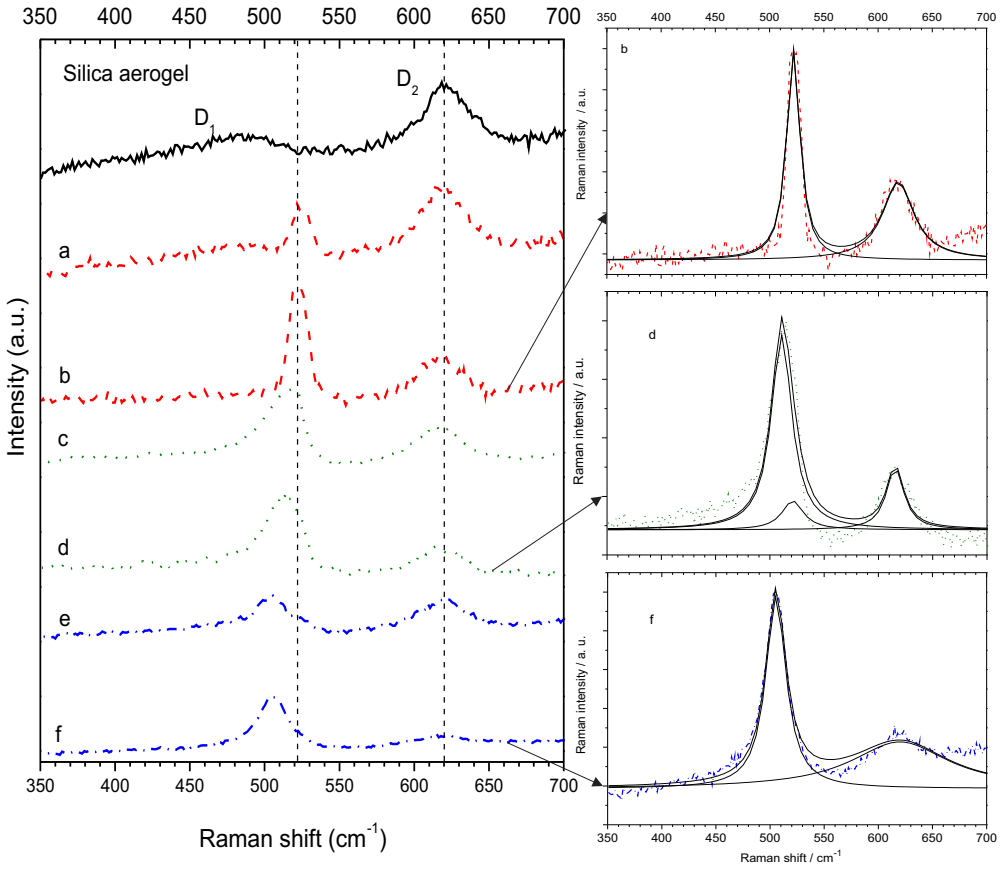

Figure 3.10: Raman spectra of selected composite samples. On left side : Raman spectra of silica aerogel (black solid line) and doped aerogels. LH are represented by red dash lines with (a) and (b) are 0.021 and 0.084 mg/ml concentrations, respectively. LO are represented by green dot lines with (c) and (d) are different concentrations as LH. SO within aerogels are shown by blue dash-dot lines LO aerogel with (e) and (f) are different concentrations as LH. The vertical dash lines indicate the Raman shift of the bulk silicon (left) and the D_2 silica defect band (right). Right side : shows fitting of the Raman spectra of the different aerogel composites at 0.084 mg/ml concentration.

discussed in many articles [21, 22]. As mentioned before, the first order Raman shift of bulk silicon is 521 cm^{-1}. Comparing with the LH aerogels Raman lines, a Lorentzian line shape fitting presents center at 522 cm^{-1}, full width half maximum (FWHM) 12 - 15 cm^{-1} as shown on right side of figure 3.10 (b). This gives an important indication that the Raman spectra of LH composites are mainly dominated by the solid silicon core of PSi-NPs silicon particles. Therefore, there are few porous shell have left after incorporating into the aerogel (as demonstrated in section 3.3.2 by the presence of silicon nanoparticles in the PL spectra of the LH aerogels)

On the contrary, figure 3.10 (c) and (d) clearly show asymmetric Raman spectra. The Raman peaks shift to a lower frequency, with a peak at 515.5 cm^{-1}, FWHM 28 cm^{-1} for (d) spectrum. Regarding these two parameters and a phonon confinement model in the literature [15, 16], the diameter of this particle could be then estimated to be around 4 nm. However, these LO particles have originally a core-shell structure, hence, taking account of the core bulk silicon phonon frequency in the fitting gives the second peak (related to the shell structures) at 510 cm^{-1} and FWHM 23 cm^{-1} as presented in (d) at the right side of figure 3.10. This implies an average diameter of 2.7 to 3.3 nm. This Raman band is obviously dominated by the porous shell of nano-silicon.

Ultimately, the SO nanocrystals are solid and have an approximately spherical shape due to the preparation process that was described in section 3.2.1. According to this assumption, single band fitting has been used to fit the silicon nanoparticle band (the same case as LH particles for which mainly the core structure remains), as demonstrated in the right side of figure 3.10 (f), the fitting peak is at 505.5 cm^{-1} with FWHM 23 cm^{-1} which could be interpreted as a mean diameter of 2.3 to 3.3 nm referring to the same model [15, 16].

According to figure 3.5, as increasing the concentration of Si nanoparticles ; the appearance of aerogel composites changes from highly transmitting to become more opaque. The penetration depth for the excitation light and the total scattering volume were reduced drastically as the concentrations increased. Because the well-defined aerogel Raman D_2 band (as illustrated in figure 3.10 at 620 cm^{-1}) arises from the same scattering volume as the silicon Raman band, an ideal method to examine the concentration-dependence of the Raman scattering band, possibly, is given by the ratio between the integrated intensity of the silicon Raman band and the aerogel D_2 band. This ratio gives a prospective quantitative proportion to the silicon nanoparticles concentration on the assumption that the structure of the silica aerogel should not be modified by the presence of the embedded silicon particles. However, it has been reported that the interpretation of the ratio of these defect lines (D_1, D_2) is indicative of amount of water in the silica aerogel network [22]. But in the present case, there is no expectation of any dramatic changes in the Si-O network.

Figure 3.11 shows the ratio of the silicon Raman band and the silica aerogel D_2 band as a function of a mass density of the silicon particles introduced during

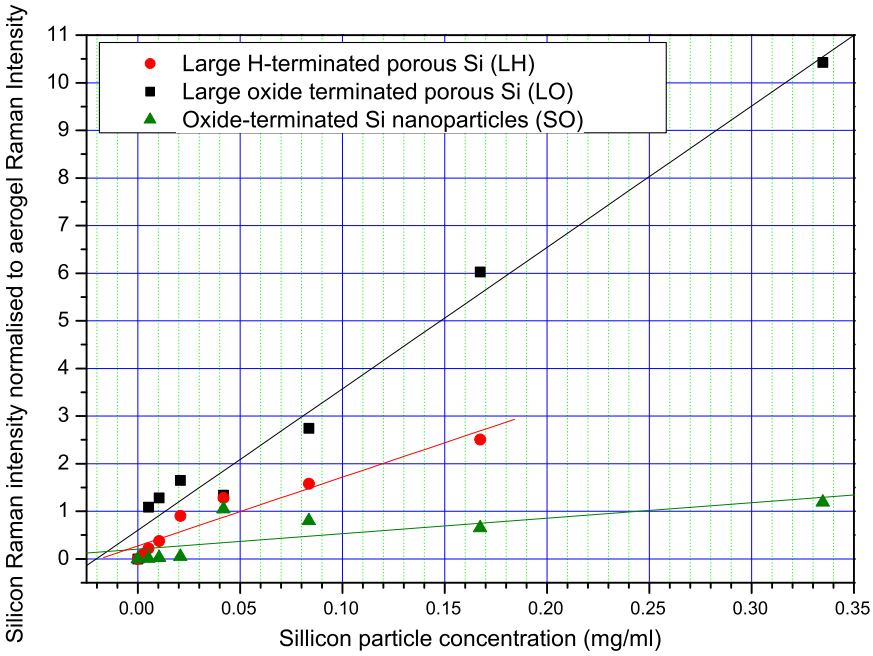

Figure 3.11: The ratio of the silicon to silica Raman intensities as a function of nano-silicon dopants concentration for LH, LO and SO particle (black squares, red circles and green triangles, respectively. Solid lines are linear least-squares fits for each data set. These data sets were examined under the 532 nm excitation wavelength.

the preparation process, for each type of dopants. Obviously, the gradient of the linear fits depends on the type of incorporated materials. First, in the SO nanoparticle case, it is clearly shown that the proportion between silicon Raman band and aerogel band seems to vanish away during the preparation procedure, according to their mean size (5 - 10 nm). This is much less than the aerogel pore size (typically, 10 - 50 nm). Therefore, there are few enduring SO particles in the SO doped gel. This accounts both for the weak degree of colouration, as shown in figure 3.5 (c) and the low rate of increase of the Raman band with concentration as presented in figure 3.11 (green triangular line).

Secondly, the colouration of the LH doped aerogel, apparently, indicates the ratio of the silicon nanoparticle in the composites (as shown in figure 3.5 (b)) which agrees with the ratio of the LH Raman band in figure 3.11 (red circle line). The Raman strength of the LH composite is higher than the SO particles due to the larger diameter of the embedded particles. Finally, the LO particles (black square line) have the highest rate of increase of the Raman band with concen-

tration. Comparing between LO and LH particles, which initially have the same average diameters, the Raman strength of the LO particles is stronger than the LH particles by factor of 2, approximately. This is qualitatively consistent with the previous conclusion that the porous shell of the LH particles were oxidised, causing a loss of scattering cross-section of the silicon phonon mode.

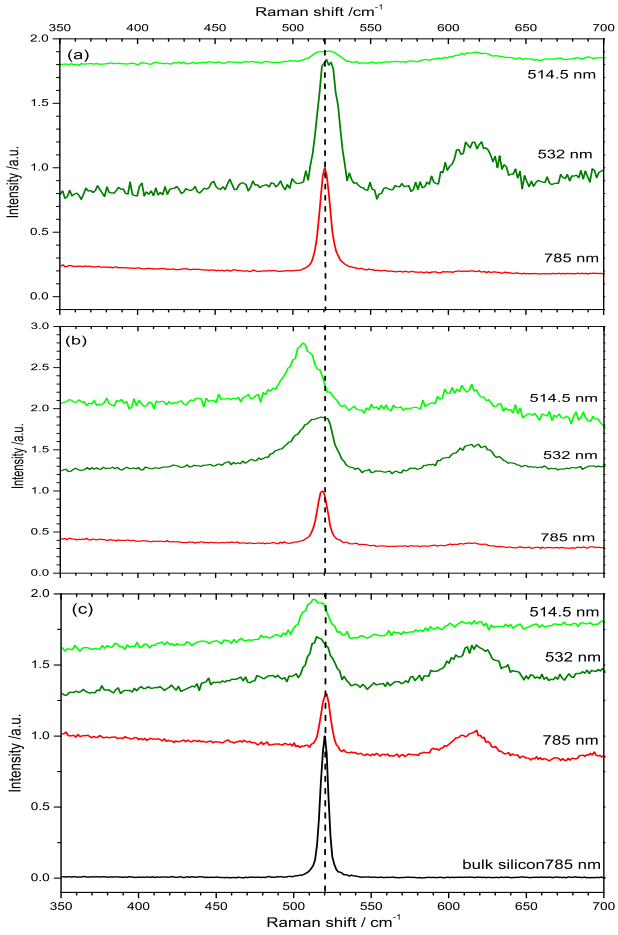

Figure 3.12: Comparison of Raman spectra on the selective composite samples with the various excitation wavelengths 514.5 nm, 532 nm and 785 nm. Top (a) is the Raman spectra of the LH aerogel. Middle (b) shows the Raman spectra of the LO aerogel. Bottom (c) is the Raman spectra of SO aerogel and the crystalline silicon (black line). The vertical dash lines indicate the Raman shift of the bulk silicon (521 cm^{-1}). All Raman spectra were normalised to their unit peak height.

In comparison, Raman scattering measurements were taken at different excitation wavelength with the similar laser powers to those at wavelength 532 nm. At laser wavelength 514.5 nm, the instrument set up is the same as 532 nm. However,

at 785 nm laser, Raman spectra were measured by a Renishaw inVia Raman Microscope.

Figure 3.12 shows the comparison between the Raman shift of 514.5, 532 and 785 nm excitation wavelengths. The spectra of LH aerogel show peaks at the same position as the bulk crystalline silicon and even the spectrum excited by 514.5 nm laser shows a broad phonon band and extremely weak signal (less than 5 counts/m). On the other hand, both Raman spectra excited by 532 and 785 nm show sharp symmetric peaks at 522 cm^{-1} and 520.6 cm^{-1} with widths of 14.7 and 7.4 cm^{-1}, respectively as shown in table 3.1. These confirm our assumption that the PSi-NP LH type retains only the crystalline-core structure. Also the 620 cm^{-1} silica aerogel band was detected but the spectra are not as strong as the one which measured at 532 nm. However, the aerogel band was shown more clearly at the lower concentrations of the LH aerogel composites which are not presented in this figure.

Following the Raman spectra of the LO aerogel, as presented in figure 3.12 (b), we observed broad phonon bands with asymmetric lines shape. However, with increasing excitation wavelength, the phonon band becomes narrower in width and closer to the bulk silicon peak. Especially, the spectra of 785 nm exhibits a sharp symmetric line shape and slight shift to lower frequency. By fitting with a Lorentzian line shape, the centre of this Raman peak is 518.6 cm^{-1} with the FWHM of 7.7 cm^{-1}. Nevertheless, considering the core shell structure of the PSi-NP, fitting gives the peak at 517.8 cm^{-1} and FHWM 7.2 cm^{-1} as shown in table 3.1. This can be explained as the effect of resonant Raman scattering (RRS) process [23]. As demonstrated in figure 3.7, the PL spectra of LO composites are broad as determined by the various porous shell sizes. When the excitation laser matches the electron transition energy of a certain size of porous shell, the observed Raman spectrum is dominated by this grain size and enhances the signal. On the other hand, when the excitation wavelength is far from any electron transition energy of the porous shell, the Raman band will be excited without resonance and enhancement. The shorter wavelengths are more sensitive to smaller nanocrystals [23, 24, 25] therefore the Raman spectra from 514.5 and 532 nm excitations demonstrate red shifts and broaden spectra. On the contrary, the 785 nm laser shows the Raman feature of the large porous shell or even the core structure of the LO composite. This explanation also corresponds with Raman spectra of the LH composites which are mainly dominated by the core

structure.

Table 3.1: A Lorentzian fitting of Raman frequency and FWHM at various excitation wavelengths at the main silicon Raman peak

Excitation λ	**LH aerogel**		**LO aerogel**		**SO aerogel**	
(nm)	ω (cm^{-1})	FWHM (cm^{-1})	ω (cm^{-1})	FWHM (cm^{-1})	ω (cm^{-1})	FWHM (cm^{-1})
514.5	520.6	21.5	505.6	21.4	513.4	18.8
532	522.0	14.7	510.0	23.0	516.6	18.8
785	520.6	7.4	517.8	7.2	520.6	7.0

Finally, the Raman spectra of the SO composites present the same trend as the Raman spectra of the LO composites as shown in figure 3.12 (c). The spectra of LH, LO and SO aerogels, excited by 785 nm, present only a narrow and symmetric line shape. This implies that the laser source is far from the resonant range of the sample sizes and cause the same Raman feature of the spectra. Although 514.5 nm excitation can detect the asymmetric and broad silicon Raman band, it is less sensitive to the silica aerogel D_2 band. So the 532 nm laser is an appropriate wavelength for our Raman measurement.

Figure 3.13 shows the ratio of the silicon Raman band and the silica aerogel D_2 band as a function of a mass density of silicon particles introduced during preparation process, for each type of dopants and using the 785 nm laser. This confirms that the 785 nm laser is not a suitable wavelength to analyse the aerogel composites.

3.3.5 Fourier transform infrared transmission

Fourier transform infrared (FTIR) spectroscopy is a technique to measure an infrared spectrum of absorption (transmission) of sample in either solid, liquid or gas phase. This method is used to characterize a molecular structure on surfaces. Also it can be used to confirm the identity and the quantity of substances [11].

The FTIR transmission measurements were made using a Perkin Elmer Frontier FTIR. A diamond attenuated total reflection (ATR) stage is mounted on FTIR

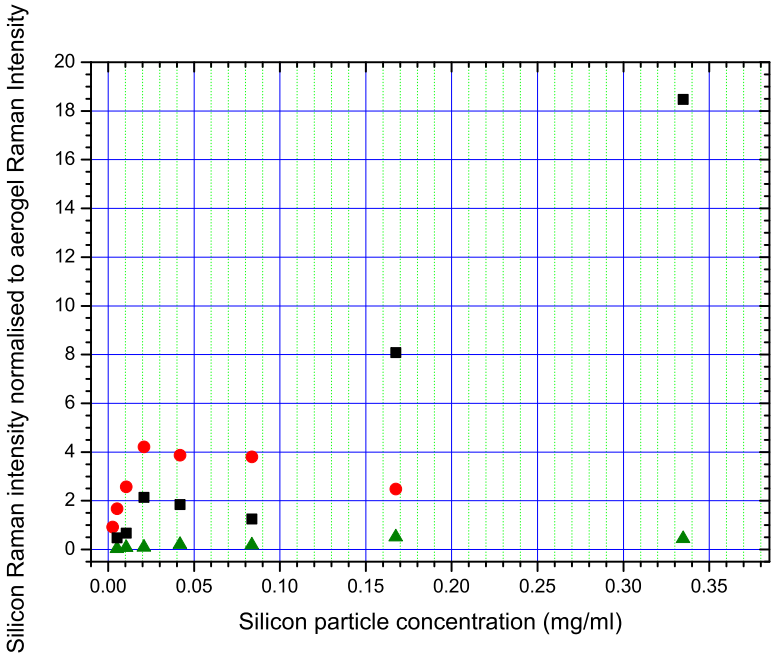

Figure 3.13: The ratio of the silicon to silica Raman intensities as a function of nano-silicon dopants concentration for LH, LO and SO particle (red circles, black squares and green triangles, respectively. These data sets were examined under the 785 nm excitation wavelength.

spectrometer. The sample must be in direct contact with the diamond ATR head. However, due to the fragility of the aerogel, the aerogel sample was fixed with the ATR stage by using only a modest mounting pressure. Therefore, the comparison of the relative strength of a result is not reliable. In terms of the particle concentration measurement, ATR-FTIR is not the best way to provide this answer. Table 3.2 shows typical infrared band frequencies of porous silicon.

However, ATR-FTIR provides a sensitive identification of surface chemical bonding as shown in figure 3.14. The top spectrum was obtained from the conventional electrochemically etched porous silicon. In table 2.4, the Si-H vibrational mode is identified by the dashed lines that corresponding with 2,00-2,200 cm^{-1}, approximately. These modes are shown even if the porous silicon sample was left for several months and rather oxidised. The free Si-NCs (SO) also have the Si-H modes even though these are weaker than the typical porous silicon, as illustrated in the second spectrum. The green spectrum represents the IR absorption after SO was incorporated into the gels. This spectrum has a similar weak Si-H modes, likewise the free SO. This implies that Si-NCs (SO), before and after preparation,

Table 3.2: Common infrared bands associated with porous silicon [11]

Frequency (cm^{-1})	**Species**	**Mode**
2965	Si-CH_3	antisymmetric stretching C-H
2898	Si-CH_3	symmetric stretching C-H
2140	Si-H_3	stretching Si-H
2108	Si-H_2	stretching Si-H
2087	Si-H_1	stretching Si-H
1150-1240	Si-O-Si	symmetric stretching Si-O-Si
980-1050	Si-O-Si	antisymmetric stretching Si-O-Si
610	Si-Si	stretching Si-Si

are mostly oxidised. However, the FTIR spectrum of PSi-NPs (LH) does not show any sign of these bands (the blue spectrum) even in the samples that contain high concentration of PS-NPs. On the other hand, the spectrum is dominated by the IR absorption of silica aerogel rather than the silicon nanoparticles as compared with the bottom spectrum in figure 3.14. Si-O-Si and Si-CH_3 vibration modes of the silica aerogel are presented in table 3.3. The silica aerogel spectrum (at the bottom of figure 3.14) shows the expected Si-O-Si modes with two weak Si-CH_3 modes (indicated by two arrows). The strength of the Si-CH_3 bands indicate whether the aerogel surface is hydrophilic or hydrophobic, therefore these weak modes confirm that our silica aerogels are hydrophilic [26].

Table 3.3: A selection of vibration frequencies in FTIR spectra of synthesized silica aerogel [26]

Frequency (cm^{-1})	**Species**	**Mode**
2969	Si-CH_3	symmetric stretching C-H
2885	Si-CH_3	antisymmetric stretching C-H
$\sim$ 1200	Si-O-Si	antisymmetric stretching Si-O-Si
1095	Si-O-Si	antisymmetric stretching Si-O-Si
799	Si-O-Si	symmetric stretching Si-O

The FTIR of LO aerogel shows no signal of Si-H modes and the spectrum (this is not show in figure 3.14) is similar to those silica aerogels. This corresponds to the previous experiments demonstrating the oxidisation of our aerogels.

3.4 Conclusion

In summary, silicon nanoparticles and macroscopic porous silicon grains are introduced into silica aerogel by conventional aerogel synthesis. For hydride-terminated surfaces, substantial oxidation of the porous silicon occurs during the preparation process. This is severe enough to remove a major part of the porous silicon shell structure. Hence a solid crystalline silicon core is left inside the composites. Various experimental results also provide strong evidence for this conclusion. On the other hand, oxide-terminated porous silicon grains retain their porous structure. However, they are not able to transfer energy to oxygen molecules meaning that these aerogel composites can not be used as hosts in the energy transfer process.

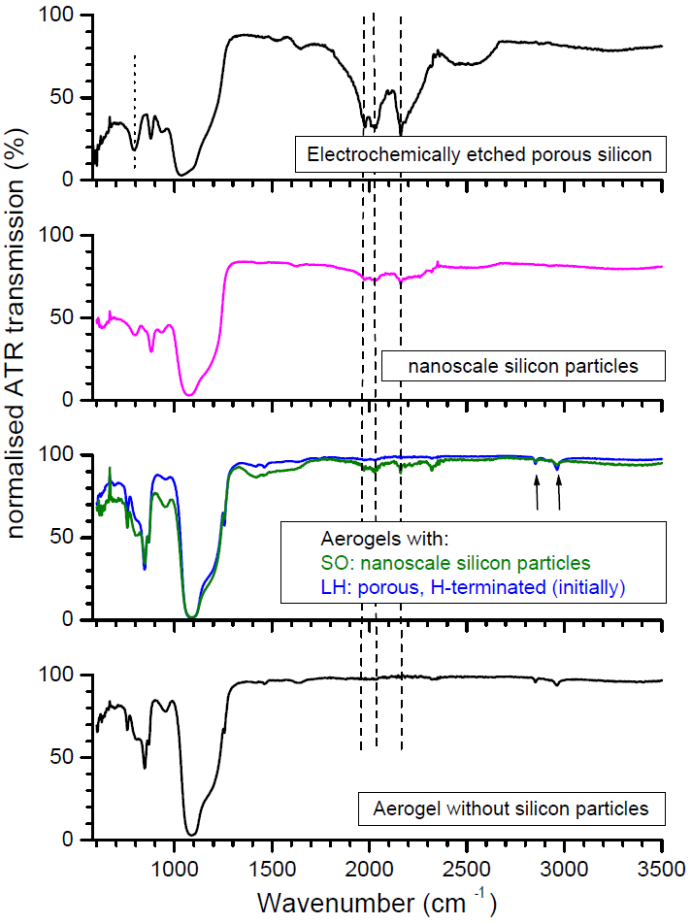

Figure 3.14: Fourier transform infrared transmission spectra in the attenuated total reflection configuration. Top is a spectrum of electrochemically etched porous silicon. The second is a free SO Si-NC spectrum. Thirdly, spectra of aerogels containing SO and LO are presented in green and blue lines, respectively. Bottom displays a spectrum of pure silica aerogel. All spectra are corrected baselines and normalised to 3% transmission at approximately, 1,100 cm^{-1} which is the Si-O-Si absorption band. The vertical dashed lines indicate the Si-H modes and the dotted line on the top shows the 790 cm^{-1} band which corresponds to substantially oxidised porous silicon [11]. The arrows indicate the peaks that present in all type of the aerogels. These peaks relate to the CH_3 species. These results were obtained by Dr.Daniel Wolverson.

References

[1] S. S. Kistler. Coherent expanded-aerogels. *The Journal of Physical Chemistry*, 36(1):52–64, 1931.

[2] G.M. Pajonk. Aerogel catalysts. *Applied Catalysis*, 72(2):217 – 266, 1991.

[3] A. Soleimani Dorcheh and M. H. Abbasi. Silica aerogel; synthesis, properties and characterization. *Journal of Materials Processing Technology*, 199(1-3):10–26, 2008.

[4] N. Husing and U. Schubert. Aerogels airy materials: Chemistry, structure, and properties. *Angewandte Chemie-International Edition*, 37(1-2):23–45, 1998.

[5] M. D. W. Grogan, M. D. Rollings, L. M. Xiao, W. J. Wadsworth, R. England, S. A. Maier, and T. A. Birks. Plasmonic Aerogel Doped with Gold Nanoparticles. In *2010 Conference on Lasers and Electro-Optics (CLEO) and Quantum Electronics and Laser Science Conference (QELS)*. IEEE, 2010.

[6] T. A. Birks, M. D. W. Grogan, L. M. Xiao, M. D. Rollings, R. England, and W. J. Wadsworth. Silica Aerogel in Optical Fibre Devices. In *2010 12th International Conference on Transparent Optical Networks (ICTON)*. IEEE, 2011.

[7] D. Kovalev and M. Fujii. Silicon nanocrystals: Photosensitizers for oxygen molecules. *Advanced Materials*, 17(21):2531–2544, 2005.

[8] B. Goller, S. Polisski, and D. Kovalev. Spin-flip excitation of molecules mediated by photoexcited silicon nanocrystals. *Physical Review B*, 75(7), 2007.

[9] A. Yu Karlash, Yu E. Zakharko, V. A. Skryshevsky, A. I. Tsiganova, and G. V. Kuznetsov. Photoluminescence properties of silica aerogel/porous silicon nanocomposites. *Journal of Physics D-Applied Physics*, 43(33), 2010.

[10] S. Limaye, S. Subramanian, B. Goller, J. Diener, and D. Kovalev. Scaleable synthesis route for silicon nanocrystal assemblies. *Physica Status Solidi A-Applications and Materials Science*, 204(5):1297 – 1301, 2007.

[11] M. J. Sailor. *Porous silicon in practice : preparation, characterization and applications*. Wiley-VCH, Weinheim, 2012.

[12] J. Knipping, H. Wiggers, B. Rellinghaus, P. Roth, D. Konjhodzic, and C. Meier. Synthesis of high purity silicon nanoparticles in a low pressure microwave reactor. *Journal of Nanoscience and Nanotechnology*, 4(8), 2004.

[13] B. Goller, S. Polisski, H. Wiggers, and D. Kovalev. Freestanding spherical silicon nanocrystals: A model system for studying confined excitons. *Applied Physics Letters*, 97(4):041110, 2010.

[14] M. R. Ayers and A. J. Hunt. Visibly photoluminescent silica aerogels. *Journal of Non-Crystalline Solids*, 217(23):229 – 235, 1997.

[15] I. H. Campbell and P. M. Fauchet. The effects of microcrystal size and shape on the one phonon Raman-spectra of crystalline semiconductors. *Solid State Communications*, 58(10):739–741, 1986.

[16] Z. F. Sui, P. P. Leong, I. P. Herman, G. S. Higashi, and H. Temkin. Raman analysis of light-emitting porous silicon. *Applied Physics Letters*, 60(17):2086–2088, 1992.

[17] A. G. Cullis, L. T. Canham, and P. D. J. Calcott. The structural and luminescence properties of porous silicon. *Journal of Applied Physics*, 82(3):909–965, 1997.

[18] M. N. Islam and S. Kumar. Influence of crystallite size distribution on the micro-Raman analysis of porous Si. *Applied Physics Letters*, 78(6):715–717, 2001.

[19] Y. Kanemitsu, H. Uto, Y.i Masumoto, T. Matsumoto, T. Futagi, and H. Mimura. Microstructure and optical properties of free-standing porous silicon films: Size dependence of absorption spectra in Si nanometer-sized crystallites. *Physical Review B*, 48:2827–2830, 1993.

[20] K. H. Khoo, A. T. Zayak, H. Kwak, and James R. Chelikowsky. First-principles study of confinement effects on the Raman spectra of Si nanocrystals. *Physical review letters*, 105:115504, 2010.

[21] B. Humbert, A. Burneau, J. P. Gallas, and J. C. Lavalley. Origin of the Raman bands, D1 and D2, in high surface-area and vitreous silicas. *Journal of Non-Crystalline Solids*, 143(1):75–83, 1992.

[22] B. Riegel, I. Hartmann, W. Kiefer, J. Gro, and J. Fricke. Raman spectroscopy on silica aerogels. *Journal of Non-Crystalline Solids*, 211(3):294 – 298, 1997.

[23] S. Guha, P.r Steiner, and W. Lang. Resonant raman scattering and photoluminescence studies of porous silicon membranes. *Journal of Applied Physics*, 79(11):8664–8668, 1996.

[24] F. Agullo-Rueda, J. D. Moreno, E. Montoya, R. Guerrero-Lemus, and J. M. Martinez-Duart. Influence of wavelength on the raman line shape in porous silicon. *Journal of Applied Physics*, 84(4):2349–2351, 1998.

[25] S. L. Zhang, W. Ding, Y. Yan, J. Qu, B. Li, L. Li, K. T. Yue, and D. Yu. Variation of raman feature on excitation wavelength in silicon nanowires. *Applied Physics Letters*, 81(23):4446–4448, 2002.

[26] R. Al-Oweini and H. Ei-Rassy. Synthesis and characterization by FTIR spectroscopy of silica aerogels prepared using several Si(OR)(4) and R" Si(OR')(3) precursors. *Journal of Molecular Structure*, 919(1-3):140–145, 2009.

Chapter 4

Energy Transfer from Silicon Nanocrystals to Molecular Oxygen

4.1 Introduction

As mentioned in chapter 1, oxygen molecules (O_2) have a unique ground triplet electronic state. To create excited states of O_2, which is forbidden by direct photoexcitation, Si nanoparticles are adopted for transferring energy to O_2. This chapter will give an account of the transfer energy from Si nanoparticles to oxygen molecules. The first section of this chapter reviews the evidence for the magnetic field effect on silicon nanoparticles. It will then go on to the energy transfer process between silicon nanocrystals and molecular oxygen and its field dependence. Finally, the theoretical model of the energy transfer mechanism is established and tested with the experimental results.

4.2 Effect of magnetic field on silicon nanocrystals

To examine the effect of the magnetic field on silicon nanoparticles, PL spectra of Si nanocrystals were measured in liquid He. Figure 4.1 presents the magnetic field dependence of excitons in PSi at 1.5 K. The PL emission band is broad which reflects the wide size distribution of the silicon nanocrystals in PSi samples. In the presence of a magnetic field, the PL spectra show a slight increase of the PL intensities.

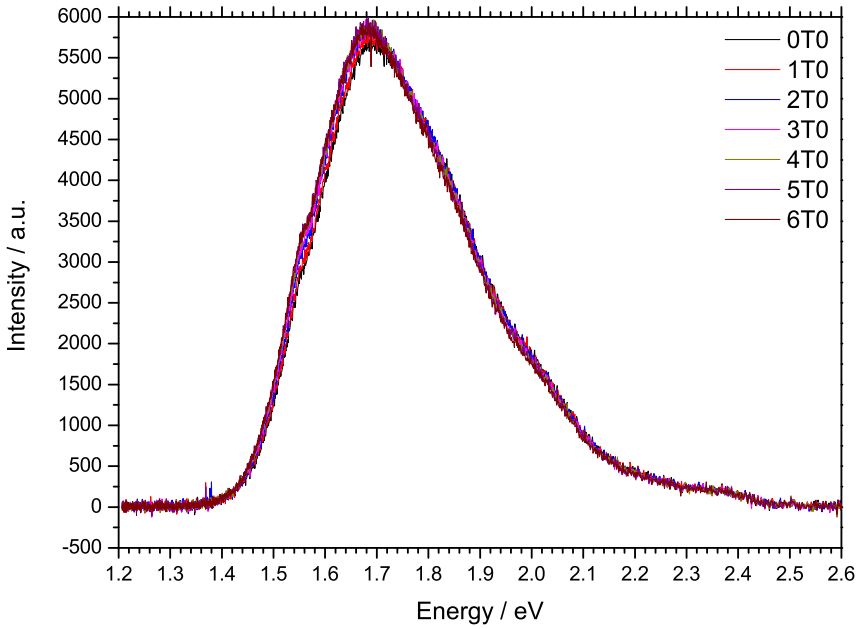

Figure 4.1: PL spectra of the PSi sample in vacuum at 1.5 K excited by E_{ex} = 2.755 eV with 4.68 mW/cm^2, magnetic field from 0 Tesla to 6 Tesla.

As mentioned before, the broad size distribution of the PL band makes the observation of any change with the magnetic field rather difficult. Therefore to investigate magnetic field effects, we introduced the intensity ratio between intensity at various B fields and intensity at zero field (I(B)/I(B=0) as a function of PL energy. The results in figure 4.2 indicate the strong evidence of the magnetic field dependence. In Figure 4.2 there is a clear trend of increasing intensity ratio I(B)/I(B=0) with raising the magnetic field at low energy range. Interestingly, at energy of about 1.75 eV the magnetic field dependence seems to have less effect.

In contrast, the intensity ratio I(B)/I(B=0) at high energy range are decreasing with the increasing of the magnetic field.

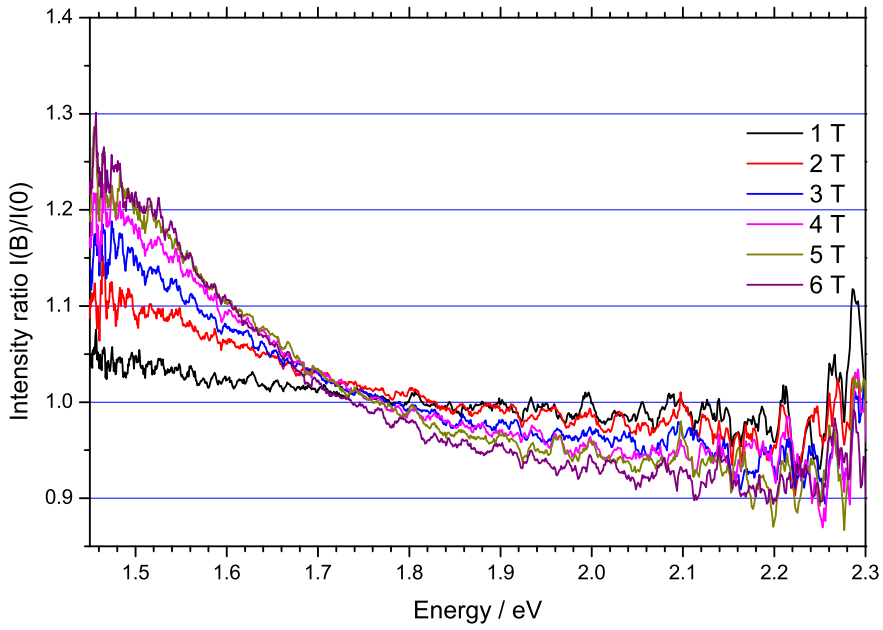

Figure 4.2: PL intensities ratio (I(B)/I(B=0)) at various magnetic fields as a function of PL energy. At energy range beyond 2.1 eV, the noisy ratios have arisen from the PL band edge.

Figure 4.3 compares the intensity ratio I(B)/I(B=0) at various energy as a function of magnetic fields. From the graph in figure 4.3, it is apparent that I(B)/I(B=0) at low PL energy has a strong magnetic field dependence as presented by PL energy at 1.55 eV and 1.63 eV in figure 4.3. At low magnetic fields (about 1 to 3 Tesla) the intensity ratio I(B)/I(B=0) of 1.55 and 1.63 eV gradually rise. Whereas when the magnetic field is increased furthers, the intensity ratio I(B)/I(B=0) of 1.55 and 1.63 eV are approximately constant with the magnetic field. On the other hand the I(B)/I(B=0) at high PL energy as shown at 1.73 and 1.86 eV in figure 4.3, they are more likely to be independent of the magnetic field.

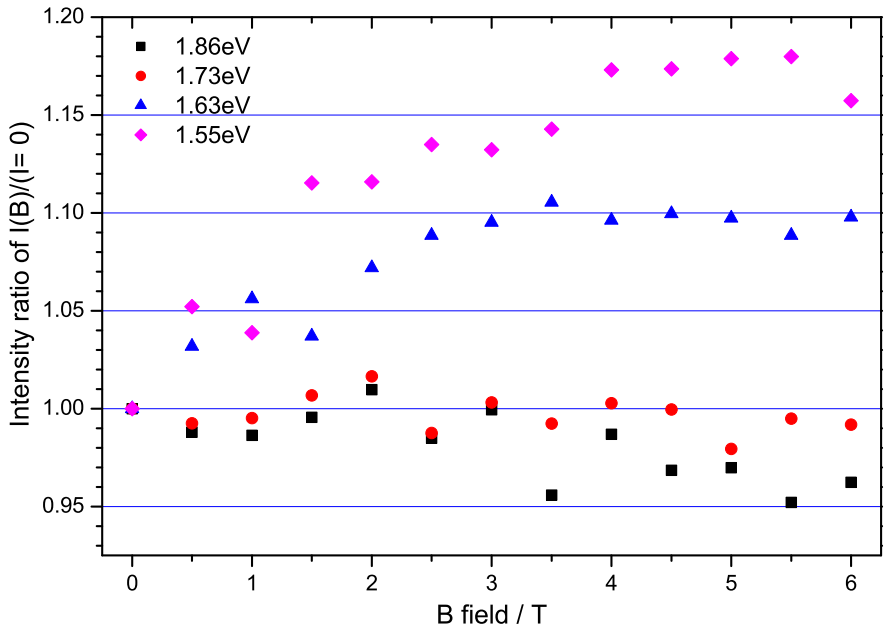

Figure 4.3: Magnetic field dependence of PL intensities compared with the zero field at various PL energy at T=1.5 K.

4.3 Energy transfer of silicon nanocrystal to O_2

The transfer energy between excitons confined in Si nanocrystals to molecular oxygen can be examined by measuring PL spectra of Si nanocrystals in vacuum and in gaseous oxygen for comparison. These experiments were carried on at liquid He temperatures to avoid the thermal broadening effects at elevated temperature.

Figure 4.4 demonstrates a normalised PL spectrum of PSi in vacuum (black spectrum) and a PL spectrum of PSi oxygen ambient (red spectrum). In vacuum, the PL spectrum has a broad and featureless band which indicates the wide bandgap distribution of Si nanocrystals assemblies. It clearly shows that in the presence of molecular oxygen, the PL spectrum is quenched and exhibits the fine structure. This drastic change is due to the oxygen molecules that are physisorbed on the surface of Si nanocrystals. The photoexcited excitons formed in the triplet state are exchanged to O_2 in its triplet ground state [1]. The strong suppression is observed above energy of 1.63 eV (indicated by dashed line) which corresponds

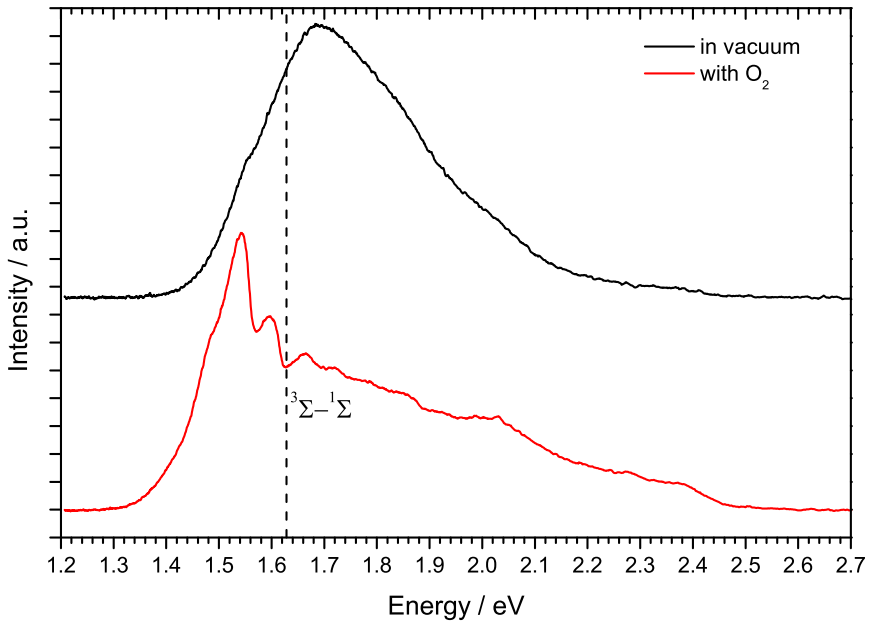

Figure 4.4: Comparison of a normalised PL spectrum from PSi in vacuum (black solid line) with a normalised PL spectrum from PSi with O_2 adsorbed at the surface of Si nanocrystals (red solid line) at T=1.5 K. Excited energy is 2.755 eV with 46.75 mW/cm^2. The black dash line shows the energy transition between $^3\Sigma$ to $^1\Sigma$ states in energy transfer process.

to the $^3\Sigma$ to $^1\Sigma$ transition. Energy transfer between Si nanocrystals assemblies and O_2 can generate either the first excited $^1\Delta$ singlet state (0.98 eV above the $^3\Sigma$ ground state) or the next higher $^1\Sigma$ singlet state (1.63 eV above the $^3\Sigma$ ground state) depending on the band gap of Si nanoparticles [2]. If Si nanocrystals have a bandgap energy higher than 1.63 eV (the $^3\Sigma$ - $^1\Sigma$ transition), the $^1\Sigma$ state is formed efficiently, due to the triplet-triplet annihilation and angular momentum conservation [3]. However, the formation of the $^1\Delta$ state has less efficiency resulting from its nonzero orbital angular momentum equal to 2, therefore the $^3\Sigma$ - $^1\Delta$ transition is spin and orbital angular momentum forbidden [3, 4].

The fact that the PL quenching is obvious in a presence of O_2, shows strong evidence of the $^1O_2$ generation. This energy transfer process is irreversible owing to the fast relaxation of the $^1\Sigma$ state either to the $^1\Delta$ or $^3\Sigma$ states [4, 5]. Also the energy of the $^1\Delta$ state, even if the relaxation is slow, is below the bandgap of bulk Si. However, this quenching can be recovered to the initial emission after the removal of oxygen molecules. To display the effect of the wide size distribution

of Si nanoparticles, the strength of PL quenching is introduced as the ratio of PL intensity measured in vacuum and the PL intensity measured with oxygen present.

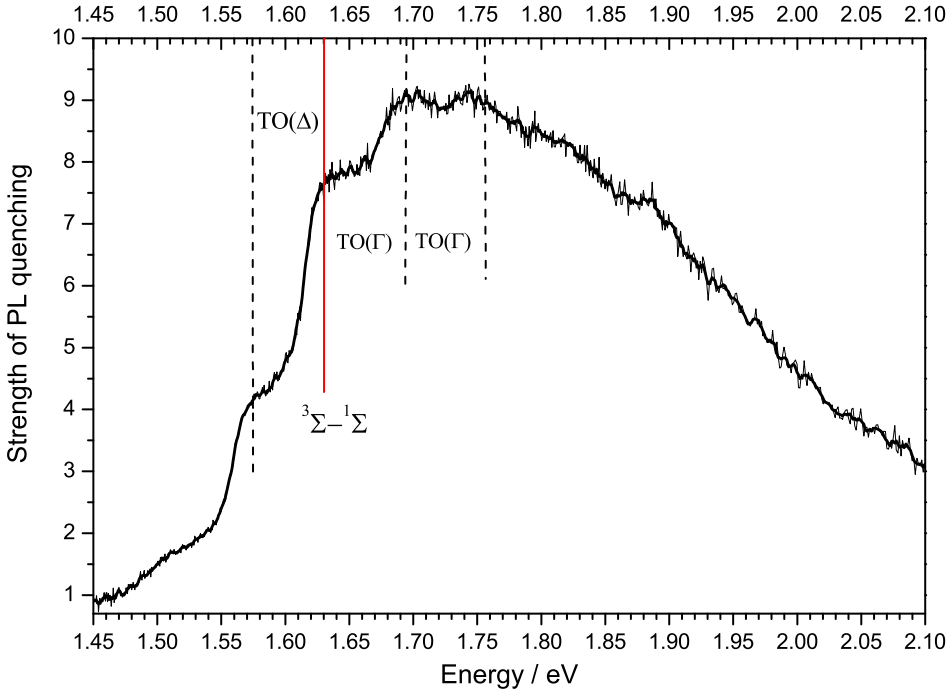

Figure 4.5: Strength of PL quenching as a function of PL energy at T=4 K with laser 2.755 eV. Phonon features are shown by the dashed lines which relate to multiple TO-phonon emission including energy conserving phonons (TO(Γ)= 63 meV) and one momentum conserving phonon (TO(Δ)= 56 meV).

The strength of PL quenching obtained from the PL spectra in figure 4.4 is presented in figure 4.5. As can be seen from the graph, the most efficient energy transfer is in the energy band near 1.63 eV that coincides with the $^3\Sigma$ to $^1\Sigma$ of O_2 transition. The efficiency of the energy transfer depends on the character of the Si nanocrystals itself e.g. exciton lifetime, presence of nonradiative centres and surface termination and so on. and the concentration of physisorbed molecular oxygen [1, 3]. This result also shows the periodic spectral features which can be implied as the multiple phonons which help conserve energy during the transfer energy process [1, 2]. To obtain the explicit multiple phonon feature, its second derivative is produced as shown in figure 4.6.

Figure 4.6 illustrates the phonon-assisted energy transfer. By considering Si

nanocrystals having a bandgap at 1.63 eV, the transverse optical phonon TO(Δ) 56 meV is observed below $^1\Sigma$ as shown in figure 4.4, 4.5 and 4.6. This result can be explained by the fact that the conduction band of bulk Si is located near the X point of the Brillouin zone therefore the recombination process needs phonons to conserve the momentum. Similarly, many studies also reported the TO(Δ) phonon assisted transition in Si nanocrystals even for small Si nanocrystals [6, 7, 8].

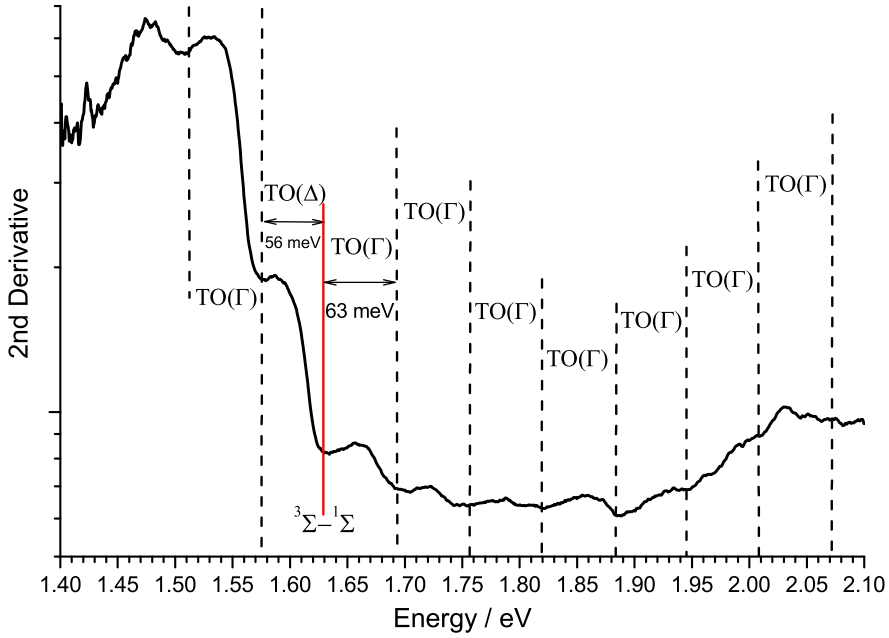

Figure 4.6: 2nd derivative of the PL from PSi with adsorbed O_2.

For the excitons having excess energy compared with the energies of $^1\Sigma$ and $^1\Delta$, the multiple phonons are emitted as shown in figure 4.6. This finding can be explained by the mechanism of energy transfer from excitons to oxygen molecules as provided in figure 4.7. This diagram shows how the formation of the singlet O_2 states occurs. For a nonresonant energy transfer process, the excess energy is dissipative via multiple phonon emission which mainly emits from the highest density of states [10]. In bulk Si, these phonons are transverse optical phonons (TO(Γ)) which are close to the centre of the Brillouin zone corresponding with the energy of 63 meV [10]. As can be seen in figure 4.7, the energy transfer takes place when the bandgap of the Si nanocrystals coincides with the excitation energy of the O_2 singlet state plus an integer number of TO phonon energies. Otherwise, a Si nanocrystal requires an additional acoustic phonon emission in order to fulfill

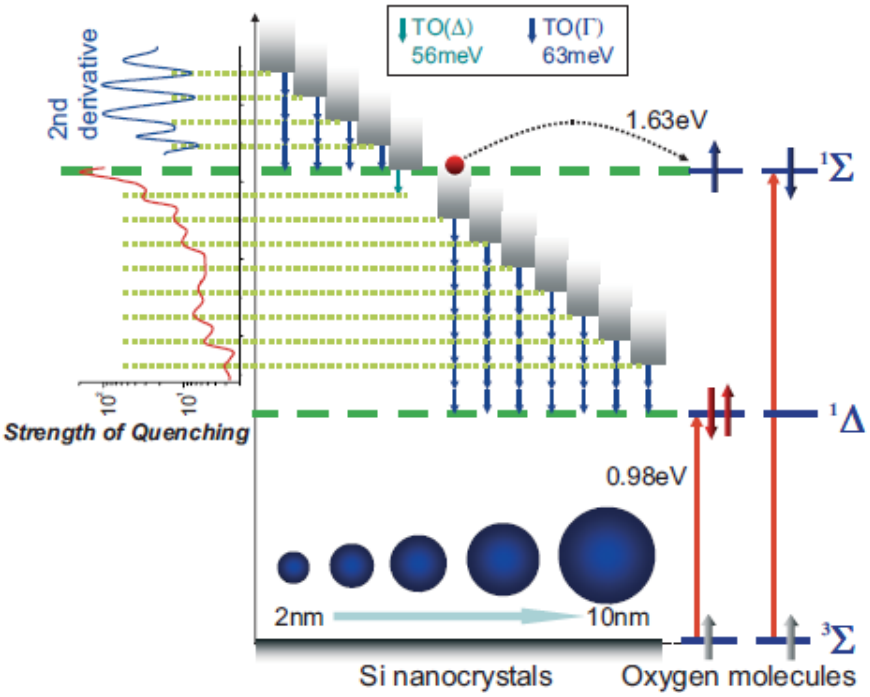

Figure 4.7: Schematic energy diagram of O_2 during energy transfer process and the phonon assisted transition reproduced from reference [9]. The surplus exciton energy is released by the multiple phonons assistance as shown by the blue arrow with corresponding to the energy-conserving TO(Γ) phonons of energy 63 meV. At $^1\Sigma$, energy exchange occurs from a photoexcited electron in Si nanocrystals (represented by the red sphere) with a non-excited electron belonging to O_2 (represented by the grey arrow). The momentum-conserving TO(Δ) phonon is indicated by the cyan arrow.

energy conservation, which causes the energy transfer rate to be efficient [11]. Due to the indirect bandgap of Si nanocrystals, exciton radiative recombination needs the emission of a bulk Si TO phonon (TO(Δ)) of 56 meV for conserving momentum as presented by the cyan arrow in the diagram.

4.3.1 O_2 concentration dependence

As mentioned in section 4.3, one of the most significant parameters that varies the efficiency of the energy transfer is the concentration of physisorbed molecular oxygen. In order to establish this effect, PL measurements were carried on the same PSi sample by varying O_2 concentration. Figure 4.8 compares the results obtained from various adsorbed molecular oxygen concentration.

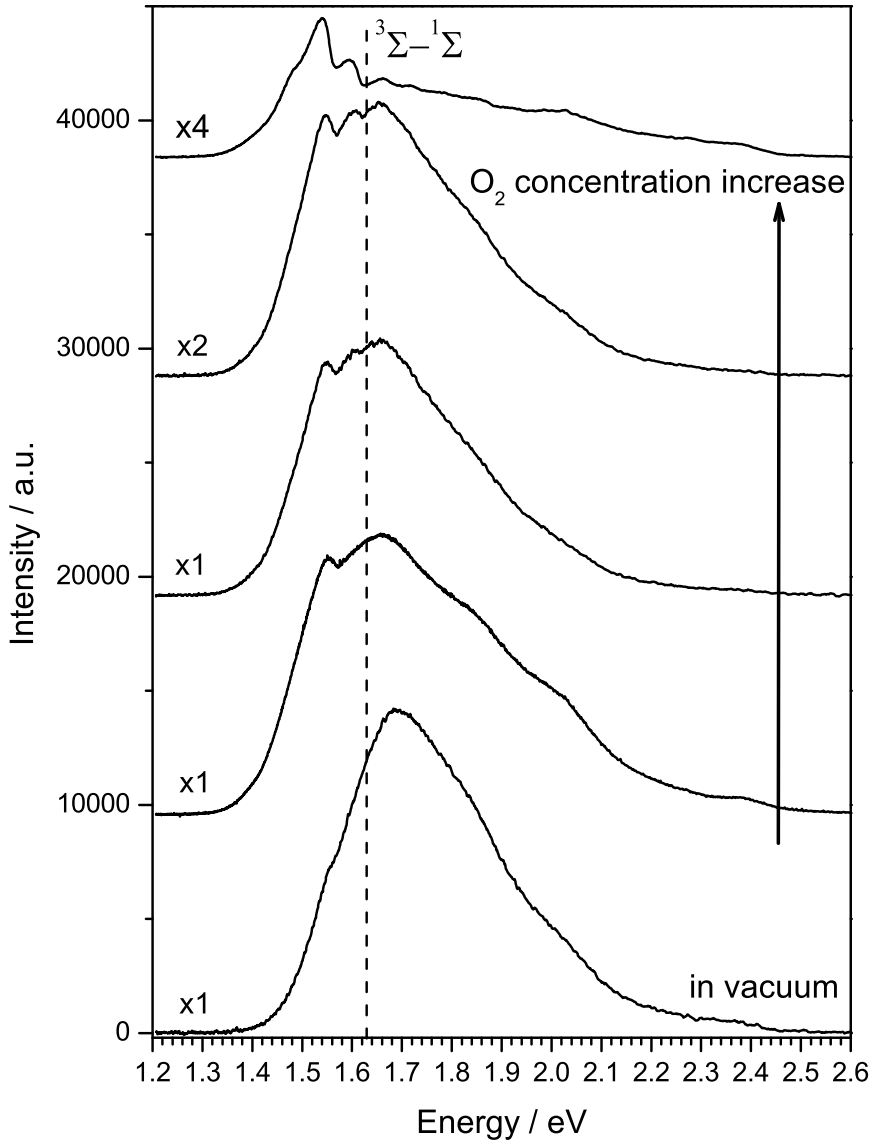

Figure 4.8: Comparison between PL spectrum of PSi in vacuum (the bottom line) and PL spectra of PSi with different adsorbed O_2 concentration at T = 1.5 K. The dash line indicates the energy transition between $^3\Sigma$ and $^1\Sigma$ states in energy transfer process. Excited energy is 2.755 eV with 23.38 mW/cm^2. Arrow line indicates the increased direction of O_2 concentrations. For better comparison, spectra at high-physisorbed O_2 are scaled by the indicated multiplication factor.

In vacuum, the PL spectrum of PSi samples shows a broad featureless emission band in the energy range 1.35 - 2.6 eV. In the presence of O_2, the PL spectrum from the lowest O_2 concentration starts to reveal the phonon TO(Δ) at energy below $^1\Sigma$ and its intensity drops slightly compared with the PL intensity with no physisorbed O_2. This shows that the energy transfer between Si nanocrystals and oxygen molecules exists even though the efficiency is less. When the O_2 concentration increases, the intensities of the PL spectra decrease gradually, whereas the spectra display a significant increase in phonon features. At the highest O_2 concentration, the quenching suppresses significantly, causes a raising of the energy transfer efficiency as shown in the top spectrum in figure 4.8. These findings suggest that increasing the O_2 concentration provides more oxygen molecules which access the Si nanocrystal surface.

4.3.2 Power dependence

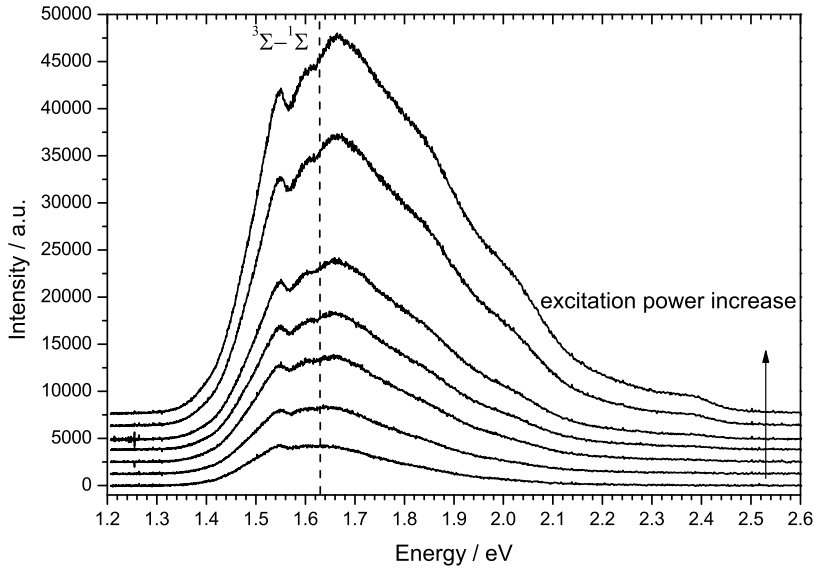

Figure 4.9: Selections of PL spectra of PSi sample with adsorbed O_2 at the surface of Si nanocrystals at various excitation powers at T = 1.5 K. The dash line indicates the energy transition between $^3\Sigma$ and $^1\Sigma$ states in energy transfer process. Non-focus excited energy is 2.755 eV. Arrow line indicates the increased direction of powers.

The PL intensity and peak of the PSi spectrum is sensitive to the excitation intensity. Several studies have reported that there is a blue shift in PL spectrum

as the effect of increasing the incident flux on the PSi sample [12, 13, 14]. The effect can be explained as a result of independent absorption and luminescence of different particles sizes. Commonly, the lifetime of higher energy (smaller nanocrystals) is shorter than at lower energy (larger nanocrystals). When the intensity of excitation is increased, PL intensity at low photon energy reaches its saturated level first, whereas at high photon energy, the PL intensity still increases linearly. Therefore, the PL spectrum shifts to higher energy until the excitation intensity is high enough to make the whole spectrum range reaches its saturation [13, 15]. In the excitation process, the population of larger Si nanocrystals saturates more rapidly than the smaller nanocrystals thus producing a peak shift.

Turning now to the experimental evidence on the effect of the incident power on PSi sample in the energy transfer process, the PL measurements are investigated at the same O_2 concentration level at various incident powers as illustrated in figure 4.9. Increasing excitation power rises up the intensities of spectra and also emphasizes the phonon feature. However, there is no evidence of the PL peak shift in the energy transfer process with the raising of excitation intensity.

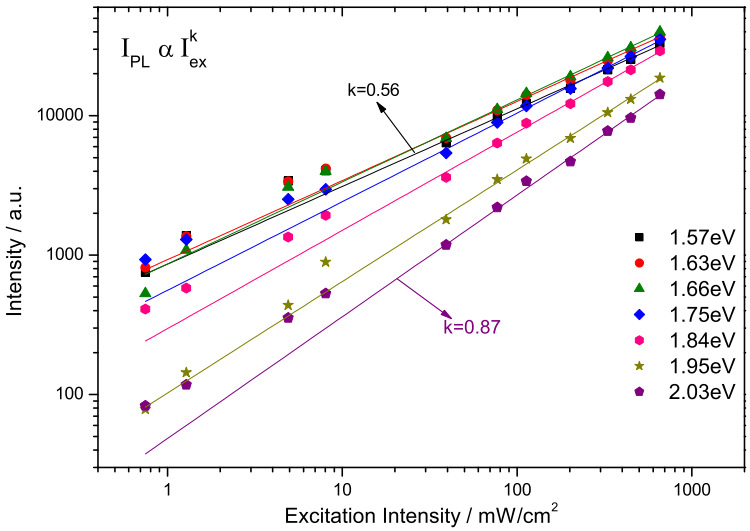

Figure 4.10: PL intensity from PSi sample with adsorbed O_2 as a function of power density at various photon energy at T = 1.5 K. Excited energy is 2.755 eV. The lines are the fitting by $I_{PL} \propto I_{ex}^{k}$, where I_{PL} is PL intensity at various detected energy from PSi, I_{ex} is excitation intensity and k is the gradient for fitting.

Consider the power dependence of the PL intensity at different energies as shown in figure 4.10. As the incident density is increased, the PL intensities for every photon energy increase steeply, especially at high energy such as 2.03 eV. From the fitting by $I_{PL} \propto I_{ex}^{k}$, the best fit gives $k = 0.87$ and 0.56 for the detection energies of 2.03 and 1.57 eV, respectively as shown in figure 4.10. These results are consistent with the lifetime of the nanocrystals which is due to the fact that smaller nanoparticles have shorter decay time than the larger nanocrystals. Therefore, the PL intensity at lower energy has a more rapid approach to saturation than the PL intensity at higher energy as indicated by the gradients (k). Nevertheless, there are no signs of the saturation phenomenon which may be explained by the fact that the selected powers are not high enough to reach the saturation point. In the energy transfer process, however, this might be due to the excited nanoparticles transferring energy to adsorbed oxygen molecules. Therefore, the excitons in the excited state do not reach their saturated points.

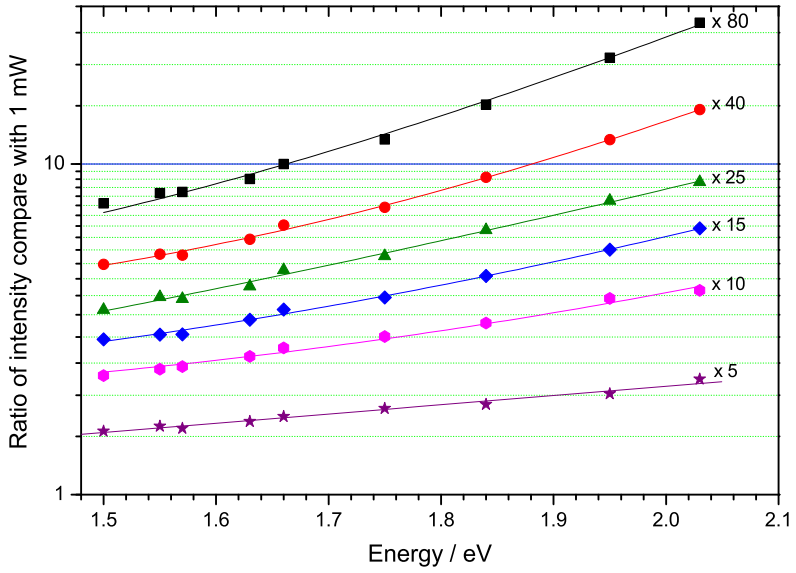

Figure 4.11: Ratio of PL intensity from PSi sample with adsorbed O_2 as a function of PL energy at the selection of various excited powers in mW unit compared with the excited power of 1 mW. Exited energy is 2.755 eV at 1.5 K. Numbers indicate the excitation power relative to 1 mW. The solid lines guide to the eye.

To present the energy dependence of the incident powers, the comparison of PL intensity at different excited powers with the 1 mW incident power ratio is created. It is clearly seen in figure 4.11 that at higher detected energies the PL intensity ratio increases rapidly compared to the lower energies.

4.4 Effect of magnetic field on the energy transfer process

As mentioned in section 4.1, the ground energy state of molecular oxygen is in a triplet state [4, 5, 3] and the spin state of Si nanocrystal forms singlet-triplet excited states [16, 17]. In direct electron exchange energy transfer, the orientation of spins is crucial. It occurs only between electrons having opposite mutual spin orientation [2, 9, 18]. In order to verify the spin influence on the energy transfer process, the magnetic field dependence of the PL spectra with adsorbed O_2 was studied.

Considering the electronic states at zero magnetic field, the energy levels of the triplet excitons and the triplet ground state of O_2 are each threefold degenerate. All states are populated with equal probability, the spin conservation is satisfied and the energy transfer happens to create the singlet oxygen. Figure 4.12 illustrates the magnetic field dependence of the quenched PL spectra. At B=0, PL quenching is presented by the black line. When magnetic field is applied, the three fold degeneracy is lifted by Zeeman splitting as shown in inset of figure 4.12. The energy spitting is given by

$$\Delta \mathrm{E} = g\mu_{\mathrm{B}}\mathbf{B},$$

where g is the Landé g-factor ($g_{\mathrm{exciton}} \sim g_{\mathrm{O_2}} \sim 2$ [19]), μ_{B} is the Bohr magnetron and $\mathbf{B}$ is the external magnetic field. At low temperatures, the magnetic field causes the alignment of both exciton spins and molecular oxygen spins to be in the same direction as spin down states. Therefore spin-flip is prohibited via exchange between electrons of photo-generated excitons confined in PSi and O_2. Thus, the energy exchange efficiency of this process reduces with increasing magnetic fields, which results in the PL intensity recovery.

Interestingly, at low magnetic field the PL intensities at some energy ranges drops then starts to rise up gradually at high magnetic field as presented in figure 4.12. This correlation can be seen clearly by introducing a ratio between the PL intensities at certain magnetic fields I(B) and the PL intensities at zero field I(B=0) as demonstrated in figure 4.13. The magnetic field dependence of the ratio I(B)/I(B=0) from PSi with O_2 adsorbed to the surface of Si nanocrystals

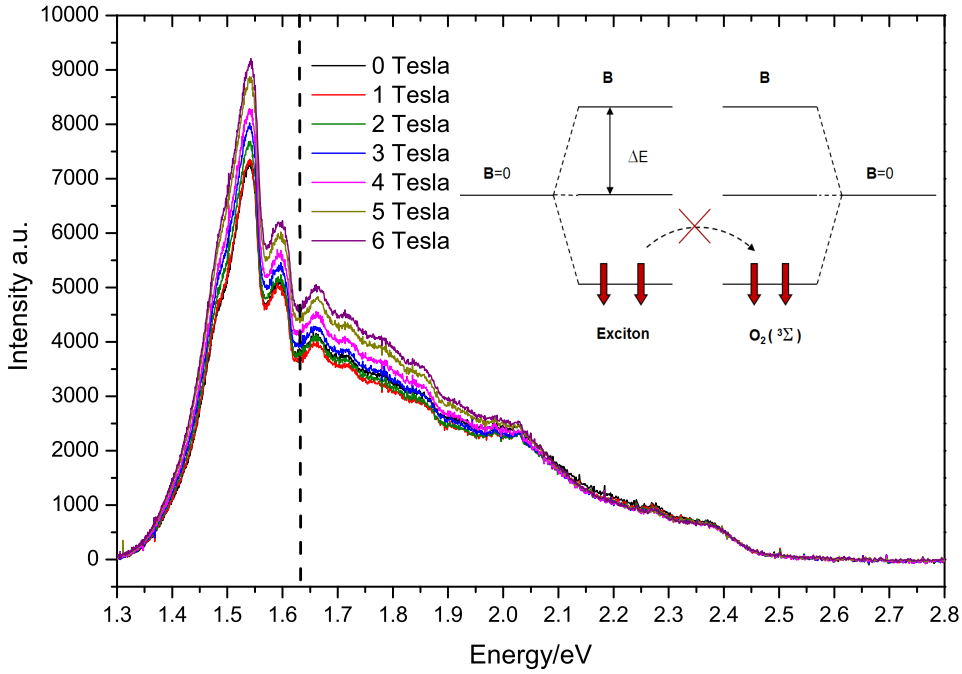

Figure 4.12: PL spectra of PSi with adsorbed O_2 at various magnetic fields from 0 to 6 Tesla at T = 1.5 K with excited energy 2.755 eV of 45.45 mW/cm^2. The dash line presents the energy transition between $^3\Sigma$ to $^1\Sigma$ states in energy transfer process. Inset: Sketch Zeeman splitting of the triplet exciton state and the $^3\Sigma$ triplet ground state of O_2. Arrows represent the spin orientations of electrons. ΔE is the Zeeman splitting. See text for details.

at several PL energies is shown. At an energy of 1.55 eV, below the $^3\Sigma$ - $^1\Sigma$ transition, the PL intensity ratio recovers up to 1.3 times at 6 Tesla compared with the zero field. The results of interest here are shown at higher detection energies such as 1.63 and 1.73 eV. Below 2.5 Tesla, the PL ratios are below 1 which means the intensities at low magnetic field have dropped slightly then rise up again when the magnetic field is over 2.5 Tesla. This trend carries on until at detection energies of 2.1 eV or above, the PL intensities are slightly decreased as a function of magnetic fields as presented via the red-circles and the black-squares in figure 4.13.

In order to understand how the magnetic field regulates the intensity ratio over the energy range, a series of the PL intensity ratio as a function of PL energies with the different magnetic fields is performed in figure 4.14. It is apparent from this figure that the appearance of phonon features gets stronger with increas-

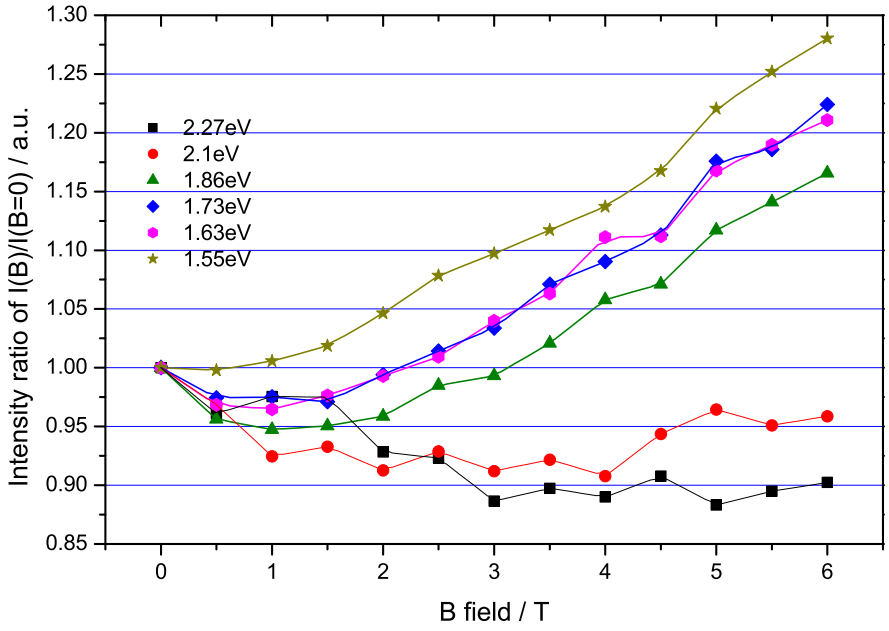

Figure 4.13: PL intensities ratio (I(B)/I(B=0)) as a function of magnetic fields at various detection energies obtained from PL spectra in figure 4.12. The solid lines are guides to the eyes.

ing magnetic field. What is interesting in these graphs are that the intensity ratios I(B)/I(B=0) increase with raising the magnetic field at energy range below 1.55 eV. On the contrary, over this energy especially at low magnetic fields, I(B)/I(B=0) ratios are decreased corresponding with the increasing of the magnetic field. These findings may help us to clarify the detailed mechanisms of the energy transfer process and to model it.

4.5 Modeling

This section will provide the concepts required to establish the energy transfer mechanism model, based on ideas about donor-acceptor recombination that was undertaken by Dunstan and Davies [20]. The spin Hamiltonian for the exciton states can be presented:

$$H_{ex} = \mu_B \sum_{i,j} g_{ij} B_i s_j + \sum_{i,j} \delta_{ij} s_i s_j, \tag{4.1}$$

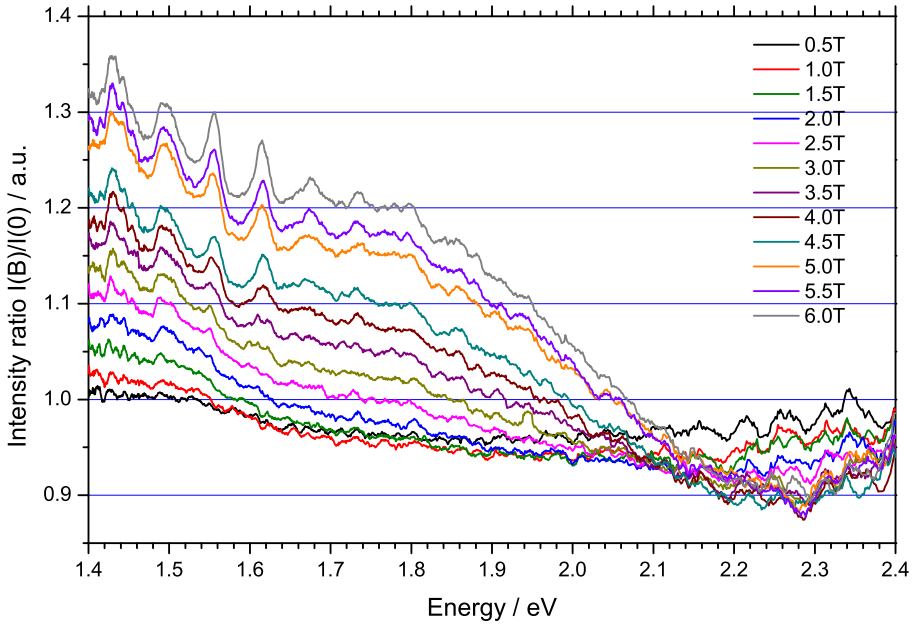

Figure 4.14: PL intensities ratio (I(B)/I(B=0)) at various magnetic fields as a function of PL energy.

where g_{ij} is the g tensor, s is spin operators and δ_{ij} is a fine structure tensor giving a zero field splitting parameter of Si exciton. However, the zero field splitting of the Si exciton is very small, equal to 0.0055 meV [16], therefore this zero field splitting term will be neglected. The equation 4.1 can be simplified to

$$H_{ex} = g\mu_B B \cdot s. \tag{4.2}$$

For the excited exciton states, there are two basic approaches currently being adopted in Si nanocrystals. One is the case of a small regular shape nanocrystal (x = y = z) such as embedded Si nanocrystals in a SiO_2 matrix and the other is an irregular nanocrystal (x≠ y≠ z) that is fabricated by electrochemically etching likes PSi. For the regular nanostructure, quantum confinement causes the splitting of a valence band into a heavy hole and a light hole band at Γ point as presented in diagram of figure 4.15 (a). The heavy hole band is formed from p-like orbitals therefore the total angular momentum of hole state is $J_{hh}=\frac{3}{2}$. The conduction band is formed from s orbitals with a total angular momentum of electron state $J_e=\frac{1}{2}$. Hence, the total angular momentum of an exciton $J_{ex} = 2$ or $J_{ex} = 1$. The exchange interaction causes the degeneracy of the exciton states

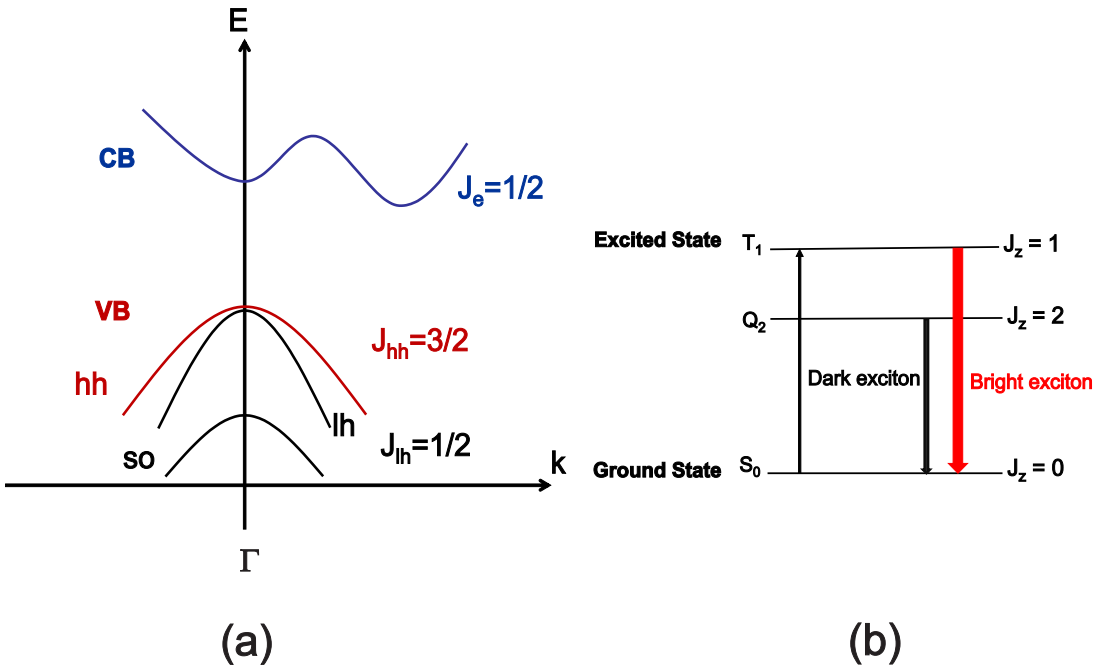

Figure 4.15: Schematic diagram of Si nanoparticles of regular shape. (a) The electronic band structure of Si nanocrystal: the conduction band (CB) is represented by blue line and the valence band (VB) is split into heavy hole (hh), light hole (lh) and spin-orbit (so) bands by quantum confinement. (b) The excitonic fine structure of the first two excited states T_1 (triplet) and Q_2 (quintet) .

are lifted up to a triplet and a quintet as shown in figure 4.15 (b). There are many published studies reporting that the J_{ex}=1 state is higher energy than the J_{ex}=2 state [21, 22, 23]. Due to the dipole forbidden transition of the J_{ex}=2 state (as illustrated by the black arrow), these excitons are labelled as dark excitons. Whereas, the transition of excitons from the J_{ex}= 1 state (as presented by the red arrow)are marked as bright excitons.

On the other hand, the valence band degeneracy of irregular Si nanostructures is lifted by the quantum confinement. For simplification, the orbital coupling is neglected, therefore the quantised energy level in the valence band can be marked as P_x, P_y and P_z as presented in figure 4.16 (a) with effective spin J = $\frac{1}{2}$. The effect of the magnetic field B is shown in figure 4.16 (b). The exciton triplet state is split into three levels with m_l equal to 1, 0 and -1 where m is the z component of the exciton spin [16].

Mainly, the samples in this study are PSi, hence, the best approach to adopt for the exciton states is the irregular shape model. There are many published studies observing the g value of PSi of $\approx$ 2 (for example, Hecker et al., 1999; Diener et

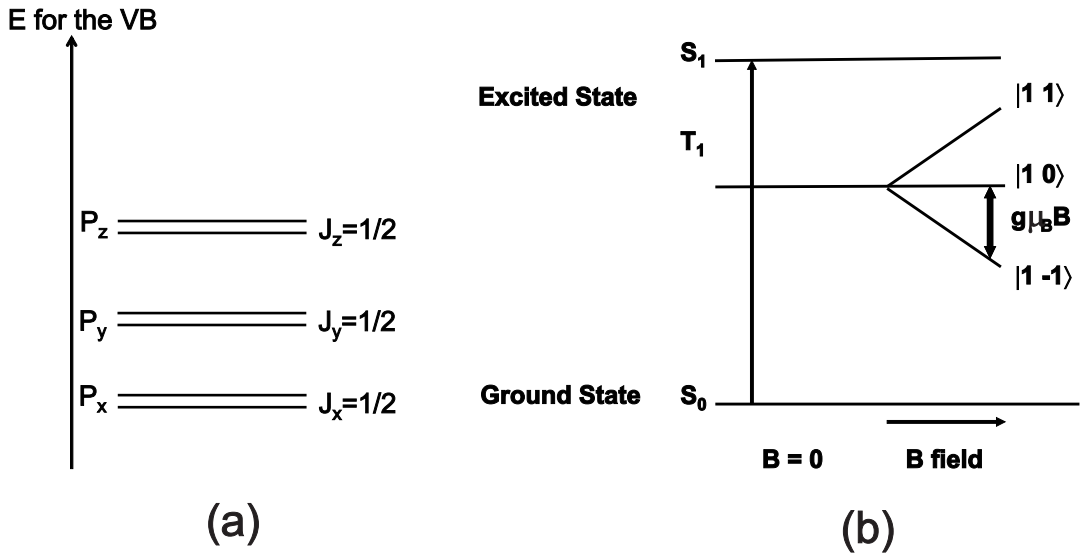

Figure 4.16: Schematic diagram of Si nanoparticles with irregular shape. (a) The valence band of Si nanocrystal: the valence band (VB) is split into P_x, P_y and P_z bands with the total angular momentums of $J_x = J_y = J_z = \frac{1}{2}$. (b) The excitonic fine structure of the first two excited states S_1 (singlet) and T_1 (triplet) at B=0 compares with the presence of magnetic field. As a result of Zeeman effect, the exciton triplet states $|+1\rangle$ and $|-1\rangle$ are raised and lowered, respectively.

al., 2001). For Diener et al. reported a linear downward shift with increasing external magnetic field due to the Zeeman effect of the lowest exciton state (m = -1) and estimated the g factor of the exciton ≈ 2 [24]. This study produced results which corroborate the findings of the previous work of Heckler et al. [25]. The finding confirms the linear Zeeman spin splitting of the triplet ground state of excitons confined in the Si nanoparticles and gave the g factor of ≈ 2. In both publications, results are obtained from PSi samples which support our irregular shape model. Therefore, $s = 1$ and g = 2.0 in equation 4.2 and the spin states $m_s = +1$, 0 and -1. In this model. we assume that the exciton spin states are irrespective of the magnetic field direction.

The spin Hamiltonian for the ground triplet oxygen states is similar to the exciton states as shown in equation 4.3

$$H = \mu_B \sum_{i,j} G_{ij} B_i S_j + \sum_{i,j} D_{ij} S_i S_j, \tag{4.3}$$

where subscripts i, j refer to Cartesian coordinate (x, y, z), B is a magnetic field, μ_B is a Bohr magnetron, G_{ij} is the oxygen g tensor, S is spin operators and D_{ij}

is a fine structure tensor or a zero field splitting parameter. The first term in equation 4.3 is the linear Zeeman term. The second term is the zero-field splitting or fine structure term. D_{ij} is real and symmetric, so can be diagonalized. Then equation 4.3 can be expressed as

$$H_{O_2} = G\mu_B \left(B_x S_x + B_y S_y + B_z S_z\right) + D\left(S_z^2 - \frac{1}{3}S(S+1)\right), \tag{4.4}$$

where

$$S_x = \frac{1}{\sqrt{2}}\begin{pmatrix} 0 & 1 & 0 \\ 1 & 0 & 1 \\ 0 & 1 & 0 \end{pmatrix}, S_y = \frac{1}{\sqrt{2}}\begin{pmatrix} 0 & -i & 0 \\ i & 0 & -i \\ 0 & i & 0 \end{pmatrix}, S_z = \begin{pmatrix} 1 & 0 & 0 \\ 0 & 0 & 0 \\ 0 & 0 & -1 \end{pmatrix}$$

and $\mathrm{S}^2 = \begin{pmatrix} 2 & 0 & 0 \\ 0 & 2 & 0 \\ 0 & 0 & 2 \end{pmatrix}$.

The G and D values are equal to 2.000 and 3.572 cm^{-1} (0.442909 meV) in solid air, respectively [19]. This model is based upon an assumption that O_2 will be excited to their singlet states only by adjacent excitons.

4.5.1 Oxygen orientation aligned with the magnetic field

In this section, we assume that O_2 is along the magnetic field B direction, the z axis, hence the spin Hamiltonian in equation 4.4 can be rewritten as

$$H_{O_2//z} = G\mu_B B \begin{pmatrix} 1 & 0 & 0 \\ 0 & 0 & 0 \\ 0 & 0 & -1 \end{pmatrix} + D \begin{pmatrix} \frac{1}{3} & 0 & 0 \\ 0 & -\frac{2}{3} & 0 \\ 0 & 0 & \frac{1}{3} \end{pmatrix}. \tag{4.5}$$

The eigenstates and their energies can be expressed as:

$$\phi_1 = \left(-G\mu_B B + \frac{D}{3}\right)|-1\rangle, \tag{4.6}$$

$$\phi_2 = -\frac{2D}{3}|0\rangle, \tag{4.7}$$

$$\phi_3 = \left(G\mu_B B + \frac{D}{3}\right)|+1\rangle. \tag{4.8}$$

In steady state, the numbers of oxygen molecules , which are not excited by Si excitons, are n_1,n_2 and n_3 with corresponding to the populations of three triplet states of the oxygen molecule in case of the oxygen molecule aligned on the same direction as the magnetic field, where number 1, 2 and 3 correspond to the spin states -1,0 and +1, respectively. When excitons have been created, oxygen-exciton pairs are formed in total of 3 energy levels with population $n\left[i,j\right]$. The index i represents the exciton states (i = 1, 2 and 3 correspond to the spin states -1,0 and +1, respectively), whereas j refers to the oxygen spin states as mentioned before. In energy transfer process, there are n_e oxygen molecules that have been excited to their singlet state by the Si excitons. Consequently, the total number of oxygen molecules N_0 is

$$N_0 = (n_1 + n_2 + n_3) + \Sigma n\left[i,j\right] + n_e. \tag{4.9}$$

We normalise equation 4.9 by dividing with N_0, thus

$$1 = \frac{n_1}{N_0} + \frac{n_2}{N_0} + \frac{n_3}{N_0} + \Sigma\frac{n\left[i,j\right]}{N_0} + \frac{n_e}{N_0}, \tag{4.10}$$

and a relative population can be presented as

$$1 = U + V + W + \Sigma x\left[i,j\right] + \gamma, \tag{4.11}$$

where $U = \frac{n_1}{N_0}$, $V = \frac{n_2}{N_0}$, $W = \frac{n_3}{N_0}$, $x\left[i,j\right] = \frac{n\left[i,j\right]}{N_0}$ and $\gamma = \frac{n_e}{N_0}$.

Base on the following assumption : firstly, a excitation rate (P) is constant and independent with the exciton spin state and secondly, the oxygen spin state is not changed with the exciton creation, thus, the schematic diagram of the transfer energy can be sketched in figure 4.17. In case that the exciton recombines and decays before energy transfer has occurred, recombination rates (r_1) from the exciton spin states $|-1\rangle$ and $|+1\rangle$ are equal and constant. On the contrary, the recombination rate of the spin state $|0\rangle$ (r_0) is a different rate from r_1. The exciton recombination rates are shown in figure 4.17 by orange arrows. The oxygen spin, during this exciton recombination, is assumed unmodified and can relax with equal probability and the constant rate R as represented by a cyan arrow.

In steady state, rate equations can be set up as followed:

$$0 = \frac{PU}{3} - x\left[3,1\right]r_1 - t\left[3,1\right]x\left[3,1\right], \tag{4.12a}$$

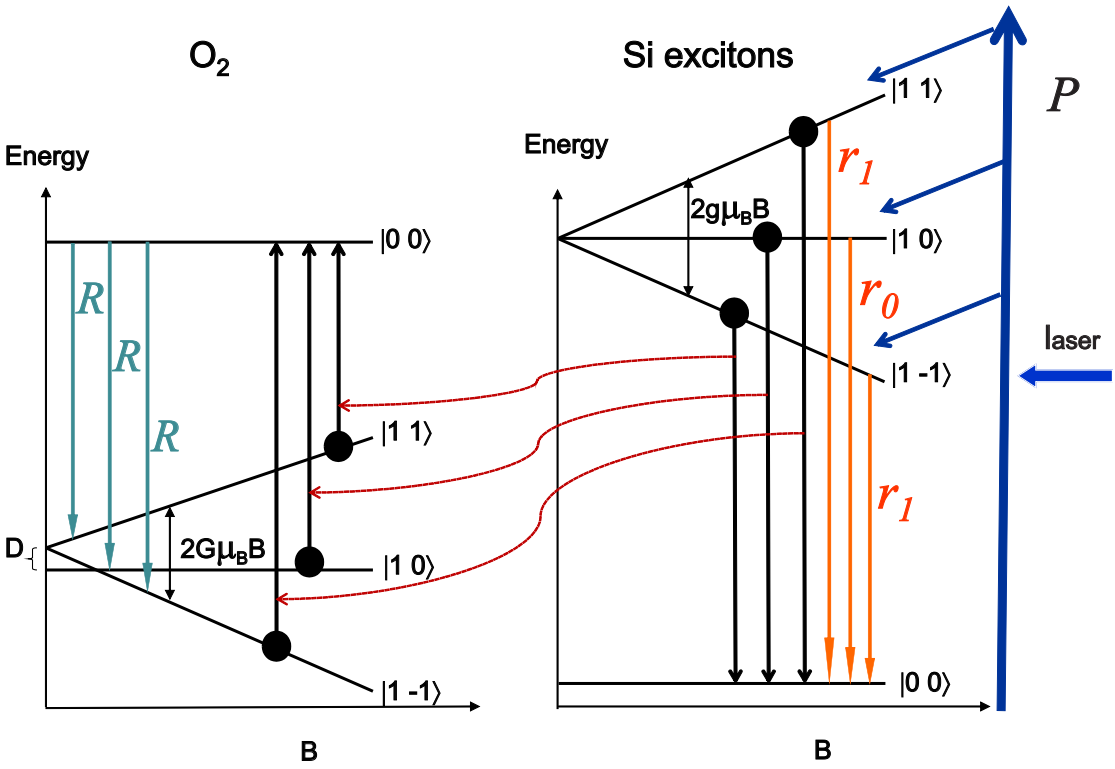

Figure 4.17: Energy transfer diagram between Si nanocrystals and oxygen molecules in case of the molecules aligned in the same direction as the magnetic field B.

$$0 = \frac{PV}{3} - x\,[2,2]\,r_0 - t\,[2,2]\,x\,[2,2]\,, \tag{4.12b}$$

$$0 = \frac{PW}{3} - x\,[1,3]\,r_1 - t\,[1,3]\,x\,[1,3]\,, \tag{4.12c}$$

$$0 = -PU + R\frac{\gamma}{3} + x\,[3,1]\,r_1, \tag{4.13a}$$

$$0 = -PV + R\frac{\gamma}{3} + x\,[2,2]\,r_0, \tag{4.13b}$$

$$0 = -PW + R\frac{\gamma}{3} + x\,[1,3]\,r_1, \tag{4.13c}$$

$$0 = (t\,[1,3]\,x\,[1,3] + t\,[2,2]\,x\,[2,2] + t\,[3,1]\,x\,[3,1]) - R\gamma \tag{4.14}$$

and equation 4.11 can be rewritten as

$$U + V + W + x\,[1,3] + x\,[2,2] + x\,[3,1] + \gamma = 1. \tag{4.15}$$

where $t\,[i,j]$ are transfer coefficients for exciton spin state $|i\rangle$ which transfers energy to the O_2 spin state $|j\rangle$ and i = 1,2 and 3 and j = 1,2 and 3. The transfer coefficients equal the square of the coefficient of the O_2 spin states. Thus, $t\,[3,1]$

$$= \left(-G\mu_B B + \frac{D}{3}\right)^2,\ t\,[2,2] = \left(-\frac{2D}{3}\right)^2 \text{ and } t\,[1,3] = \left(G\mu_B B + \frac{D}{3}\right)^2.$$

Equations 4.12a - 4.12c express the rate equations of the exciton triplet states together with the O_2 ground state. The energy transfer involves transitions which are spin conserving as shown by red arrows in figure 4.17. In steady state, the rate equations of the triplet O_2 states can be calculated as equation 4.13a to 4.13c. The rate equation for the O_2 singlet state also is presented in equation 4.14 and the total population amongst this process is shown in equation 4.15.

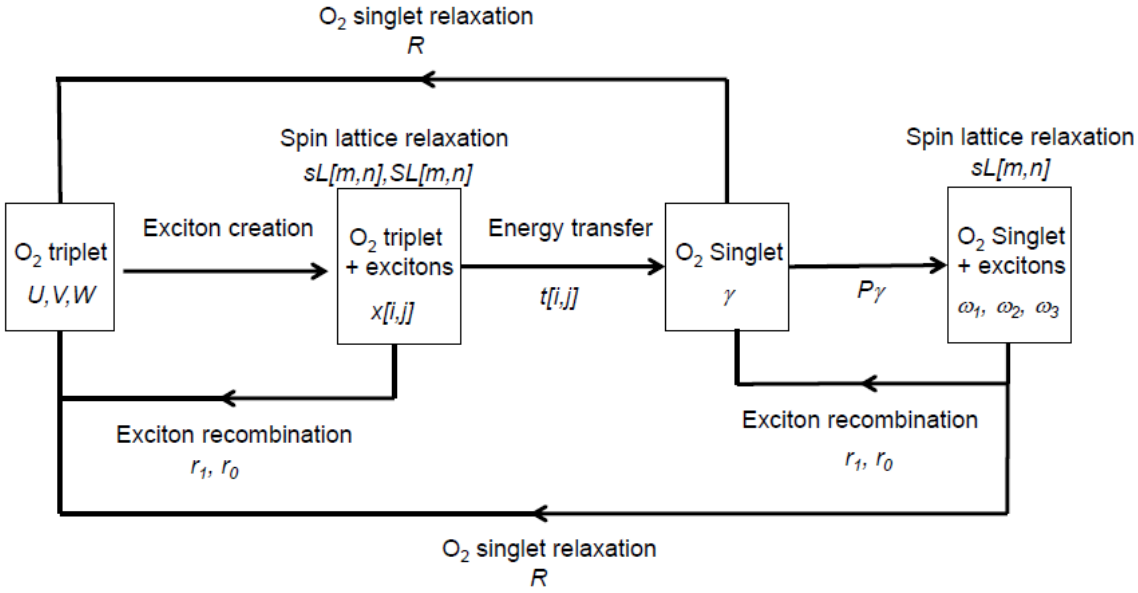

Figure 4.18: A sketch of the energy transfer process scheme between excitons and oxygen molecules.

However, these simple rate equations do not include several factors that can occur during the energy transfer process. In order to establish a more realistic model, several essential factors are introduced. A summary concept for the energy transfer model is given as illustrated in figure 4.18. First of all, in the O_2 ambient, the ground triplet O_2 states have the relative populations U, V and W. When the creation of excitons happens, the population of the excitons which are adjacent to the O_2 is $x\,[i,j]$. For a coupled system at this stage, a spin lattice relaxation can occur either by spin-flip of the exciton or by spin-flip of the O_2. The spin lattice relaxation of the exciton and O_2 are defined as $sL[m,n]$ and $SL[m,n]$, respectively, where m and n correspond to 1, 2 and 3 spin states.

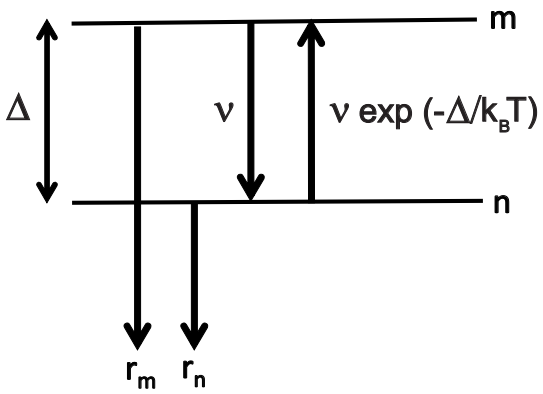

Figure 4.19: A sketch of the spin lattice relaxation idea.

Figure 4.19 shows a simple idea of the spin lattice relaxation. The energy difference between spin states m and n is Δ and r_m, r_n are recombination rates of state m and n, respectively. In this model, an assumption of thermalised population of states is taken into account. The spin relaxation rate from m to n are represented by ν and vice versa by $\nu \exp(-\Delta/k_BT)$. Note that the $\exp(-\Delta/k_BT)$ term comes from the Boltzmann distribution. For simplicity, if r_m and r_n equal to 0, therefore,

$$\frac{m}{n} = exp(-\Delta/k_BT).$$

Hence, when the spin relaxation $sL[m,n]$ and $SL[m,n]$ occur, the spin-flip rate ratio of the upwards and downwards constants must fulfill this above ratio to satisfy detailed balance. Meanwhile, the excitons can recombine with the rate r_1 and r_0 depending on their spin state. Secondly, the triplet excitons transfer their energy to triplet O_2 with the rate $t\,[i,j]$ via the spin conservation rule so that singlet O_2 is generated. This singlet O_2 can relax back to the original triplet state with the rate R. After the singlet O_2 production, the excitons are also created continuously, thus, three new variables ω_1, ω_2 and ω_3 are introduced where ω is a population of excitons in spin state as shown by indices 1,2 and 3 at which correspond to the $|-1\rangle$, $|0\rangle$ and $|+1\rangle$ states, respectively. In this situation either the excitons can recombine or the singlet oxygen can return to the ground triplet state.

These new factors have to be incorporated into equations 4.12a - 4.13c including the step of exciton creation while the O_2 is in the singlet state. According to the

above assumption, the rate equation can be adapted as presented:

$$\begin{aligned} 0 = \frac{PU}{3} &- x\,[3,1]\,r_1 - t\,[3,1]\,x\,[3,1] - sL\,[3,1]\,x\,[3,1] - sL\,[3,2]\,x\,[3,1] \\ &+ sL\,[1,3]\,x\,[1,1] + sL\,[2,3]\,x\,[2,1] - SL\,[1,3]\,x\,[3,1] \\ &- SL\,[1,2]\,x\,[3,1] + SL\,[3,1]\,x\,[3,3] + SL\,[2,1]\,x\,[3,2] + \omega_3 R, \end{aligned} \tag{4.16a}$$

$$\begin{aligned} 0 = \frac{PV}{3} &- x\,[2,2]\,r_0 - t\,[2,2]\,x\,[2,2] - sL\,[2,1]\,x\,[2,2] - sL\,[2,3]\,x\,[2,2] \\ &+ sL\,[1,2]\,x\,[1,2] + sL\,[3,3]\,x\,[3,2] - SL\,[2,3]\,x\,[2,2] \\ &- SL\,[2,1]\,x\,[2,2] + SL\,[3,2]\,x\,[2,3] + SL\,[1,2]\,x\,[2,1] + \omega_2 R, \end{aligned} \tag{4.16b}$$

$$\begin{aligned} 0 = \frac{PW}{3} &- x\,[1,3]\,r_1 - t\,[1,3]\,x\,[1,3] - sL\,[1,2]\,x\,[1,3] - sL\,[1,3]\,x\,[1,3] \\ &+ sL\,[2,1]\,x\,[2,3] + sL\,[3,1]\,x\,[3,3] - SL\,[3,1]\,x\,[1,3] \\ &- SL\,[3,2]\,x\,[1,3] + SL\,[1,3]\,x\,[1,1] + SL\,[2,3]\,x\,[1,2] + \omega_1 R, \end{aligned} \tag{4.16c}$$

$$\begin{aligned} 0 = -PU + R\frac{\gamma}{3} &+ x\,[3,1]\,r_1 - SL\,[1,2]\,U \\ &- SL\,[1,3]\,U + SL\,[2,1]\,V + SL\,[3,1]\,W, \end{aligned} \tag{4.17a}$$

$$\begin{aligned} 0 = -PV + R\frac{\gamma}{3} &+ x\,[2,2]\,r_0 - SL\,[2,1]\,V \\ &- SL\,[2,3]\,V + SL\,[1,2]\,U + SL\,[3,2]\,W, \end{aligned} \tag{4.17b}$$

$$\begin{aligned} 0 = -PW + R\frac{\gamma}{3} &+ x\,[1,3]\,r_1 - SL\,[3,1]\,W \\ &- SL\,[3,2]\,W + SL\,[1,3]\,U + SL\,[2,3]\,V. \end{aligned} \tag{4.17c}$$

The $\omega_1 R$, $\omega_2 R$ and $\omega_3 R$ terms in equations 4.16a - 4.16c are added due to the fact that the oxygen can occupy a singlet excited state and decay to the triplet O_2 state. We assume that the exciton spin does not change in this step. The Si exciton states can decay back to their singlet ground state, thus, equation 4.14

needs to be added by term of $\omega_1 r_1 + \omega_2 r_0 + \omega_3 r_1$ as presented:

$$0 = \left(t\left[1,3\right]x\left[1,3\right] + t\left[2,2\right]x\left[2,2\right] + t\left[3,1\right]x\left[3,1\right]\right) - R\gamma + \omega_1 r_1 + \omega_2 r_0 + \omega_3 r_1. \tag{4.18}$$

Including additional new equations which contribute to the creation of exciton during the energy transfer:

$$0 = \frac{P\gamma}{3} - \omega_1 r_1 - \omega_1 R - \omega_1 sL\left[1,3\right] - \omega_1 sL\left[1,2\right] + \omega_2 sL\left[2,1\right] + \omega_3 sL\left[3,1\right], \tag{4.19}$$

$$0 = \frac{P\gamma}{3} - \omega_2 r_0 - \omega_2 R - \omega_2 sL\left[2,3\right] - \omega_2 sL\left[2,1\right] + \omega_3 sL\left[3,2\right] + \omega_1 sL\left[1,2\right], \tag{4.20}$$

$$0 = \frac{P\gamma}{3} - \omega_3 r_1 - \omega_3 R - \omega_3 sL\left[3,1\right] - \omega_3 sL\left[3,2\right] + \omega_1 sL\left[1,3\right] + \omega_2 sL\left[2,3\right]. \tag{4.21}$$

Finally, the total population would be

$$U + V + W + x\left[1,3\right] + x\left[2,2\right] + x\left[3,1\right] + \gamma + \omega_1 + \omega_2 + \omega_3 = 1. \tag{4.22}$$

However, as a result of various oxygen concentrations, we also can assume that some excitons may not be surrounded by O_2. Thus, the rate equations of these excitons are presented by

$$0 = \frac{Pn_0}{3} - \epsilon_1 r_1 - \epsilon_1 sL\left[1,3\right] - \epsilon_1 sL\left[1,2\right] + \epsilon_2 sL\left[2,1\right] + \epsilon_3 sL\left[3,1\right], \tag{4.23a}$$

$$0 = \frac{Pn_0}{3} - \epsilon_2 r_0 - \epsilon_2 sL\left[2,3\right] - \epsilon_2 sL\left[2,1\right] + \epsilon_1 sL\left[1,2\right] + \epsilon_3 sL\left[3,2\right], \tag{4.23b}$$

$$0 = \frac{Pn_0}{3} - \epsilon_3 r_1 - \epsilon_3 sL\left[3,1\right] - \epsilon_3 sL\left[3,2\right] + \epsilon_1 sL\left[1,3\right] + \epsilon_2 sL\left[2,3\right], \tag{4.23c}$$

where ϵ_1, ϵ_2 and ϵ_3 are excitons population in each exciton triple state of $|-1\rangle$, $|0\rangle$

and $|+1\rangle$, respectively. Consequently, the total population for the whole process, which is shown in equation 4.22, needs to include the non-enclosed excitons. Then, equation 4.22 is adapted into

$$U + V + W + x\,[1,3] + x\,[2,2] + x\,[3,1] + \gamma + \omega_1 + \omega_2 + \omega_3 + n_0 + \epsilon_1 + \epsilon_2 + \epsilon_3 = 1,$$

and

$$F + n_0 + \epsilon_1 + \epsilon_2 + _3 = 1,$$

where $F = U + V + W + x\,[1,3] + x\,[2,2] + x\,[3,1] + \gamma + \omega_1 + \omega_2 + \omega_3$. Therefore, if F is equal to 1, it means that the system contains only excitons with surrounding by adsorbed oxygen molecules.

The PL intensity (I_{PL}), which comes from the exciton decay, is given by

$$\begin{aligned} I_{PL} &= r_1 x\,[1,3] + r_0 x\,[2,2] + r_1 x\,[3,1] + r_1(\omega_1 + \omega_3) + r_0\omega_2 + r_1\epsilon_1 + r_0\epsilon_2 + r_1\epsilon_3 \\ &= r_1\,(x\,[1,3] + x\,[3,1] + \omega_1 + \omega_3 + \epsilon_1 + \epsilon_3) + r_0\,(x\,[2,2] + \omega_2 + \epsilon_2) \end{aligned} \quad (4.24)$$

4.5.2 Oxygen orientation aligned randomly with respect to the magnetic field

The last section described a set of rate equations which supposed that the spin states of the oxygen molecule is aligned along the magnetic field. Nevertheless, in general the orientation of the oxygen molecule will be aligned randomly with the B field. Let us define the B field along a z-direction at angle θ to the O_2 z-axis as shown in figure 4.20, causing the mixture of these spin states, thereby the new

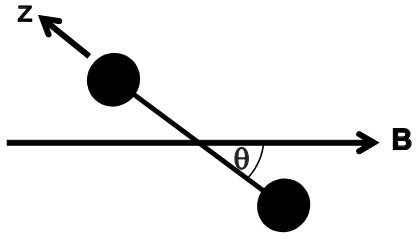

Figure 4.20: Oxygen molecule z-axis is aligned along the magnetic field with angle θ.

field direction is taken as the axis of quantisation. The spin Hamiltonian of the

triplet O_2 states in equation 4.4 is modified as

$$H_{O_2} = \begin{pmatrix} -G\mu_B B + \frac{D(3\cos^2\theta - 1)}{6} & \frac{D\sin\theta\cos\theta}{3\sqrt{2}} & \frac{D\sin^2\theta}{2} \\ \frac{D\sin\theta\cos\theta}{3\sqrt{2}} & \frac{D(1-3\cos^2\theta)}{3} & \frac{-D\sin\theta\cos\theta}{3\sqrt{2}} \\ \frac{D\sin^2\theta}{2} & \frac{-D\sin\theta\cos\theta}{3\sqrt{2}} & G\mu_B B + \frac{D(3\cos^2\theta - 1)}{6} \end{pmatrix}.$$

The eigenstates and their energies eigenvalues are quantised along the new z-axis and are mixed, therefore the strict selection rules of section 4.5.1 are relaxed. The mixing of these states is expressed as

$$\begin{aligned} \phi_1 &= a_{11}\left|-1\right\rangle + a_{21}\left|0\right\rangle + a_{31}\left|+1\right\rangle, \\ \phi_2 &= a_{12}\left|-1\right\rangle + a_{22}\left|0\right\rangle + a_{32}\left|+1\right\rangle, \\ \phi_3 &= a_{13}\left|-1\right\rangle + a_{23}\left|0\right\rangle + a_{33}\left|+1\right\rangle. \end{aligned} \tag{4.25}$$

$a_{k,l}$ is the coefficient of the oxygen spin Hamiltonian matrix with respect to the basis spin states $|-1\rangle$, $|0\rangle$ and $|+1\rangle$. The eigenstates and energies in equation 4.25 can be solved and obtained by numerical diagonalisation.

From Fermi's Golden Rule, the transfer coefficients ($t[i,j]$) need to be considered as follows: For transfer energy from the exciton spin state $|-1\rangle$, the transfer process must involve the O_2 spin state $|+1\rangle$. Hence, in O_2 eigenstate ϕ_1, the transfer coefficient $t[1,1]$ is proportional to the square of the coefficient of the O_2 spin state $|+1\rangle$ inside the eigenstate ϕ_1 as expressed

$$t\left[1,1\right] = a_{31}^2.$$

Similarly, in O_2 eigenstate ϕ_2, the transfer coefficient $t[1,2]$ is proportional to the square of the coefficient of the O_2 spin state $|+1\rangle$ inside the eigenstate ϕ_2 as shown

$$t\left[1,2\right] = a_{32}^2.$$

And there is repeatedly $t[1,3]$ with O_2 eigenstate ϕ_3.

For transfer energy from the exciton spin state $|0\rangle$, the transfer process must involve the O_2 spin state $|0\rangle$. Finally, transfer energy from the exciton spin state $|+1\rangle$, the transfer process must involve the O_2 spin state $|-1\rangle$. Eventually, the transfer rates are proportional to these squared coefficients multiplied by the

populations of the related paired states as illustrated,

$$\begin{aligned} t\,[1,1] &= a_{31}^2 \quad t\,[1,2] = a_{32}^2 \quad t\,[1,3] = a_{33}^2 \\ t\,[2,1] &= a_{21}^2 \quad t\,[2,2] = a_{22}^2 \quad t\,[2,3] = a_{23}^2 \\ t\,[3,1] &= a_{11}^2 \quad t\,[3,2] = a_{12}^2 \quad t\,[3,3] = a_{13}^2 \end{aligned} \tag{4.26}$$

The rate equations can be established and summarised in figure 4.21 showing the O_2 triplet ground states with U, V and W relative populations for $|-1\rangle$,

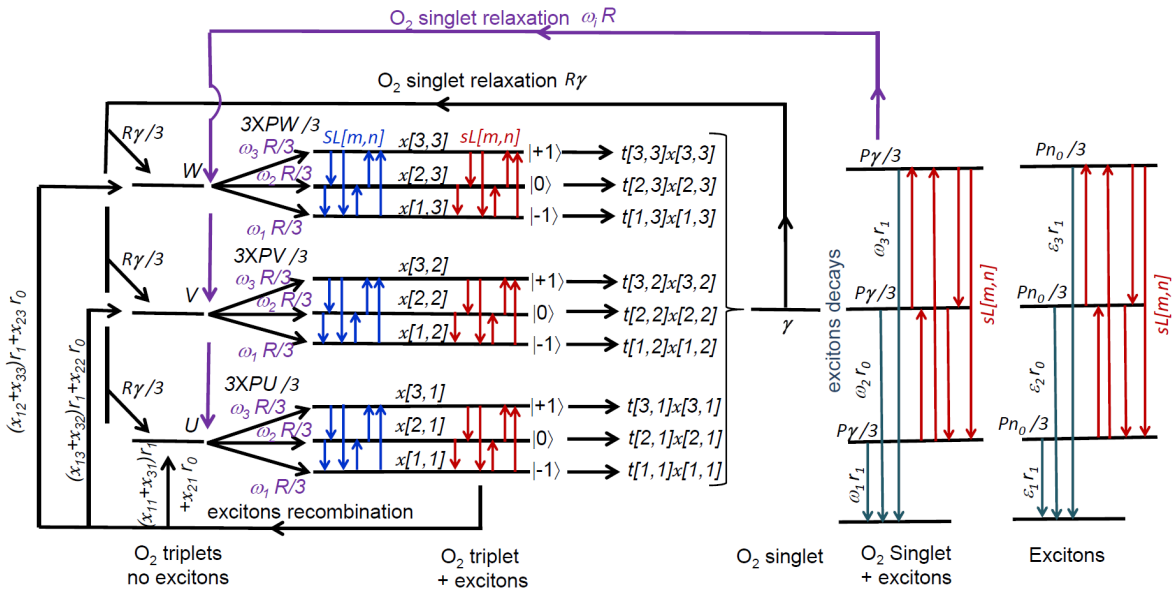

Figure 4.21: Energy transfer summary diagram between excitons and oxygen molecules.

$|0\rangle$ and $|+1\rangle$, respectively. When the magnetic field switches on, the mixtures of the O_2 spin states creates the new set of these states as shown in equation 4.25. With the exciton creation $x[i,j]$ by the constant pump rate P, the direct electron exchange coupling between these excitons and the O_2 states can occur and cause the energy transfer. During this step the spin-lattice relaxation also happens, either by the spin-flip of the exciton $sL[m,n]$ or by the spin-flip of the O_2 $SL[m,n]$ as represented by red and blue arrows, respectively. Together with these relaxations, the excitons also recombine through r_1 from the spin states $|+1\rangle$ and $|-1\rangle$ and r_0 from the spin states $|0\rangle$. The creation of singlet O_2 is governed by the transfer rates as shown in equation 4.26 and populated γ of $^1O_2$.

Meanwhile, $^1O_2$ can relax with the constant rate R. At this stage, the creation of the excitons still takes place with the population of ω_i, lead to the possibility of the exciton decay as presented by cyan arrows (see right hand side of figure

4.21. Together with these excitons, the surrounding $^1O_2$ decays back to the triplet ground states as represented by violet arrows. In the meantime, the spin-lattice relaxation of the excitons can happen throughout this stage. A detail of the rate equations will be shown in appendix B.

4.6 Fitting results

This section follows on from the previous section, which established the rate equations together with those of the spin Hamiltonians. We turn now to the experimental evidence on the energy transfer between Si exciton to molecular oxygen at various magnetic fields in order to examine the model. The PSi samples are divided into two groups based on their PL spectra shape in the presence of magnetic field and adsorbed O_2 as shown figure 4.22.

Figure 4.22(a) presents the PL spectra set (including sample numbers 30,34 and 701); even though the PL emissions originate from different samples, they have similar characteristics. The energy range covers from 1.3 to 2.4 eV. The phonon features also look alike, in particular below $^3\Sigma$ to $^1\Sigma$ of the energy transfer. In this case, the oxygen levels are comparable to the same high degree (although are not quantitative). The other set in figure 4.22(b) covers the energy of 1.4 to 2.6 eV. Unlike the sample set (a), PL intensities above the 1.63 eV threshold still show strong PL spectra and also emit different phonon patterns. The oxygen levels are comparatively high the same as the other set. There are sample number 350 and 2501 in this set. The samples details are described in appendix A.

4.6.1 Parameters for modeling

The key parameters for modeling can be listed as follows: 1) temperature (T); 2) pump power (P); 3) radiative recombination time of exciton spin states $|\pm1\rangle$ (τ_{r1}); 4) radiative recombination time of exciton spin state $|0\rangle$ (τ_{r0}); 5) exciton spin-lattice relaxation time (τ_w); 6) transfer time (τ_t); 7) radiative recombination time of O_2 (τ_R); 8) O_2 spin-lattice relaxation time (τ_W); and 9) ratio of O_2 to Si excitons populations (F). However, some parameters are not constant, depending on either energy and therefore on nanoparticle size or magnetic field

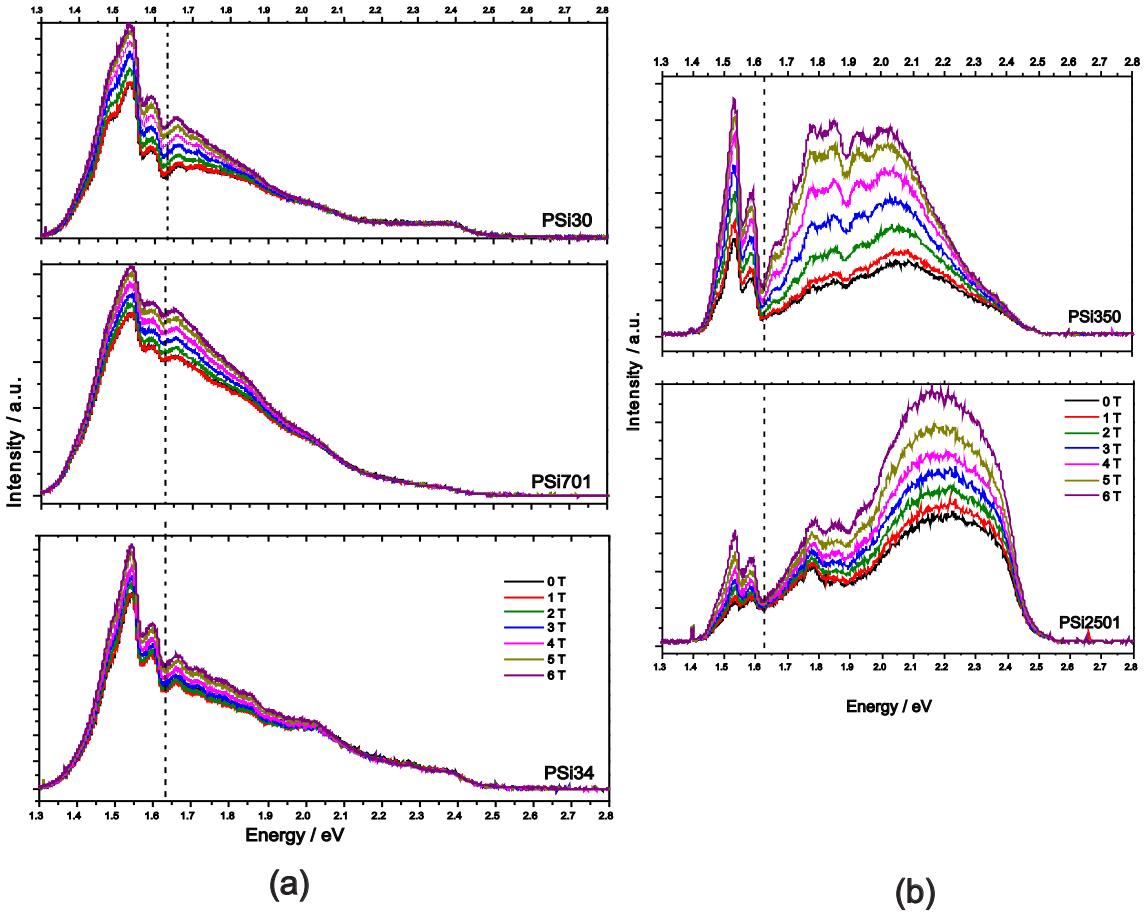

Figure 4.22: Selected PL spectra from PSi samples with adsorbed O_2 at different magnetic fields from 0 to 6 Tesla at T = 1.5 K with excitation energy 2.755 eV. The dashed line is the energy transition of O_2 between $^3\Sigma$ to $^1\Sigma$. (a) is a set of PL spectra from various PSi samples which emit PL spectra of similar shape at 44.8 mW/cm^2 excited power. (b) is the other set of PL spectra from different PSi samples that give another shape of PL spectra with the excited power of 23.9 to 39.8 mW/cm^2.

[26, 27, 28, 29, 30]. Temperature dependence is actually one of the most effective parameters which leads to the variation of several time factors [7, 31], nevertheless, all experimental results in this section are examined at liquid-He temperature. Hence, we can assume that the experimental temperature is fixed and equal to 1.5K.

There are published studies describing the dependence of the PSi exciton radiative decay rate on the size of quantum dot [7, 27, 28], together with the transfer rate depend on the shape of the this quantum dot [31]. As mentioned in section 4.6, the PSi samples are classified into two groups, thus we assume that intrinsic parameters of all samples in the same category should be similar. Finally, exter-

nal factors such as P and F are adjustable parameters due to the experimental conditions.

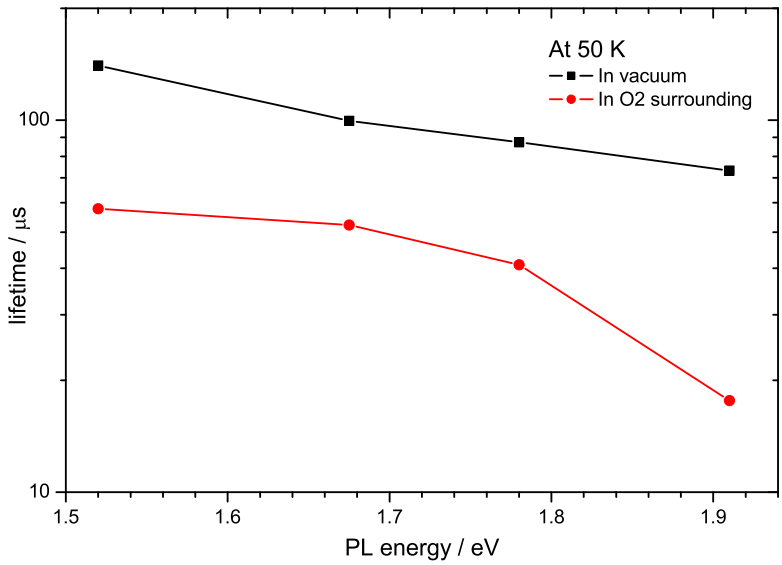

Figure 4.23: Si exciton decay time in vacuum and in the presence of oxygen molecules at T = 50 K.

From the frequency resolved measurements, figure 4.23 provides an estimated decay time in the presence of O_2, although the result is measured at elevated temperature. As commented before in chapter 2, the lifetime of nanocrystalline Si depends strongly on photon energy and temperature. In the absence of adsorbed O_2, the lifetime (represented by black line) is equal to the radiative lifetime of the excitons and is on the order of ms comparative with other reports [2, 6, 7]. Due to the energy transfer with O_2, a nonradiative decay channel occurs and leads to a significant decrease of the PL decay time as shown by red line in range of μs. So far this section has focused on the related parameters in order to achieve the fitting result in the following section.

4.6.2 Energy dependence

For the high level of O_2 adsorption as presented in figure 4.22, thus the ratio of O_2 to excitons populations F is set equal to 1 (defined in section 4.5.1). The individual group of the samples has a comparable P, therefore the two sets of

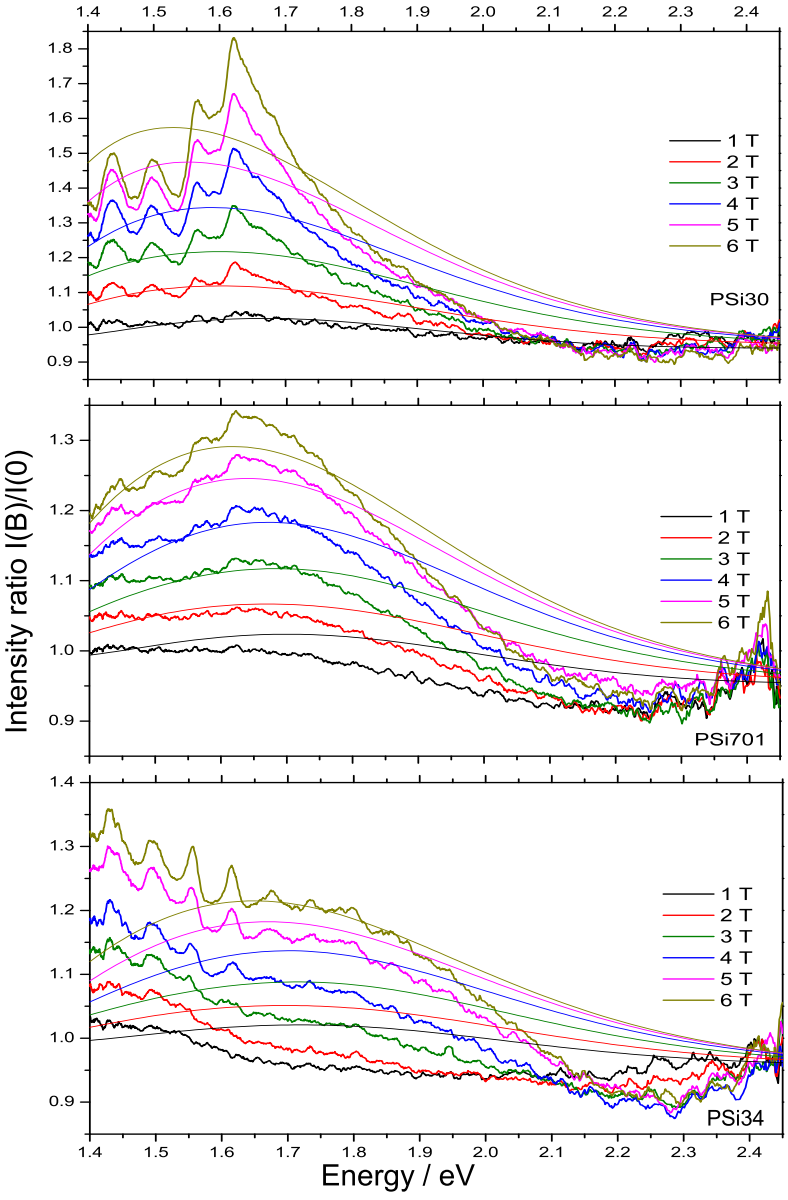

Figure 4.24: The intensity ratios I(B)/I(B=0 from the sample set (a) together with a fitting results from the parameter in equation 4.27.

parameters in equation 4.27 and 4.28, for the sample groups (a) and (b), respectively, can be tested for the intensity ratios I(B)/I(B=0) as displayed in figure 4.24 and 4.25

$$\begin{aligned} \tau_r = 55\,\mu s \quad \tau_{r0} = 5.5\,\mu s \quad \tau_w = 45\,\mu s \\ \tau_t = 0.75\,\mu s \quad \tau_R = 75\,ms \quad \tau_W = 40\,ms \quad \propto B^2. \end{aligned} \tag{4.27}$$

$$\begin{aligned} \tau_r = 60\,\mu s \quad \tau_{r0} = 0.35\,ms \quad \tau_w = 0.35\,\mu s \\ \tau_t = 0.75\,\mu s \quad \tau_R = 7.8\,ms \quad \tau_W = 70\,ms. \end{aligned} \tag{4.28}$$

Without adjusting any parameters except the excitation rate P, the simulations are created and shown via thin lines. For sample PSi30, the simulations seem to match well at low field (figure 4.24, top). On the contrary with PSi701 at high magnetic field, the fitting with the experimental data becomes better. For PSi34 (figure 4.24, bottom), at 6 Tesla the simulation matches well in the energy range of $\sim$ 1.6 - 1.9 eV, with magnetic fields reducing the fittings do not meet the results as good as at 6 Tesla. However, the fittings still give the right direction comparing with experimental outcomes.

Turning to figure 4.25, for PSi350 at low energy range, the fitting is better than higher energy range. In contrast to PSi350, the shape of the intensity ratio of PSi2501 is difficult to fit, however, the simulations still provide the right trend as shown in bottom of figure 4.25.

4.6.3 Magnetic field dependence

The effect of magnetic field on the energy transfer process is clearly seen by plotting the ratio between the PL intensities at certain magnetic fields I(B) and the PL intensities at zero field I(B=0) as a function of B field and at a specific PL energy of 1.63eV as demonstrated in figure 4.26. The magnetic field dependence calculation can be set up to obtain only one particular photon energy, so the figure 4.26 illustrates only the energy where the transfer between the Si excitons and molecular oxygens takes place. All parameters in these results are similar as equation 4.27 and 4.27. In sample set (a), the best result is the simulation of PSi701, nevertheless, the model can not recreate a situation where the PL

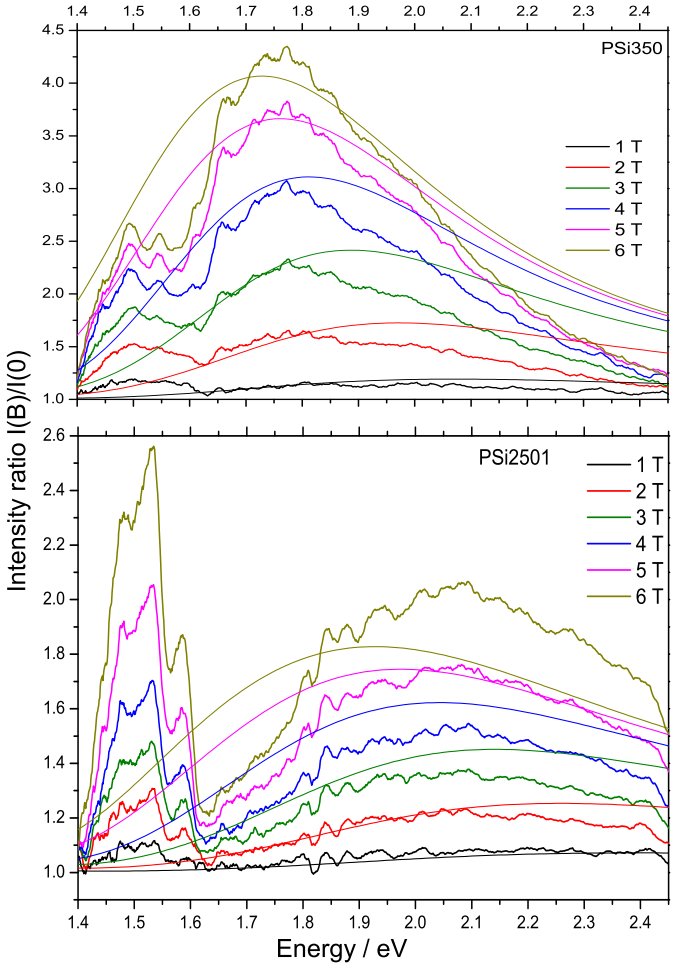

Figure 4.25: The intensity ratios I(B)/I(B=0) from the sample set (b) together with a fitting results from the parameter in equation 4.28.

intensity decreases at first as the field increases from zero. On the contrary, the simulated outcome of PSi30 shows these decreases, while for B above 2 T the match seems to fall off. For PSi34, the fit at the beginning of the field falls away but recovers to match at the high field.

The fit of sample set (b) provides a good simulation at the low fields, however, at fields higher than 3.5 T the fit starts to disagree with the experiments. Overall, the simulations still keep their tracks into the same direction as experimental results.

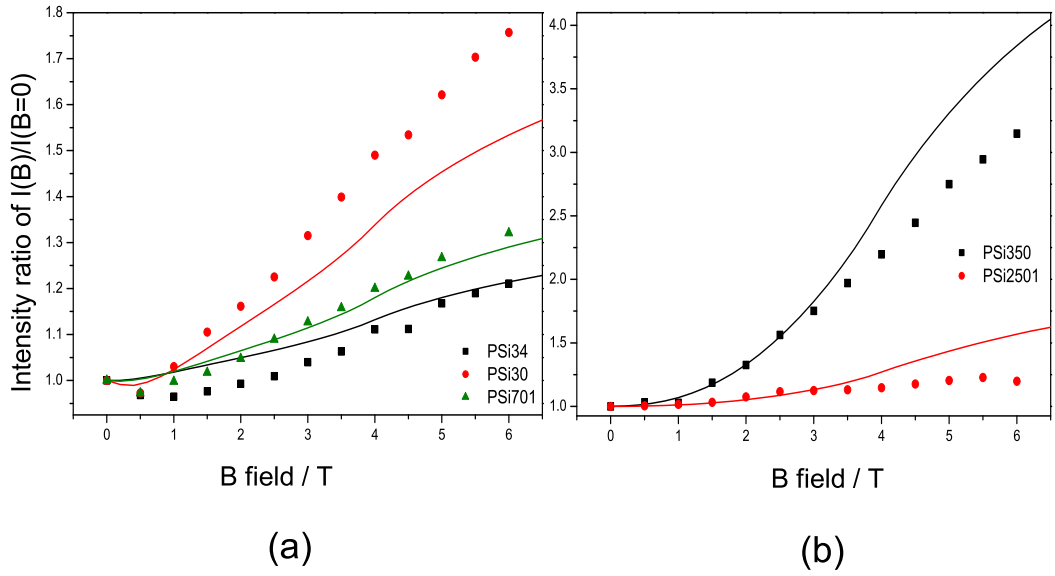

Figure 4.26: PL intensities ratio (I(B)/I(B=0)) as a function of magnetic fields at the $^3\Sigma$ to $^1\Sigma$ detection energy 1.63 eV. There are the experimental results of I(B)/I(B=0) of PSi30, PSi701 and PSi34 in (a). (b) is included the results of PSi350 and PSi2501. Dots and lines are represent the experimental data and simulate results, respectively.

4.6.4 Power dependence

To identify the power dependence effect, the variation of the excitation powers was used. The parameter set 1 in equation 4.27 is applied by keeping $F = 1$, and the only adjustable parameter is P. The experimental results and the simulations are included in figure 4.27. The maximum ratios of I(B)/I(B=0) at 0.3 mW is about 1.9, as a result of increasing field, at 3.0 mW the maximum ratio I(B)/I(B=0) rises up to 2.2. Finally, the last power excitation step is 16 mW, in contrast with the previous powers, the highest I(B)/I(B=0 ratio declines to around 1.8. These findings suggest that a saturation of the exciton population is probably the reason for this observation. Let turn our attention to the simulation; at low excited power the model produces reasonable results over the energies range, especially when compared to the highest power.

The intensity ratio I(B)/I(B=0) as a function of magnetic fields at energy of 1.63

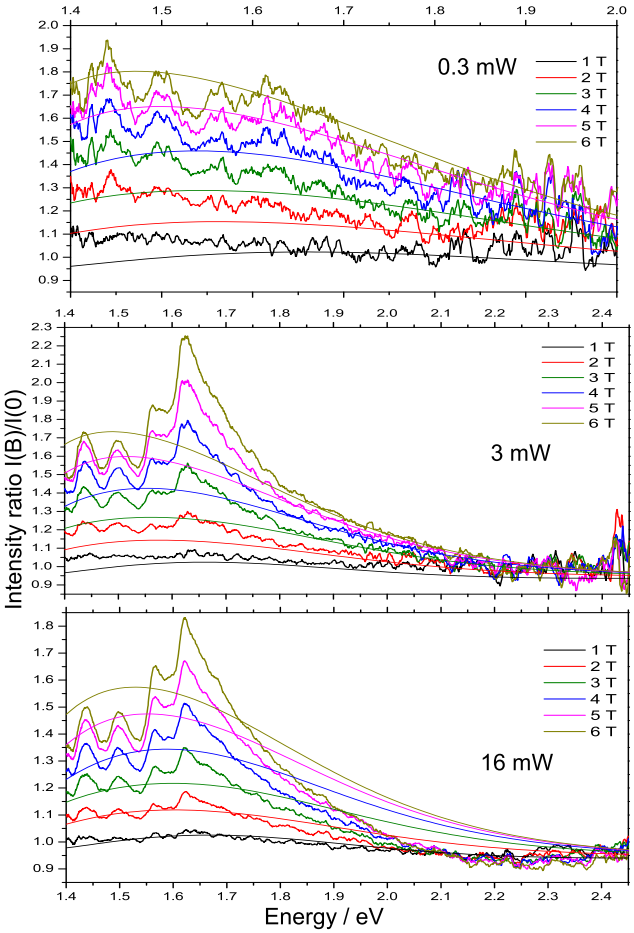

Figure 4.27: The intensity ratios I(B)/I(B=0) as a function of emission energy from the sample PSi30 with the different power excitation as 0.3 mW, 3.0 mW and 16.0 mW. The laser spot sizes are similar with the unfocused beams.

eV is presented in figure 4.28. Interestingly, the intensity ratio I(B)/I(B=0) < 1 at field below than 1 T is observed in all powers. In this case, the simulations produce good matches for all powers. Nevertheless, only the fitting of the lowest power generates the best fit over the fields range. The fitting results in the energy and the field dependence are pointed out in the same direction that, at the low excited power, our model seems to be supported by our experimental data.

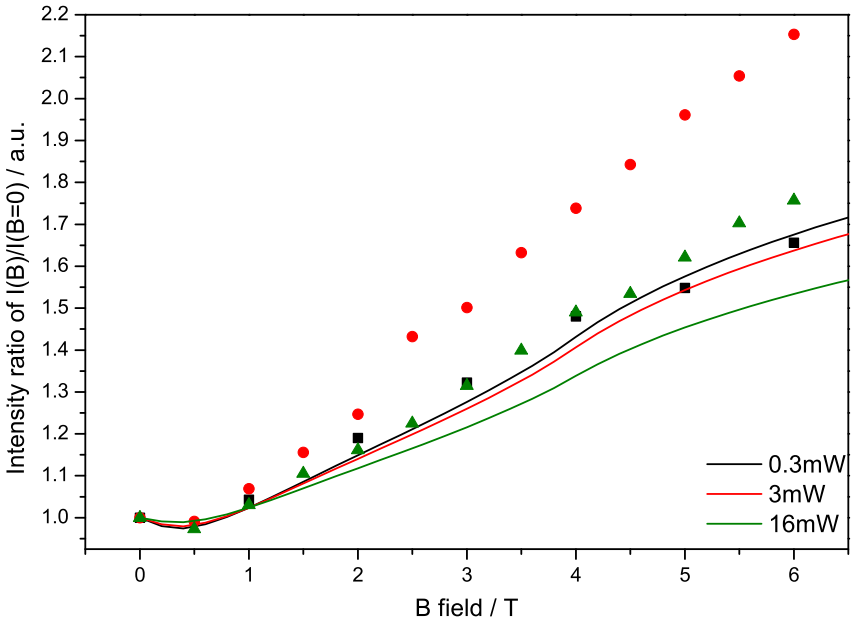

Figure 4.28: Field dependence of the intensity ratios I(B)/I(B=0) at energy of 1.63 eV with the dots are the experimental data and the lines are originated from simulated models.

4.6.5 O_2 concentration dependence

In order to investigate the O_2 concentration dependence in the energy transfer process with the magnetic field, the simulated parameter F needs to be varied. By keeping other parameters in equation 4.27 constant, the best simulation is obtain by setting $F = 0.6$ as illustrated in figure 4.29. It is clearly seen that at energies range below than 1.8 eV, the model gives reasonable results with the experimental data. However, above that energies range, the simulation seems to be unable to describe the behavior of the experimental results. Therefore, it is likely to claim that our model does not quite answer the situation where the system has low O_2 level. According to this, we might need to combine an empirical fit of the magnetic field dependence of nanoparticles without O_2 together with the model.

Considering, the ratio of PL intensity at various magnetic field I(B) and I(B=0) of the experimental system without O_2, the empirical PL intensity (I_{em}) is created by using a Gaussian function to simulate as shown in figure 4.30. As can be seen, the empirical fit provides the good fitting covered the energy range of 1.4

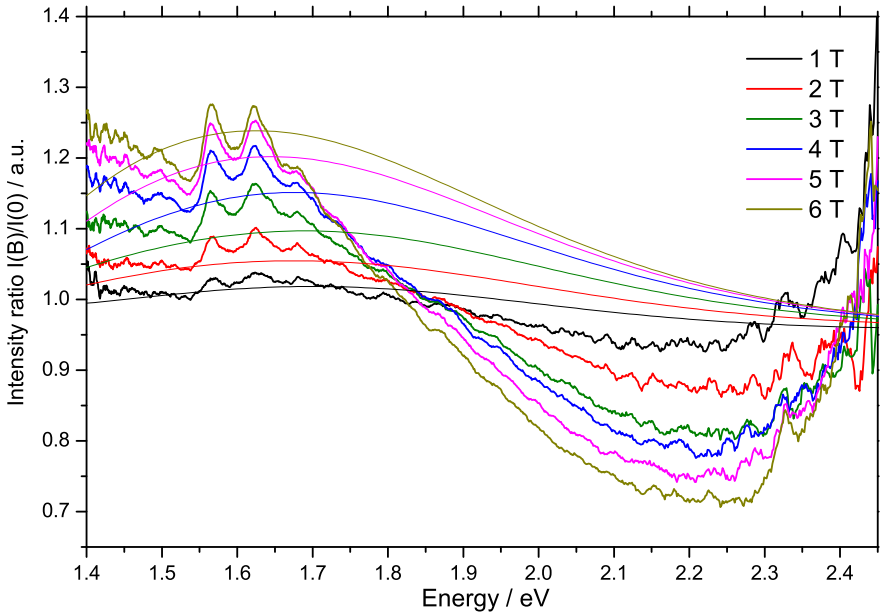

Figure 4.29: PL intensities ratio (I(B)/I(B=0)) as a function of emission energies for the case of low adsorbed O_2 level of PSi34.

to 2.05 eV. Above this energy range, the empirical result diverges apart from the experiment.

Finally, by including the empirical term for the absence O_2 situation, we can set up a formula as:

$$\frac{I(B)}{I(0)} = \frac{(1-\alpha)I_{fit}(B) + \alpha I_{em}(B)}{(1-\alpha)I_{fit}(0) + \alpha I_{em}(0)}, \tag{4.29}$$

where α is a fraction without O_2, $I_{fit}(B)$ is the simulation from our model at several fields and $I_{em}(B)$ is the empirical fit without O_2 at various fields. Therefore, in the absence of O_2 case α is equal to 1; on the other hand, α is equal to 0 in the presence of O_2.

Comparisons between the two different O_2 concentrations are made using equation 4.29. Figure 4.31 shows the results from the fitting model (the black smooth line) and the combination of the fitting model with the empirical $\alpha = 0.15$ (red line) compared with the experiments for high O_2 concentration. At low field such as B = 3T; the result (the red line) is improved by including the empirical fit, especially, when compared with the original model (the black line) as presented

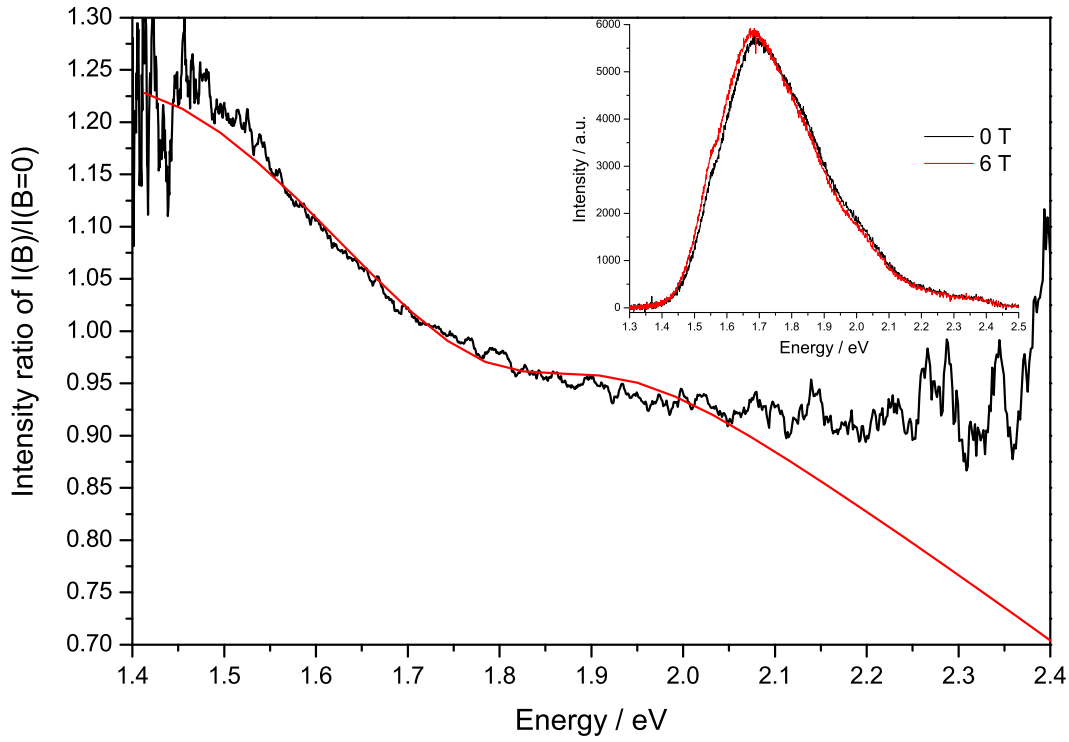

Figure 4.30: The empirical of intensity ratio I_{em}(B=6T)/I_{em}(B=0T) for PSi34 is presented by the red line. The black line is the experimental result of I(B=6T)/I(B=0). Inset is the PL spectra from PSi34 at 0 and 6 Tesla, presented by black and red lines, respectively, which are used to calculate the empirical fit. These results are observed and calculated from the absence of O_2 case.

in figure 4.31(a). On the other hand, although combining the empirical fit, the result at 6 T seems unachievable to get the good match with the experiment as shown in figure 4.31(b) .

Figure 4.32 displays the results from the fitting model (the black smooth line) and the combination of the fitting model with the empirical calculations at $\alpha = 0.97$ (red line) and $\alpha = 0.3$ (green line) compared with the experiments for low O_2 concentration. As presented in figure 4.32, although the fitting is not quite consistent, but overall the inclusion of the system without O_2 by using the empirical fit in equation 4.29 seems to be the right way to improve the fitting shape. Especially, at PL intensity ratio I(B)/I(B=0) less than 1, it is clear that the combination of empirical zero-O_2 case gives the ratio less than 1 figure. Therefore, our model needs zero-O_2 behaviour in order to achieve the better fit.

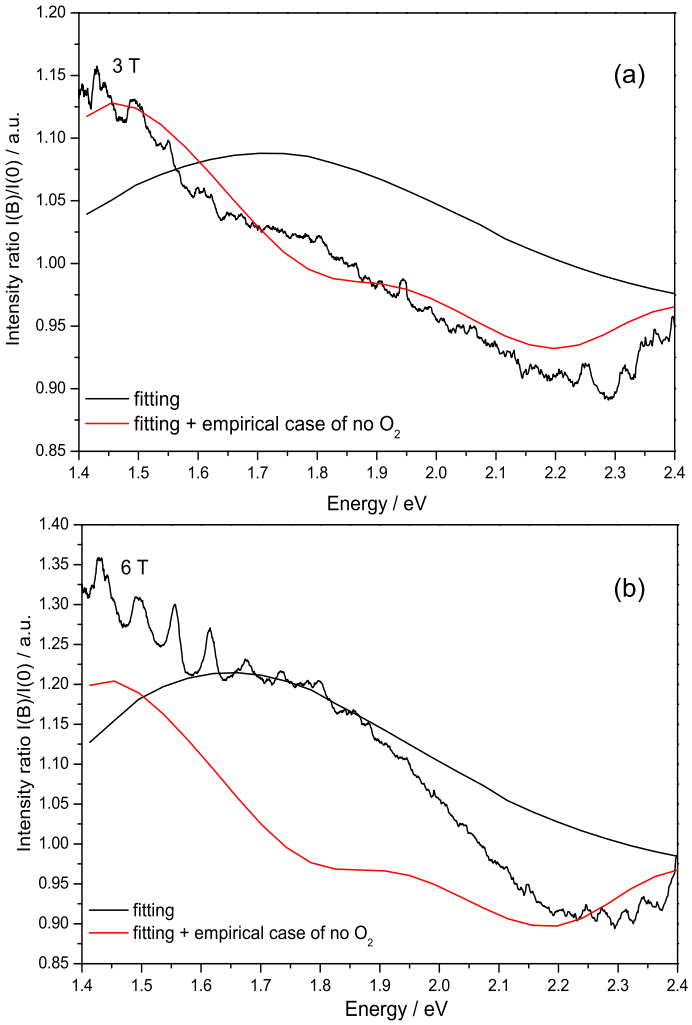

Figure 4.31: PL intensities ratio (I(B)/I(B=0)) as a function of emission energies for the case of high adsorbed O_2 level of PSi34. (a) is the result at 3 T. (b) is the result at 6 T. This fit uses $\alpha = 0.15$. The black and red smooth lines are the original fitting model and the including of the empirical calculation with the original model, respectively.

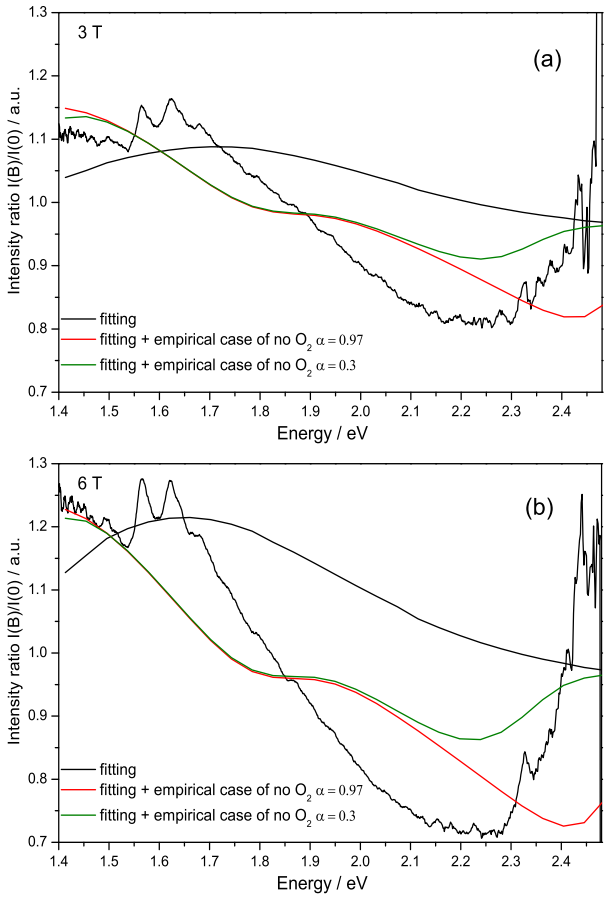

Figure 4.32: PL intensities ratio (I(B)/I(B=0)) as a function of emission energies for the case of low adsorbed O_2 level of PSi34. (a) shows the result at 3 T. (b) shows the result at 6 T. This fit uses $\alpha = 0.97$ and $\alpha = 0.3$ for comparison. The black, red and green smooth lines are the original fitting model, the including of the empirical calculation at $\alpha = 0.97$ with the original model and the including of the empirical calculation at $\alpha = 0.3$ with the original model, respectively.

4.7 Conclusion

This chapter has examined the energy transfer mechanism between the nanostructured Si and O_2. The significant suppression of PL over 1.63 eV shows evidence of the singlet oxygen $^1O_2$ creation. The experimental results reveal phonon replica features together with the production of $^1O_2$. The effects of magnetic field, power and O_1 concentration on the energy transfer process were studied as a function of PL energy dependence. The energy transfer model is set up and applied to simulate the experimental data. Although the model is incomplete for the case of the absence of O_2, overall, the simulations are in good agreement with the experimental results. The parameters obtained from the simulations will be explained and discussed in more details in chapter 5.

References

[1] D. Kovalev, E. Gross, N. Künzner, F. Koch, V. Yu. Timoshenko, and M. Fujii. Resonant electronic energy transfer from excitons confined in silicon nanocrystals to oxygen molecules. *Physical Review Letters*, 89:137401, 2002.

[2] E. Gross, D. Kovalev, N. Kunzner, J. Diener, F. Koch, V. Y. Timoshenko, and M. Fujii. Spectrally resolved electronic energy transfer from silicon nanocrystals to molecular oxygen mediated by direct electron exchange. *Physical Review B*, 68(11), 2003.

[3] N. J. Turro, V. Ramamurthy, and J. C. Scaiano. *Modern molecular photochemistry of organic molecules*. Sausalito, Calif. : University Science, 2010.

[4] C. Schweitzer and R. Schmidt. Physical mechanisms of generation and deactivation of singlet oxygen. *Chemical Reviews*, 103(5):1685–1757, 2003.

[5] R. Schmidt. Influence of Heavy Atoms on the Deactivation of Singlet Oxygen ($^1\Delta_g$) in Solution. *Journal of the American Chemical Society*, 111(18):6983–6987, 1989.

[6] P. D. J. Calcott, K. J. Nash, L. T. Canham, M. J. Kane, and D. Brumhead. Identification of radiative transitions in highly porous silicon. *Journal of Physics-Condensed Matter*, 5(7):L91–L98, 1993.

[7] A. G. Cullis, L. T. Canham, and P. D. J. Calcott. The structural and luminescence properties of porous silicon. *Journal of Applied Physics*, 82(3), 1997.

[8] D Kovalev, H Heckler, B Averboukh, M Ben-Chorin, M Schwartzkopff, and F Koch. Hole burning spectroscopy of porous silicon. *Physical Review B*, 57(7):3741–3744, 1998.

[9] D. Kovalev and M. Fujii. Silicon nanocrystals: Photosensitizers for oxygen molecules. *Advanced Materials*, 17(21):2531–2544, 2005.

[10] W. Weber. Adiabatic Bond Charge Model for Phonons in Diamond, Si, Ge, and α-Sn. *Physical Review B*, 15(10):4789–4803, 1977.

[11] D. Kovalev, H. Heckler, M. Ben-Chorin, G. Polisski, M. Schwartzkopff, and F. Koch. Breakdown of the k-conservation rule in Si nanocrystals. *Physical Review Letters*, 81(13):2803–2806, 1998.

[12] J. Linnros, N. Lalic, A. Galeckas, and V. Grivickas. Analysis of the stretched exponential photoluminescence decay from nanometer-sized silicon crystals in sio$_2$. *Journal of Applied Physics*, 86(11):6128–6134, 1999.

[13] V. Vinciguerra, G. Franzo, F. Priolo, F. Iacona, and C. Spinella. Quantum confinement and recombination dynamics in silicon nanocrystals embedded in Si/SiO_2 superlattices. *Journal of Applied Physics*, 87(11):8165–8173, 2000.

[14] C. Garcia, B. Garrido, P. Pellegrino, R. Ferre, J. A. Moreno, J. R. Morante, L. Pavesi, and M. Cazzanelli. Size dependence of lifetime and absorption cross section of Si nanocrystals embedded in SiO_2. *Applied Physics Letters*, 82(10):1595–1597, 2003.

[15] M. Koós, I. Pócsik, and É. Vázsonyi. Experimental proof for nanoparticle origin of photoluminescence in porous silicon layers. *Applied Physics Letters*, 62(15):1797–1799, 1993.

[16] K. J. Nash, P. D. J. Calcott, L. T. Canham, and R. J. Needs. Spin-orbit interaction, triplet lifetime, and fine-structure splitting of exctions in highly porous silicon. *Physical Review B*, 51(24):17698–17707, 1995.

[17] Brandt M. S. and Stutzmann M. Triplet excitons in porous silicon and siloxene. *Solid State Communications*, 93(6):473 – 477, 1995.

[18] B. Goller, S. Polisski, and D. Kovalev. Spin-flip excitation of molecules mediated by photoexcited silicon nanocrystals. *Physical Review B*, 75(7), 2007.

[19] L. A. Pardi, J. Krzystek, J. Telser, and L. Brunel. Multifrequency epr spectra of molecular oxygen in solid air. *Journal of Magnetic Resonance*, 146(2):375 – 378, 2000.

[20] D. J. Dunstan and J. J. Davies. The behaviour of donor-acceptor recombination emission in II-VI crystals subjected to magnetic resonance. *Journal of Physics C-Solid State Physics*, 12(14):2927–2944, 1979.

[21] F. A. Reboredo, A. Franceschetti, and A. Zunger. Dark excitons due to direct Coulomb interactions in silicon quantum dots. *Physical Review B*, 61(19):13073–13087, 2000.

[22] S. Lttjohann, C. Meier, M. Offer, A. Lorke, and H. Wiggers. Temperature-induced crossover between bright and dark exciton emission in silicon nanoparticles. *EPL*, 79(3), 2007.

[23] C. Meier, S. Luettjohann, M. Offer, H. Wiggers, and A. Lorke. Silicon Nanoparticles: Excitonic Fine Structure and Oscillator Strength. In Haug, R., editor, *Advances in Solid State Physics, Vol 48*, volume 48 of *Advances in Solid State Physics*, pages 79–90, 2009.

[24] J. Diener, D. Kovalev, H. Heckler, G. Polisski, and F. Koch. Exciton states of silicon nanocrystals studied by magneto-optical spectral hole burning. *Physical Review B*, 63:073302, 2001.

[25] H. Heckler, D. Kovalev, G. Polisski, N. N. Zinov'ev, and F. Koch. Magneto-optical effects in photoluminescence of Si nanocrystals. *Physical Review B*, 60(11):7718–7721, 1999.

[26] C. Delerue, G. Allan, and M. Lannoo. Theoretical aspects of the luminescence of porous silicon. *Physical Review B*, 48:11024–11036, 1993.

[27] F. Huisken, G. Ledoux, O. Guillois, and C. Reynaud. Light-emitting silicon nanocrystals from laser pyrolysis. *Advanced Materials*, 14(24):1861–1865, 2002.

[28] V. A. Belyakov, V. A. Burdov, R. Lockwood, and A. Meldrum. Silicon nanocrystals: fundamental theory and implications for stimulated emission. *Advances in Optical Technologies*, 2008:1–32, 2008.

[29] E. G. Barbagiovanni, D. J. Lockwood, P. J. Simpson, and L. V. Goncharova. Quantum confinement in si and ge nanostructures. *Journal of Applied Physics*, 111(3):034307–1–034307–9, 2012.

[30] F. A. Zwanenburg, A. S. Dzurak, A. Morello, M. Y. Simmons, L. C. L. Hollenberg, G. Klimeck, S. Rogge, S. N. Coppersmith, and M. A. Eriksson.

Silicon quantum electronics. *Reviews of Modern Physics*, 85(3):961–1019, 2013.

[31] M. Fujii, D. Kovalev, B. Goller, S. Minobe, S. Hayashi, and V. Y. Timoshenko. Time-resolved photoluminescence studies of the energy transfer from excitons confined in Si nanocrystals to oxygen molecules. *Physical Review B*, 72(16), 2005.

Chapter 5

Conclusion

The development of nano-technology exploits the properties and functionalities of nanoscale materials including nanocrystalline Si. The spin structures and the exchange mechanisms are key features which establish Si nanocrystals as facilitators for the photoexcitation of adsorbed molecules discussed throughout this thesis. This chapter presents an overview of the major findings from the previous chapters and discusses the main objectives of this study. Finally, an outlook for the continuation of this work in the future is also provided.

5.1 Investigation of the energy transfer process

From the previous chapter, it can be seen that the parameters provided simulate the behaviour of several samples over a wide energy range. The fitting parameters are summarised and presented in table 5.1 including theoretical and experimental data from other studies. However, these modeling outcomes are calculated at a fixed energy of 1.63 eV ($^3\Sigma$ - $^1\Sigma$). The comparison between two sets of parameters shows two different variables; the radiative lifetime of excitons from r_0 state (τ_{r0}) and and the spin lattice relaxation of excitons (τ_w). Other variables are in similar ranges. Obviously, these differences reveal that samples in group I have an average particle size smaller than samples in group II. As shown in table 5.1, the lifetime τ_{r0} from samples in set I is shorter than that of samples in set II which implies that the overall size of Si nanocrystals in the set I samples is smaller than the

Table 5.1: Summary of the modeling parameters for the energy transfer process compared with other reports.

Model			Other reports	Notes /
Parameters	**set I**	**set II**		**reference**
τ_r	55 μs	60 μs	10 μs $< \tau <$ 10 ms	with phonon [3]
τ_{r0}	5.5 μs	350 μs	$\tau >$ 1 ms	without phonon [3]
			$\sim$ 2-15 μ s	T_{room} [4]
			$\sim$ 2-6 ms	T = 1-25 K [4]
			$\sim$ 8-300 μs	T_{room} [5]
			$\sim$ 200 μs	T = 5 K [6]
τ_w	45 μs	0.35 μs	$\sim$ 2.8 s and $\tau_{S/T} \sim$ 10 ms	[1]
			13.8 ms	[2]
τ_t	0.75 μs	0.75 μs	$\tau_{Si\rightarrow\Sigma} \sim$ 2.56 μs	T = 5 K [7]
			$\tau_{Si\rightarrow\Delta} \sim$ 300 μs	$T_{cryogenic}$ [7]
τ_R	75 ms	7.8 ms	$\tau_{1\Delta}$ = 46 μs	T = 77K [8]
			$\tau_{1\Sigma}$ = 24 μs	T = 77K [8]
τ_W	40 ms	70 ms		set I: $\tau_W \propto B^2$

Note: Parameters depend strongly on the size, fabrication procedures of Si nanocrystals and temperatures .

set II samples. The other variable also confirms this implication as the spin-lattice relaxation time τ_w of the set I is longer than τ_w of the set II. Due to the decreasing size of Si nanostructures, the exciton-phonon interaction is less efficient, therefore, the spin-lattice relaxation time increases [1, 2].

The evidence from SEM images supports this finding as presented in figure 5.1; (a) the top view image of sample PSi30 (set I) compares with sample PSi350 (set II) and (b) the cross section image of sample PSi30 (set I) compares with sample PSi350 (set II). This figure is quite revealing in several ways. First, the top view image of the sample set I shows clear separate particles which have diameters in a range less than 100 nm, in contrast with the sample set II for which the particles look more compact and it is difficult to estimate the size. Second, the pore structures of set I can be seen; on the contrary, the pores of set II are indistinct. Lastly, a characteristic "fir tree" structure and the pore branches are clearly indicated in cleaved cross sections of the set I, again in contrast with

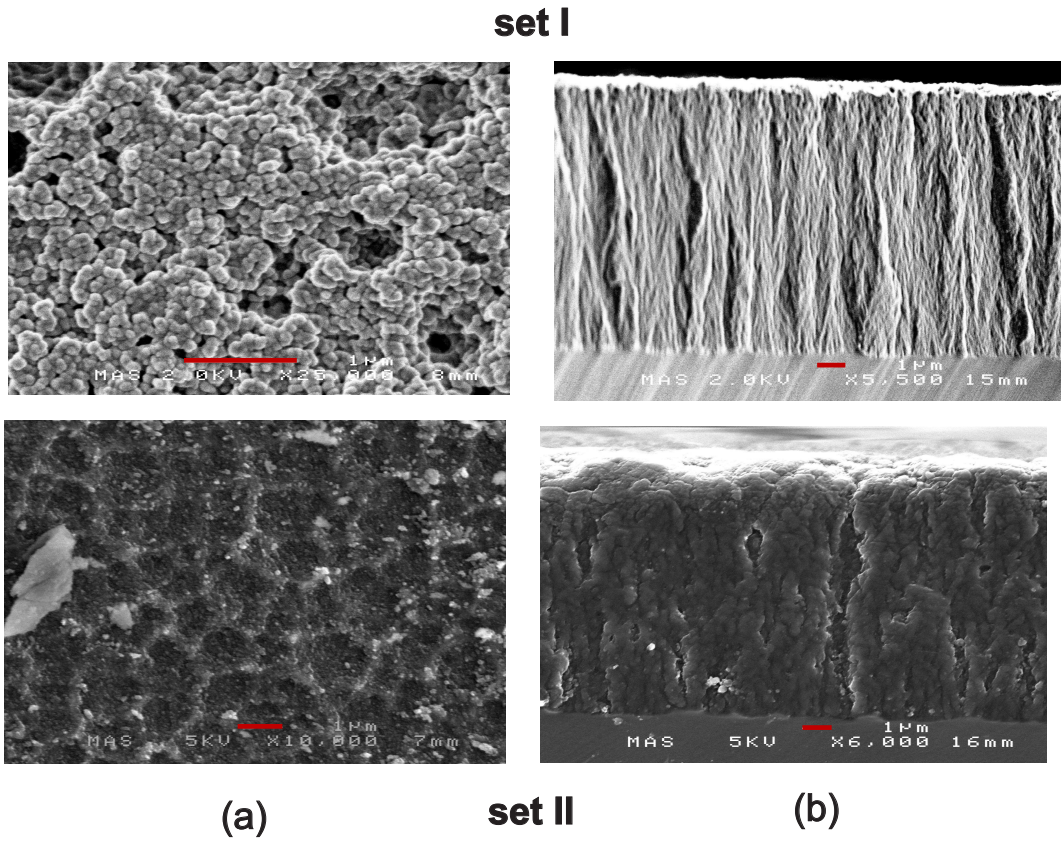

Figure 5.1: Comparison of SEM images between sample set I and sample set II. The scale bars are equal to 1 μm.

the sample set II. The SEM images of PSi set II may also give an explanation of the PL intensity shape from the samples (set II), owing to the fact that Si nanostructures are compact and have fewer pores, thus, oxygen molecules seem to have less access throughout the particles. This is probably the reason why, above 1.63 eV, the PL intensity of samples set II still appeared significant even for high O_2 concentrations. Other samples in these sets also give similar SEM images. Consequently, the model can reveal some significant properties of Si nanocrystals through the fitting parameters.

The comparison between the simulated parameters and other studies is also displayed in table 5.1. Although, some fitting parameters differ from other reports, they are in the same ranges, particularly, the radiative lifetime of Si nanoparticles. Likewise, as mentioned before these parameters depend strongly on the size, fabrication procedures of Si nanocrystals and temperatures but the model can set up the fitting calculation based on only one particular energy, which is energy of 1.63 eV in this case.

5.2 Overall summary

The main purpose of the current work was to investigate the spin dependent interactions of oxygen molecules on nanocrystalline Si, in order to understand and model the energy transfer mechanism. Chapter 1 gave the brief background of bulk crystalline Si and introduced Si nanostructures as the consequence of quantum confinement. Their excitonic spin states were explained including the unique ground triplet state of molecular oxygens. Criteria for photosensitiser candidates were discussed, together with the potential of nanostructured Si as a photosensitising agent.

Chapter 2 described the fabrication procedure of PSi which was studied through out this thesis. Several experimental measurements were used to study PSi samples in order to obtain physical and chemical characterisations along with optical and dynamic properties. Due to the preparation method, the Si nanoparticles formed as interconnected particles (PSi). Initially, PSi surfaces were hydride-terminated which are very reactive and susceptible to air oxidation. Confinement of excitons in Si nanoparticles caused the radiative recombination of excitons to become more efficient than the bulk Si.

Chapter 3 proposed the incorporation of Si nanoparticles into the silica aerogel by using typical aerogel synthesis. Various sizes and terminated surfaces of nanostructured Si were introduced to created Si-silica aerogel composites. However, the composites aerogel of hydride-terminated surfaces was oxidised and left only the solid crystalline Si. On the contrary, the porous structures of the composites aerogel containing oxide-termination persisted, even though insensitive to adsorbed molecular oxygen. Somehow, the chemical procedure of the aerogel composites preparation eliminated the energy transfer ability between Si nanocrystals and oxygen molecules.

Chapter 4 studied the energy transfer mechanism by magneto-optical measurements. The photoexcitation of Si nanostructures transfered energy to oxygen molecules as shown by the strong suppression of the PL of nanocrystalline Si above 1.63 eV corresponding with the $^3\Sigma$ to $^1\Sigma$ transition. The phonon features were demonstrated together with the creation of the $^1O_2$. The key feature to achieve the photoexcitation of oxygen molecules is the role of spin exchange between excitons and the absorbed oxygen molecules. The energy transfer model

was established, based upon the fact that the exchange-mediated energy transfer occurs only via the spin conserving transitions. When a magnetic field was applied, the effects of O_2 concentrations, powers and size distributions (detection energies) on the energy transfer process could be examined. The model produced simulations which are in good agreement with the experimental data. Dynamic parameter values were delivered. However, the model is limited by the energy dependence calculation and the lack of information on the magnetic field dependence of Si nanoparticles in the absence of oxygen behaviour.

5.3 Suggested work

Currently, the model determined the results based on a fixed energy. Nevertheless, several parameters such as lifetime and so on are energy dependence (size dependence). Our current study derives from PSi samples which, normally, have wide size distributions. Hence, it would be interesting to measure and to simulate the energy transfer process of Si nanoparticles which have similar particle sizes by the proposed model.

A further study investigating two-photon excitation of nanostructured Si would be very interesting. This research would give an opportunity to understand dipole allowed and forbidden optical transitions in Si nanocrystals by selection rules [9]. Furthermore, the energy transfer to O_2 in this case could be considered.

Further work on nano-silicon containing both aromatic molecules such as fullerene and O_2 may extend the concept of the energy transfer in organic photochemistry. The potential applications are extensive, from photochemical reactions to photodynamic therapy.

References

[1] F. A. Zwanenburg, A. S. Dzurak, A. Morello, M. Y. Simmons, L. C. L. Hollenberg, G. Klimeck, S. Rogge, S. N. Coppersmith, and M. A. Eriksson. Silicon quantum electronics. *Reviews of Modern Physics*, 85(3):961–1019, 2013.

[2] E. A. Konstantinova, V. A. Demin, and V. Y. Timoshenko. Investigation of the generation of singlet oxygen in ensembles of photoexcited silicon nanocrystals by electron paramagnetic resonance spectroscopy. *Journal of Experimental and Theoretical Physics*, 107(3):473–481, 2008.

[3] V. A. Belyakov, V. A. Burdov, R. Lockwood, and A. Meldrum. Silicon nanocrystals: fundamental theory and implications for stimulated emission. *Advances in Optical Technologies*, 2008:1–32, 2008.

[4] A. G. Cullis, L. T. Canham, and P. D. J. Calcott. The structural and luminescence properties of porous silicon. *Journal of Applied Physics*, 82(3), 1997.

[5] F. Huisken, G. Ledoux, O. Guillois, and C. Reynaud. Light-emitting silicon nanocrystals from laser pyrolysis. *Advanced Materials*, 14(24):1861–1865, 2002.

[6] S. Lttjohann, C. Meier, M. Offer, A. Lorke, and H. Wiggers. Temperature-induced crossover between bright and dark exciton emission in silicon nanoparticles. *EPL*, 79(3), 2007.

[7] M. Fujii, D. Kovalev, B. Goller, S. Minobe, S. Hayashi, and V. Y. Timoshenko. Time-resolved photoluminescence studies of the energy transfer from excitons confined in Si nanocrystals to oxygen molecules. *Physical Review B*, 72(16), 2005.

[8] S. Jockusch, N. J. Turro, E. K. Thompson, M. Gouterman, J. B. Callis, and

G.l E. Khalil. Singlet molecular oxygen by direct excitation. *Photochmical & Photobiological Sciences*, 7(2):235–239, 2008.

[9] J. Diener, D. I. Kovalev, G. Polisski, and F. Koch. Resonant two-photon excitation of silicon nanocrystals. *Applied Physics Letters*, 74(22):3350–3352, 1999.

Appendix A

Sample details

All porous silicon samples used in this thesis were fabricated by electrochemical etching of p-type crystalline silicon (100) in a 1:1 (by volume) of 49% aqueous hydrofluoric acid (HF) : ethanol solution. Preparation conditions of sample are given in table A.1, along with the porosity details.

Table A.1: Samples examined in this thesis. The growing conditions and porosities are given.

sample no.	**Resistivity**	**Current density**	**time**	**Porosity**
	Ω·cm	mA/cm^2	min	%
30	1-10	22.02	10	67.1
34	1-10	36.71	6	49.4
701	10-20	9.96	10	34.8
703	10-20	17.74	12	86.4
2501	1-10	37.90	6	82.4
2505	1-10	35.26	6	81.1
2506	1-10	26.44	8	82.2
2507	1-10	30.85	6	69.7
2508	1-10	22.92	8	69.3
350	10-20	30.85	6	-

Appendix B

Rate equation

As discussed in chapter 4.5.2, the rate equations can be established and summarised in figure 4.21. A full set of rate equations of the model of the energy

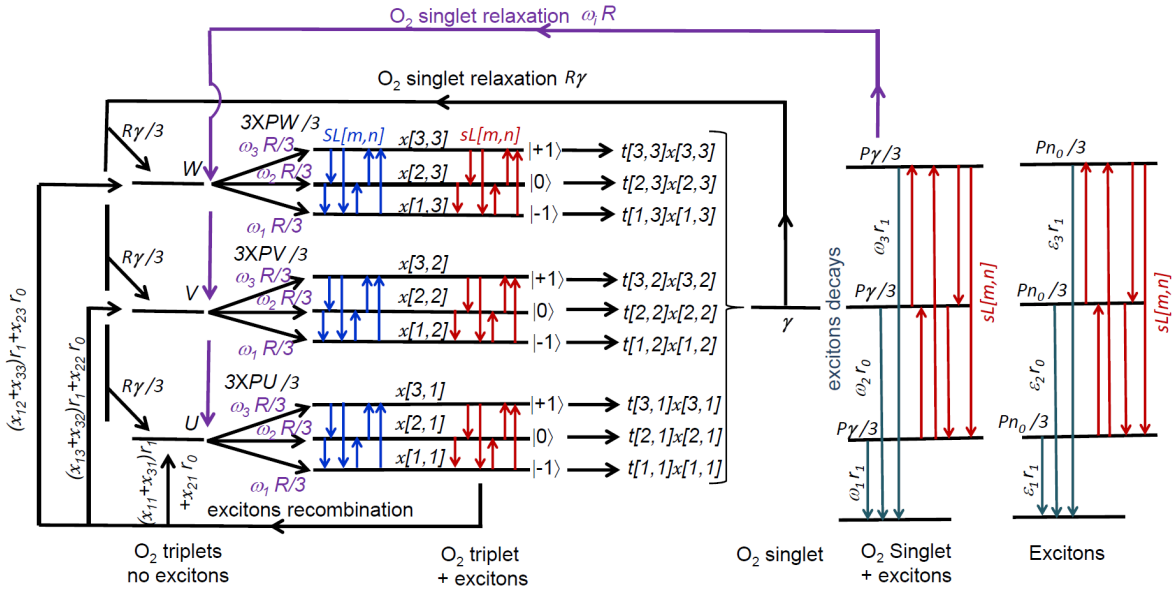

Figure B.1: Energy transfer summary diagram between excitons and oxygen molecules.

transfer between nanostructured Si and molecular oxygen, when the orientation of the O_2 is aligned randomly with the B field, can be presented as follows:

$$0 = PU/3 - x\,[1,1]\,(r_1 + t\,[1,1] + sL\,[1,2] + sL\,[1,3] + SL\,[1,2] + SL\,[1,3])$$
$$+ sL\,[2,1]\,x\,[2,1] + sL\,[3,1]\,x\,[3,1] + SL\,[2,1]\,x\,[1,2] + SL\,[3,1]\,x\,[1,3] + \omega_1 R/3, \tag{B.1a}$$

$$0 = PU/3 - x\,[3,1]\,(r_1 + t\,[3,1] + sL\,[3,1] + sL\,[3,2] + SL\,[1,2] + SL\,[1,3])$$
$$+ sL\,[1,3]\,x\,[1,1] + sL\,[2,3]\,x\,[2,1] + SL\,[3,1]\,x\,[3,3] + SL\,[2,1]\,x\,[3,2] + \omega_3 R/3, \tag{B.1b}$$

$$0 = PU/3 - x\,[2,1]\,(r_0 + t\,[2,1] + sL\,[2,1] + sL\,[2,3] + SL\,[1,2] + SL\,[1,3])$$
$$+ sL\,[1,2]\,x\,[1,1] + sL\,[3,2]\,x\,[3,1] + SL\,[3,1]\,x\,[2,3] + SL\,[2,1]\,x\,[2,2] + \omega_2 R/3. \tag{B.1c}$$

$$0 = PV/3 - x\,[1,2]\,(r_1 + t\,[1,2] + sL\,[1,2] + sL\,[1,3] + SL\,[2,1] + SL\,[2,3])$$
$$+ sL\,[2,1]\,x\,[2,2] + sL\,[3,1]\,x\,[3,2] + SL\,[1,2]\,x\,[1,1] + SL\,[3,2]\,x\,[1,3] + \omega_1 R/3, \tag{B.2a}$$

$$0 = PV/3 - x\,[2,2]\,(r_0 + t\,[2,2] + sL\,[2,1] + sL\,[2,3] + SL\,[2,1] + SL\,[2,3])$$
$$+ sL\,[1,2]\,x\,[1,2] + sL\,[3,2]\,x\,[3,2] + SL\,[1,2]\,x\,[2,1] + SL\,[3,2]\,x\,[2,3] + \omega_2 R/3, \tag{B.2b}$$

$$0 = PV/3 - x\,[3,2]\,(r_1 + t\,[3,2] + sL\,[3,1] + sL\,[3,2] + SL\,[2,1] + SL\,[2,3])$$
$$+ sL\,[1,3]\,x\,[1,2] + sL\,[2,3]\,x\,[2,2] + SL\,[1,2]\,x\,[3,1] + SL\,[3,2]\,x\,[3,3] + \omega_3 R/3. \tag{B.2c}$$

$$0 = PW/3 - x\,[1,3]\,(r_1 + t\,[1,3] + sL\,[1,2] + sL\,[1,3] + SL\,[3,1] + SL\,[3,2])$$
$$+ sL\,[2,1]\,x\,[2,3] + sL\,[3,1]\,x\,[3,3] + SL\,[1,3]\,x\,[1,1] + SL\,[2,3]\,x\,[1,2] + \omega_1 R/3, \tag{B.3a}$$

$$0 = PW/3 - x\,[2,3]\,(r_0 + t\,[2,3] + sL\,[2,1] + sL\,[2,3] + SL\,[3,1] + SL\,[3,2])$$
$$+ sL\,[1,2]\,x\,[1,3] + sL\,[3,2]\,x\,[3,3] + SL\,[1,3]\,x\,[2,1] + SL\,[2,3]\,x\,[2,2] + \omega_2 R/3, \tag{B.3b}$$

$$0 = PW/3 - x\,[3,3]\,(r_1 + t\,[3,3] + sL\,[3,1] + sL\,[3,2] + SL\,[3,1] + SL\,[3,2])$$
$$+ sL\,[1,3]\,x\,[1,3] + sL\,[2,3]\,x\,[2,3] + SL\,[1,3]\,x\,[3,1] + SL\,[2,3]\,x\,[3,2] + \omega_3 R/3. \tag{B.3c}$$

$$0 = R\frac{\gamma}{3} - (P + SL\,[1,2] + SL\,[1,3])\,U + SL\,[2,1]\,V + SL\,[3,1]\,W$$
$$+ x\,[1,1]\,r_1 + x\,[3,1]\,r_1 + x\,[2,1]\,r_0, \tag{B.4a}$$

$$0 = R\frac{\gamma}{3} + SL\,[1,2]\,U - (P + SL\,[2,1] + SL\,[2,3])\,V + SL\,[3,2]\,W$$
$$+ x\,[1,2]\,r_1 + x\,[3,2]\,r_1 + x\,[2,2]\,r_0, \tag{B.4b}$$

$$0 = R\frac{\gamma}{3} + SL\,[1,3]\,U + SL\,[2,3]\,V - (P + SL\,[3,1] + SL\,[3,2])\,W$$
$$+ x\,[1,3]\,r_1 + x\,[3,3]\,r_1 + x\,[2,3]\,r_0. \tag{B.4c}$$

$$0 = \frac{P\gamma}{3} - \omega_1\,(r_1 + R + sL\,[1,3] + sL\,[1,2]) + \omega_2 sL\,[2,1] + \omega_3 sL\,[3,1]\,, \tag{B.5a}$$

$$0 = \frac{P\gamma}{3} - \omega_2\,(r_0 + R + sL\,[2,3] + sL\,[2,1]) + \omega_3 sL\,[3,2] + \omega_1 sL\,[1,2]\,, \tag{B.5b}$$

$$0 = \frac{P\gamma}{3} - \omega_3\,(r_1 + R + sL\,[3,1] + sL\,[3,2]) + \omega_1 sL\,[1,3] + \omega_2 sL\,[2,3]\,. \tag{B.5c}$$

$$0 \;=\; \frac{Pn_0}{3} \;-\; \epsilon_1\,(r_1 + sL\,[1,3] + sL\,[1,2]) \;+\; \epsilon_2 sL\,[2,1] \;+\; \epsilon_3 sL\,[3,1]\,, \tag{B.6a}$$

$$0 \;=\; \frac{Pn_0}{3} \;-\; \epsilon_2\,(r_0 + sL\,[2,3] + sL\,[2,1]) \;+\; \epsilon_1 sL\,[1,2] \;+\; \epsilon_3 sL\,[3,2]\,, \tag{B.6b}$$

$$0 \;=\; \frac{Pn_0}{3} \;-\; \epsilon_3\left(r_1 + sL\left[3,1\right] + sL\left[3,2\right]\right) \;+\; \epsilon_1 sL\left[1,3\right] \;+\; \epsilon_2 sL\left[2,3\right]. \quad \text{(B.6c)}$$

$$F = U + V + W + x\left[1,3\right] + x\left[2,2\right] + x\left[3,1\right] + \gamma + \omega_1 + \omega_2 + \omega_3. \quad \text{(B.7)}$$

$$I_{PL} = r_1\left(x\left[1,3\right] + x\left[3,1\right] + \omega_1 + \omega_3 + \epsilon_1 + \epsilon_3\right) + r_0\left(x\left[2,2\right] + \omega_2 + \epsilon_2\right). \quad \text{(B.8)}$$

Here P is excitation rate. U, V and W are the relative populations of O_2 in the spin states -1, 0 and +1, respectively. $x[i,j]$ is the relative population of triplet oxygen/exciton pairs, where i refers to exciton spin states and j refers to O_2. γ is relative population of the excited oxygen molecules (into their singlet state). $t[i,j]$ is transfer coefficients from exciton spin state $|i\rangle$ to the O_2 spin state $|j\rangle$. Recombination rates of exciton from state $|-1\rangle$ and $|+1\rangle$ are equal and represented by r_1. The recombination rate of exciton from state $|0\rangle$ is r_0. R is the O_2 relaxation rate. After the singlet $^1O_2$ is produced, the excitons can be created continuously so that the ω_1, ω_2 and ω_3 are population of exciton spin states $|-1\rangle$, $|0\rangle$ and $|+1\rangle$, respectively. The ϵ_1, ϵ_2 and ϵ_3 are population of excitons without O_2 in the spin states $|-1\rangle$, $|0\rangle$ and $|+1\rangle$, respectively. The spin lattice relaxation of the exciton and O_2 are represented by $sL[m,n]$ and $SL[m,n]$, respectively. Here m,n are refer to spin state of exciton and O_2, respectively. If F is equal to 1, the system refers to the situation that every exciton is surrounded by O_2. In contrast, for $F = 0$, the system is in the absence of O_2. Finally, I_{PL} is the PL intensity arising from the Si exciton recombination.

Numerical calculation of all equations will allow us to simulate the energy transfer model between Si nanocrystals and oxygen molecules as shown the results in chapter 4.